Master's thesis

NTNU
Norwegian University of Science and Technology
Faculty of Natural Sciences
Department of Physics

Andreas Halkjelsvik Mjøs

Spontaneous Vortex Phase and Quantum Phase Diagram of Ferromagnetic Superconductors

Master's Thesis in Condensed Matter Physics

Master's thesis in Applied Physics and Mathematics
Supervisor: Jacob Linder

June 2020

NTNU
Norwegian University of
Science and Technology

Andreas Halkjelsvik Mjøs

Spontaneous Vortex Phase and Quantum Phase Diagram of Ferromagnetic Superconductors

Master's Thesis in Condensed Matter Physics

Master's thesis in Applied Physics and Mathematics
Supervisor: Jacob Linder
June 2020

Norwegian University of Science and Technology
Faculty of Natural Sciences
Department of Physics

NTNU
Norwegian University of
Science and Technology

Abstract

Motivated by discoveries of the coexistence of ferromagnetism and superconductivity in uranium-based structures, the 2D extended single-band Hubbard model is used in the quantum mechanical description of ferromagnetic equal-spin p-wave superconductors, both in the presence and absence of a magnetic field. The Bogoliubov-de Gennes equations are solved self-consistently and the free energies of different quantum phases are compared in order to compute phase diagrams. The ferromagnetic interaction has been modeled by the on-site Hubbard U-term or by the introduction of the exchange field h. In the first part of this master's thesis, a bulk system without any magnetic flux is considered. In the case of nearest-neighbour superconducting interaction strength of $V/t = -4.0$ and with $h/t = 0.5$, both in units of the hopping amplitude t, the phase diagram shows that the orbital p-wave symmetry $p_x + ip_y$ has higher stability than p_x and $p_x + p_y$. Using the Hubbard U-term with magnetic interaction strength of $U/t = 8.5$ instead, there are also smaller regions where the free energy of p_x or $p_x + p_y$ is the lowest. In addition, the paramagnetic phase appears both in the normal conducting and the superconducting state. The phase diagrams can be explained in terms of what is most energetically favourable of having a higher ferromagnetic order in the normal conducting state and the condensation energy of the superconducting phases. The dominance of $p_x + ip_y$ can be understood from its $\boldsymbol{k}$-space gap function without nodal lines.

In the second part, a magnetic field is incorporated into the model utilizing the Peierls substitution. To include the screening-effect of the supercurrent, the possibility of determining the vector potential self-consistently through the Maxwell equation is investigated. Despite testing of different solution strategies, there are no signs of convergence of the self-consistent solution. This is possibly caused by the breakdown of the Peierls formalism due to too large changes of the vector potential between sites in the lattice. By considering extreme type II superconductors with a large Ginzburg-Landau parameter, the supercurrent can be ignored. In this case, the spontaneity of the vortex phase comes solely from the magnetic field produced by the ferromagnetic order. For $h/t = 0.1$ and $V/t = -2.5$, the phase diagram shows the presence of spontaneous vortex phases with significant p_x and p_y superconducting order parameters. Increasing the exchange field to $h/t = 3.0$, computed phase diagrams become unreliable. Again, this can be explained by the limited validity of the Peierls substitution. The high magnetization gives too large changes of the vector potential.

Sammendrag

Motivert av oppdagelser for sameksistens av ferromagnetisme og superledning i uraniumbaserte strukturer, er den 2D utvidede enkeltbånd Hubbard-modellen brukt i den kvantemekaniske beskrivelsen av ferromagnetiske like-spinn p-bølge superledere, både med og uten et magnetfelt til stede. Bogoliubov-de Gennes-ligningene er løst selvkonsistent og den frie energien til ulike kvantefaser er sammenlignet for å beregne fasediagrammer. Den ferromagnetiske interaksjonen har blitt modellert med on-site Hubbard-U-ledd eller ved introduksjon av utvekslingsfeltet h. I første del av denne masteroppgaven er et bulk system uten magnetisk fluks betraktet. I tilfellet med nærmeste-nabo superledende interaksjon på $V/t = -4.0$ og med $h/t = 0.5$, begge i enheter av hopping-amplituden t, illustrerer fasediagrammet at den orbitale p-bølge-symmetrien $p_x + ip_y$ har høyere stabilitet enn p_x og $p_x + p_y$. Ved bruk av Hubbard-U-leddet med magnetisk interaksjonsstyrke $U/t = 8.5$ i stedet, finnes også områder hvor den frie energien til p_x eller $p_x + p_y$ er lavest. I tillegg er den paramagnetiske fasen til stede både i den normalt-ledende og den superledende tilstanden. Fasediagrammene kan forklares i form av hva som er mest energetisk gunstig av å ha en høyere ferromagnetisk orden i den normalt-ledende tilstanden og kodensasjonsenergien til de superledende fasene. Dominansen til $p_x + ip_y$ kan forstås fra dets $\boldsymbol{k}$-roms gapfunksjon uten nodale linjer.

I andre del er et magnetfelt innlemmet i modellen ved å utnytte Peierls-substitusjonen. For å inkludere skjermingseffekten til superstrømmen, er muligheten for å bestemme vektorpotensialet selvkonsistent gjennom Maxwell-ligningen, undersøkt. Til tross for testing av ulike løsningsstrategier, er det ingen tegn til konvergens for den selvkonsistente løsningen. Dette er muligens forårsaket av sammenbrudd for Peierls-formalismen på grunn av for store endringer i vektorpotensialet mellom gitterpunkter. Ved å betrakte ekstreme type-II-superledere med en stor Ginzburg-Landau parameter, kan superstrømmen bli ignorert. I dette tilfellet kommer spontaniteten til vorteksfasen utelukkende fra magnetfeltet produsert av den ferromagnetiske ordenen. For $h/t = 0.1$ og $V/t = -2.5$ viser fasediagrammet at spontane vorteksfaser med signifikante p_x og p_y superledende ordensparametere, er til stede. Ved økning av utvekslingsfeltet til $h/t = 3.0$, blir de beregnede fasediagrammene upålitelige. Igjen kan dette forklares ut ifra den begrensede gyldigheten til Peierls-substitusjonen. Den høye magnetiseringen gir for store endringer i vektorpotensialet.

Contents

List of Figures

List of Tables

List of Abbreviations

AFM	Antiferromagnetic
BCS	Bardeen-Cooper-Schrieffer
BdG	Bogoliubov-de Gennes
DOS	Density of states
FM	Ferromagnetic
GL	Ginzburg-Landau
MUC	Magnetic unit cell
NC	Normal conductor
PM	Paramagnetic
SC	Superconductor
ZES	Zero-energy states

Preface

This master's thesis is written as a final assignment in the Master's Degree Programme "Applied Physics and Mathematics" at the Norwegian University of Science and Technology (NTNU). During the period of research, I have been part of the Linder Group at the Center for Quantum Spintronics (QuSpin). The master's project constitutes 30 ECTS credits, and it has lasted for 20 weeks. This research is based on a 15 ECTS credits specialization project, where different forms of magnetism and opposite-spin unconventional superconductivity were studied separately. For these phenomena, computed phase diagrams were found to be in well agreement with published results. We did also create the vortex phase of conventional s-wave superconductivity, performing the Peierls substitution. In this master's project, the combination of superconductivity and magnetism in one quantum mechanical system has been analyzed, in terms of ferromagnetic equal-spin p-wave superconductors. The numerical methods have been extended for the computation of phase diagrams for new types of quantum phases, and to allow for the exploration of the spontaneous vortex phase. It can be expected that a deeper knowledge about the coexistence of magnetism and superconductivity will provide more insight into the behaviour of unconventional superconductors. In recent years, physicists have realized that magnetic order and superconducting correlations can be present simultaneously. However, there are still aspects of the so-called unconventional superconductors that are not fully understood.

I have found this period of research very interesting. My impression is that we have been working close to the frontier of research in this field, using models that have been the basis for much of the preceding literature. The originality of the project stems from there apparently being no previous studies aiming to compute quantum phase diagrams of the spontaneous vortex phase of ferromagnetic p-wave superconductors, utilizing the formalism of the Peierls phase. I would like to thank my supervisor Jacob Linder for his support in the search for the best possible solution strategy. The project has been challenging, including numerous hours of testing and debugging of programming code. I would also like to thank him for engaging and informative discussions about the topics of interest. Because of the outbreak of Covid-19, we have been forced to hold our weekly meetings on a digital platform. I feel like we did find a good solution here. I am also grateful for all the discussions we have had on mail.

Andreas Halkjelsvik Mjøs
Oslo, June 2020

Chapter 1

Introduction

1.1 Historical background

Historically, magnetism and superconductivity have attracted much interest in the study of solid state systems. The presence of a magnetic interaction has been known from ancient times [1]. In the beginning of the 19^{th}, the physicists Oersted, Ampère and Faraday did pioneering work for the understanding of magnetism [2]. In 1820, Oersted demonstrated that an electrical current creates a magnetic field, and shortly after, Ampère derived a mathematical formula for the magnetic force between two current elements. The full interconnection between electricity and magnetism was discovered when Faraday realized that a varying magnetic field can induce an electrical current. This was formally explained classically by Maxwell (1964) when he published a set of equations relating electric and magnetic fields [3]. The emergence of quantum mechanics in the 1920s led to new insights in the quantitative description of magnetism. In 1925, the famous Stern-Gerlach experiment indicated that electrons carry an intrinsic angular momentum, referred to as their spin [4]. After the Pauli exclusions principle was introduced (1925) [5], Heisenberg (1928) realized that the electron-electron Coulomb repulsion combined with the Pauli principle is responsible for the high-temperature magnetic order of some materials [6]. This illustrated that a complete description of magnetism can only be given using quantum mechanics.

When it comes to superconductivity, Kamerlingh Onnes (1911) discovered the vanishing direct current electrical resistance of mercury at 4.2 K [7]. In 1933, Meissner and Oschenfeld demonstrated that superconductors are not only perfect conductors [8]. They also enter a thermodynamic state of perfect diamagnetism, expelling an external magnetic field from the bulk. A fully quantum mechanical model of superconductivity was published in 1957 by Bardeen, Cooper and Schrieffer, which is known as the BCS theory [9]. This theory applies to conventional superconductors, that is elements, alloys and simple compounds at temperatures sufficiently close to 0 K [10]. For instance, the isotope effect of Fröhlich (1950) [11] was confirmed by the BCS theory, giving a relation between isotopic mass and critical temperature in agreement with experiments [12, 13, 14]. The detection of high-temperature superconductivity in a perovskite-type copper oxide (insulator) at 35 K by Bednorz and Müller (1986), marked the beginning for the research on a new class of superconductors [15, 16]. The year after a similar material was measured to have a critical temperature of 93 K [17]. In the following years, materials with even higher critical temperatures have been confirmed experimentally, but the ultimate goal of room temperature superconductivity has not yet been reached [18]. It

took 50 years to establish a microscopic theory of conventional superconductors (BCS) from the 1911-discovery of superconductivity. Still, there is no widely accepted theory available for unconventional high-temperature superconductors, reminiscent of the BCS theory [19].

In recent times, ferromagnetism and superconductivity are found to be coexisting phenomena in materials like UGe_2, URhGe and UCoGe [20, 21, 22]. Historically, ferromagnetism and superconductivity have been considered as incompatible based on the notion of the ferromagnetic order destroying the superconducting condensate [23]. This is the conventional picture predicted by the BCS theory with opposite-spin singlet paring. Since the internal field of ferromagnets tends to align the spins of electrons, the so-called spin-triplets of equal-spin electrons are supposed to be more compatible with ferromagnetic order [24, 25]. In 1980, Fay and Appel theoretically predicted the presence of the equal-spin paring in the ferromagnet $ZrZn_2$ [26]. A new candidate for uranium-based ferromagnetic superconductors was reported in 2019, that is UTe_2, with spin-triplet pairing [27]. In short, the extended number of ferromagnetic superconductors through the last decade, has provided a versatile way of studying unconventional superconductivity [28]. It is also worth to point out that there is much interest related to the role spin-triplet superconductivity can have in future spintronic devices [29].

In the mathematical description of magnetic and superconducting phases, different forms of the Hubbard model, first published in 1963 [30], have been used to a large extent. The compatibility of the phases has also been studied using the framework of the Hubbard model [31]. In particular, the model has successfully predicted features of solid state systems that have been experimentally verified afterwards [32]. The true glory of the Hubbard model is related to its simple structure, despite the complex nature of many-particle systems in condensed matter physics.

1.2 Objectives and motivations

The aim of this thesis has been the exploration of the spontaneous vortex phase of ferromagnetic p-wave equal-spin triplet superconductors. In particular, the investigation of quantum phases that emerge in materials where ferromagnetism and superconductivity coexist intrinsically, will be of importance. Emphasis will be placed on establishing the quantum phases that appear in such systems, including the possibility of a spontaneous vortex phase due to the simultaneous presence of a magnetic vector potential and superconducting order. Of special interest will be the computation of phase diagrams, showing the phase of the highest stability for a set of physical parameters.

The framework, which will be used in the quantum mechanical treatment of ferromagnetic superconductors, is the tight-binding formalism with the integration of magnetic and superconducting interaction terms. Numerically, we will solve a set of Bogoliubov-de Gennes (BdG) equations self-consistently until convergence in the magnetic and superconducting order parameters is achieved. In the search for the spontaneity of the vortex phase, the effect of a magnetic field will be included in the model by what is known as the Peierls substitution [33, 34]. This is a convenient method as the vector potential enters the Hamiltonian only through a complex phase. In previous literature, the formalism of the Peierls phase has been utilized widely in the study of the vortex state of unconventional superconductors. However, the validity of this method is limited [35]. In this thesis, we will test if the magnetic field from the supercurrent can be accounted for by solving the Maxwell equation, when the Peierls substitution is implemented. Alternatively, the supercurrent will be disregarded and the spontaneity of the

vortex state will solely arise due to the presence of ferromagnetic order. From what we know, a spontaneous vortex phase diagram of ferromagnetic equal-spin p-wave superconductors using this formalism, has not been calculated before.

The choice of studying equal-spin triplets is motivated by the behaviour of these type of superconducting correlations in ferromagnetic structures. First of all, we have the long-range proximity effect for equal-spin superconducting electron pairs in FM-SC heterostructures [36]. The essence of this phenomenon is that the ferromagnet has a larger pair-breaking effect on electron pairs of opposite spins than on equal-spin superconducting correlations [37]. Experimentally, by measurements of the penetration depth of the supercurrent in ferromagnetic materials, the existence of equal-spin superconductivity has been verified [38, 39]. More importantly for this master's project, there are, as mentioned in the previous section, experimental results showing the existence of spin-triplet pairing in ferromagnetic superconductors. Moreover, self-induced vortices, that is a spontaneous vortex phase, have been predicted theoretically in bulk materials with coexistence of ferromagnetism and superconductivity [40, 41]. In addition, Jiao *et al.* have found a spontaneous vortex ground state in an iron-based ferromagnetic superconductor [42].

1.3 Structure of the thesis

The thesis is organized in three parts. The first part consists of chapters 2, 3 and 4, which are devoted to the explanation of important concepts discussed in later chapters. In chapter 2, the second quantization formalism, the tight-binding model and the lattice structure of the system are introduced. Further, in chapters 3 and 4, magnetism and superconductivity are studied separately in order to understand the characteristic properties of these quantum mechanical phenomena. In the second part of the thesis, which is chapter 5, magnetism and superconductivity will be combined in the form of ferromagnetic equal-spin p-wave superconductors, and in the absence of a magnetic field. In the third part, there will be a finite magnetic flux through the system. In chapter 6, different solution strategies for the self-consistent computation of the vector potential by solving the Maxwell equation, are outlined. Here the discussion will be limited to the case of an external magnetic field instead of ferromagnetic order. This means that the spontaneity of the vortex phase will not be explored in this chapter. To find a convergent solution for this simpler case, can be considered as a prerequisite for being able to investigate the spontaneous vortex phase using this method. In chapter 7, the spontaneous vortex phase will be explored without solving the Maxwell equation. The source of the magnetic field is then solely the magnetization caused by alignment of electronic spins. Finally, general conclusions follow, and we will have a short outlook for future research on this topic.

1.4 Units

Throughout this document, the system of natural units (Lorentz-Heaviside) will be used. This includes setting the reduced Planck constant $\hbar = 1$, the Boltzmann constant $k_{\mathrm{B}} = 1$ and the permeability $\mu_0 = 1$. Also, the 2D lattice will be modeled with nearest-neighbour spacing $a = 1$. Numerically, physical parameters are expressed in units of the hopping amplitude t. In the case of a non-zero flux through the system, the magnetic field will be represented in units of the elementary superconducting flux quanta $\Phi_0 = h/2e$.

Chapter 2

Tight-binding model and lattice structure

In the first section of this chapter, the second quantization formalism is introduced. This formalism has been utilized throughout this thesis to obtain Hamiltonians on a form suitable for numerical computations. The next section is devoted to a description of the lattice structure used in this thesis, and the associated Brillouin zone. We will also have a short look at the tight-binding Hamiltonian in the grand-canonical ensemble, and how it can be transformed to $\boldsymbol{k}$-space. The chapter is concluded by the introduction of the Fermi surfaces of the model.

2.1 The second quantization formalism

The basic concepts of the second quantization formalism outlined here are in accordance with the book of Fetter and Walecka and the Fjærestad's lecture notes [43, 44]. In second quantization, many-particle states are defined by giving the number of particles in each single-particle state,

$$|n_1, n_2, n_3, ...\rangle\,, \tag{2.1}$$

where n_i $(i = 1, 2, 3, ...)$ is the occupation number for single-particle state i. A particle can be created in a single-particle state with quantum numbers α using the creation operator $\hat{c}^\dagger_\alpha$, and annihilated by the annihilation operator $\hat{c}_\alpha$. The antisymmetry of fermionic many-particle states is reflected in the anticommutation relation of fermionic creation and annihilation operators,

$$\{\hat{c}^\dagger_\alpha, \hat{c}_{\alpha'}\} = \delta_{\alpha,\alpha'}. \tag{2.2}$$

Analogously, bosons are symmetric under exchange of single-particle coordinates (position and spin), and for bosonic creation $(\hat{b}^\dagger_\alpha)$ and annihilation $(\hat{b}_\alpha)$ operators, we have the following commutator

$$[\hat{b}^\dagger_\alpha, \hat{b}_{\alpha'}] = \delta_{\alpha,\alpha'}. \tag{2.3}$$

In accordance with the Pauli exclusion principle, the fermionic number operators $\hat{c}^\dagger_\alpha \hat{c}_\alpha$ only have two possible eigenvalues (0 and 1). Bosons can occupy a single-particle state without any restriction on the maximal number of particles, so that $\hat{b}^\dagger_\alpha \hat{b}_\alpha$ can be any non-negative integer.

For a single-particle operator $\hat{A}$, which depends on the coordinates of a single particle, the

second quantization formalism gives

$$\sum_i \hat{A}(x_i) \rightarrow \sum_{\alpha,\beta} \langle\alpha|\, \hat{A}\, |\beta\rangle\, \hat{c}^\dagger_\alpha \hat{c}_\beta, \tag{2.4}$$

where

$$\langle\alpha|\, \hat{A}\, |\beta\rangle = \int \psi^*_\alpha(x) \hat{A}(x) \psi_\beta(x) dx. \tag{2.5}$$

Here ψ_α is an eigenfunction of the operator $\hat{A}$ with set of quantum numbers α. A two-particle operator $\hat{B}$ is dependent of the coordinates of two particles (x and x') as

$$\sum_{i,j\neq i} \hat{B}(x_i, x_j) \rightarrow \sum_{\alpha,\beta,\gamma,\delta} \langle\alpha,\beta|\, \hat{B}\, |\gamma,\delta\rangle\, \hat{c}^\dagger_\alpha \hat{c}^\dagger_\beta \hat{c}_\delta \hat{c}_\gamma, \tag{2.6}$$

where

$$\langle\alpha,\beta|\, \hat{B}\, |\gamma,\delta\rangle = \iint \psi^*_\alpha(x) \psi^*_\beta(x') \hat{B}(x,x') \psi_\gamma(x) \psi_\delta(x') dx dx'. \tag{2.7}$$

2.2 Introduction to the tight-binding model

In condensed matter physics, the tight-binding model can be used to describe electrons moving in a periodic potential due to a lattice of positive ions. Hence, the starting point of the derivation of the tight-binding Hamiltonian is

$$\hat{H} = \sum_i \frac{\hat{\boldsymbol{p}}_i^2}{2m} + \sum_i u(\boldsymbol{r}_i), \tag{2.8}$$

where the index i is used to label each electron in the system. The first term is the total kinetic energy operator of the electrons. In the second term, $u(\boldsymbol{r}_i)$ is the potential energy of an electron i with respect to the ions. These two terms can here be classified as single-particle operators as they only involve one particle index. In the tight-binding approximation, the electrons of the solid are assumed to be localized around the atoms. However, there is still a small overlap of electron orbitals of neighbouring atoms, leading to a finite probability of tunneling. When the electrons are tightly bound, we can write the eigenfunctions of the crystal electron system as a linear combination of atomic orbitals (LCAO) [45]. Accordingly, we choose $|i\rangle = \phi(\boldsymbol{r} - \boldsymbol{R}_i)$ as basis functions, where $\boldsymbol{R}_i$ is the position vector of atom i. In the single-band limit, there is one s-orbital per atom, and therefore, the basis functions have no orbital quantum number. Equation (2.8) can then be rewritten as [46]

$$\begin{aligned} \hat{H} &= \sum_{i,j,\sigma} \langle i|\, \Big(\frac{\hat{\boldsymbol{p}}^2}{2m} + u(\boldsymbol{r}) \Big)\, |j\rangle\, \hat{c}^\dagger_{i,\sigma} \hat{c}_{j,\sigma} \\ &= \sum_{i,j,\sigma} t_{i,j} \hat{c}^\dagger_{i,\sigma} \hat{c}_{j,\sigma}, \end{aligned} \tag{2.9}$$

where

$$t_{i,j} = \int \phi^*(\boldsymbol{r} - \boldsymbol{R}_i) \Big(\frac{-\nabla^2}{2m} + u(\boldsymbol{r}) \Big) \phi(\boldsymbol{r} - \boldsymbol{R}_j) d\boldsymbol{r}, \tag{2.10}$$

using equations (2.4) and (2.5). The matrix element $t_{i,j}$ is the hopping amplitude and is related to the probability of having an electron moving from site j to i. In other words, an electron with spin σ is created at site i and annihilated at site j. Therefore, the creation operator has site index i and the annihilation operator has site index j. As evident from equation (2.8), the hopping amplitude represents the kinetic energy of the electrons and their interaction with the periodic potential of the lattice ions. In the next chapters, the analysis will be restricted to nearest-neighbour hopping with constant amplitude $-t < 0$. This can be motivated by consideration of the hopping integral in equation (2.10). Since the integral becomes smaller when the overlap between the orbitals is reduced, the next-nearest neighbour hopping can be ignored in a tight-binding treatment. Usually, this is emphasized by replacing i, j by $\langle i, j \rangle$ in the sum of equation (2.9).

2.3 Lattice structure and first Brillouin zone

In this thesis, the lattice structure will be a 2D square lattice with nearest-neighbour spacing $a = 1$, as shown in figure 2.1a. The corresponding first Brillouin zone is illustrated in figure 2.1b. In the numerical calculations, the system is treated as translational invariant, that is periodic

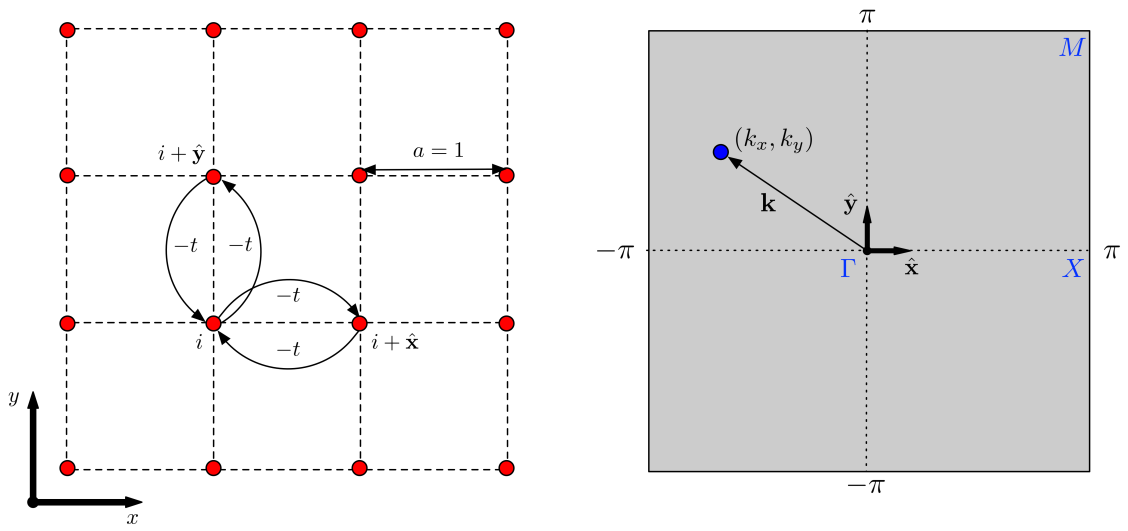

(a) The 2D square lattice with nearest-neighbour spacing $a = 1$. Hopping between lattice site i and two of its nearest-neighbours at $i + \hat{\boldsymbol{x}}$ and $i + \hat{\boldsymbol{y}}$ is illustrated. The hopping amplitude will be set to $-t$ as indicated.

(b) The reciprocal representation of the square lattice. The first Brillouin zone is bounded by $\pm\pi$ in the x- and y-direction. Here Γ, X and M denote the reciprocal points $(0, 0)$, $(\pi, 0)$ and (π, π), respectively.

Figure 2.1: Lattice structure in real space (a), and the first Brillouin zone in $\boldsymbol{k}$-space (b).

boundary conditions are implemented. Translational invariance implies that momentum $\boldsymbol{k}$ is a good quantum number, and can be used to label the states. With L lattice sites in both the x- and y-direction, the system consists of $N = L^2$ sites in total. Using periodic boundary conditions, there are also N primitive unit cells. As the number of distinct momentum vectors in the first Brillouin zone equals the number of primitive unit cells, we have N different momenta

inside the reciprocal space depicted in figure 2.1b. The components of $\boldsymbol{k}$, k_x and k_y, have the values

$$k_x, k_y = -\pi\frac{L-2}{L}, -\pi\frac{L-4}{L}, ..., \pi. \tag{2.11}$$

This representation gives L distinct k_x and k_y, which are evenly spread with spacing $2\pi/L$.

2.4 Grand canonical ensemble

In the study of many-particle systems in thermodynamic equilibrium at temperature T, there are two main possible choices of ensembles: the canonical and the grand canonical ensemble [47]. In the canonical ensemble, the system has a fixed number of particles, while it can vary in the grand canonical ensemble. In the following, the Hamiltonians will be defined in the grand canonical ensemble. Instead of describing the state of the system by the particle number, the chemical potential will be used. Fixing the chemical potential, the average number of particles is well-defined in the grand canonical ensemble. In order to obtain a Hamiltonian in this ensemble, we perform the shift

$$\hat{H} \to \hat{H} - \mu\hat{N}, \tag{2.12}$$

where μ is the chemical potential, and $\hat{N}$ is the total number operator. An eigenstate of $\hat{H} - \mu\hat{N}$ has a definite number of particles as long as $\hat{H}$ conserves the particle number, but in the grand canonical ensemble this number can be zero or any positive value. In the case of the tight-binding model, the grand canonical representation of equation (2.9) is therefore given as

$$\hat{H} = -t\sum_{\langle i,j\rangle,\sigma}\hat{c}^\dagger_{i,\sigma}\hat{c}_{j,\sigma} - \mu\sum_{i,\sigma}\hat{n}_{i,\sigma}. \tag{2.13}$$

Here the last sum is the total number operator of the electronic system.

2.5 Fourier transformation

The Hamiltonian in equation (2.13) is not diagonal in the real space indices. Utilizing the translational invariance of the system, we can perform a Fourier transformation in the x- and y-direction. This is done by transforming the real space creation and annihilation operators to $\boldsymbol{k}$-space operators as [48]

$$\hat{c}_{i,\sigma} = \frac{1}{\sqrt{N}}\sum_{\boldsymbol{k}}\hat{c}_{\boldsymbol{k},\sigma}e^{i\boldsymbol{k}\cdot\boldsymbol{r}_i} \tag{2.14}$$

$$\hat{c}^\dagger_{i,\sigma} = \frac{1}{\sqrt{N}}\sum_{\boldsymbol{k}}\hat{c}^\dagger_{\boldsymbol{k},\sigma}e^{-i\boldsymbol{k}\cdot\boldsymbol{r}_i}. \tag{2.15}$$

Inserting these transformations into the tight-binding Hamiltonian, results in

$$\begin{aligned}\hat{H} &= -t\sum_{i,\sigma}\left(\hat{c}^\dagger_{i,\sigma}\hat{c}_{i+\hat{\boldsymbol{x}},\sigma} + \hat{c}^\dagger_{i,\sigma}\hat{c}_{i-\hat{\boldsymbol{x}},\sigma} + \hat{c}^\dagger_{i,\sigma}\hat{c}_{i+\hat{\boldsymbol{y}},\sigma} + \hat{c}^\dagger_{i,\sigma}\hat{c}_{i-\hat{\boldsymbol{y}},\sigma}\right) - \mu\sum_i\hat{c}_{i,\sigma}\hat{c}^\dagger_{i,\sigma} \\ &= \sum_{i,\sigma}\frac{1}{N}\sum_{\boldsymbol{k},\boldsymbol{k}'}\Big[-t\big(e^{ik'_x} + e^{-ik'_x} + e^{ik'_y} + e^{-ik'_y}\big) - \mu\Big]e^{-i(\boldsymbol{k}-\boldsymbol{k}')\cdot\boldsymbol{r}_i}\hat{c}^\dagger_{\boldsymbol{k},\sigma}\hat{c}_{\boldsymbol{k}',\sigma} \\ &= \sum_{\boldsymbol{k},\sigma}\Big[-2t\big(\cos k_x + \cos k_y\big) - \mu\Big]\hat{c}^\dagger_{\boldsymbol{k},\sigma}\hat{c}_{\boldsymbol{k},\sigma}.\end{aligned} \tag{2.16}$$

In the last step, we have used the relation

$$N\delta_{\boldsymbol{k},\boldsymbol{k}'} = \sum_i e^{-i(\boldsymbol{k}-\boldsymbol{k}')\cdot\boldsymbol{r}_i}. \tag{2.17}$$

We now observe that $\hat{H}$ is diagonal in the quantum numbers $\boldsymbol{k}$ and σ. This means that the energy eigenvalues can be read-off as

$$E_{\boldsymbol{k},\sigma} = -2t\big(\cos k_x + \cos k_y\big) - \mu, \tag{2.18}$$

which are spin degenerate. Thus, the ground state, which is the state of lowest free energy at zero temperature, will contain as many up- as down-spin electrons. It can therefore be classified as a paramagnetic (PM) phase.

2.6 Fermi surfaces in the tight-binding model

In quantum mechanics, the Fermi surface is defined as the surface separating occupied and unoccupied electron states in $\boldsymbol{k}$-space at zero temperature. In the grand canonical ensemble for a fixed chemical potential μ, the Fermi surface goes through points in $\boldsymbol{k}$-space where the energy eigenvalues are zero. This is illustrated in figure 2.2 in the case of the tight-binding

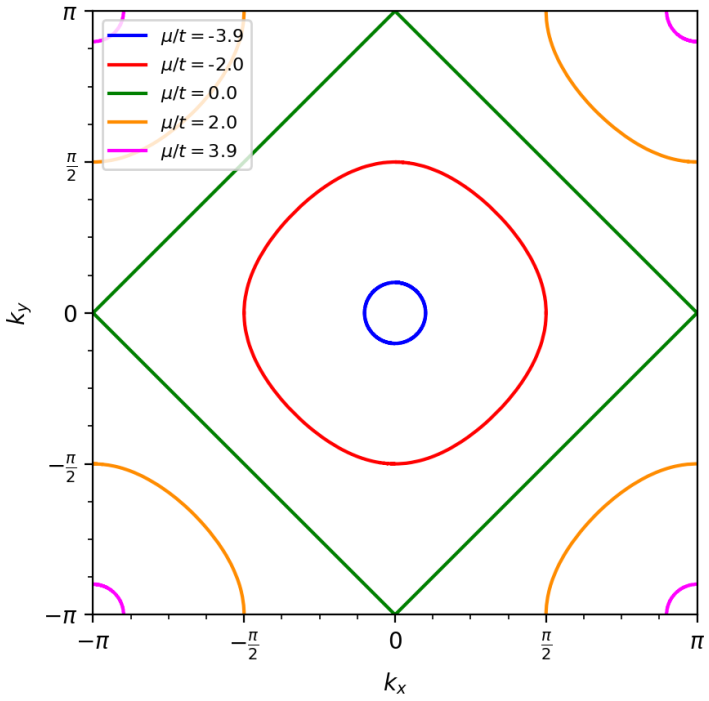

Figure 2.2: Fermi surfaces in the tight-binding model for different values of the chemical potential μ in units of t.

model for a couple of different chemical potentials. Considering equation (2.18), the maximal value of the first term is $4t$, and the minimal value is $-4t$. From this, we can find the chemical

potentials corresponding to minimal and maximal degree of filling of the electronic system. At zero temperature, the electrons will be in the ground state. Accordingly, the range of chemical potentials from minimal to maximal degree of filling is $\mu/t = [-4.0, 4.0]$. Half-filling is obtained at $\mu/t = 0.0$. This is also evident from figure 2.2. For chemical potentials near $\mu/t = -4.0$, like $\mu/t = -3.9$, only a small portion of the Brillouin zone is enclosed by the Fermi surface. This means that the ground state at a low chemical potential has few electrons in the system. In the opposite limit at $\mu/t = 3.9$, there are as many unoccupied as occupied states at $\mu/t = -3.9$. This symmetry about half-filling expresses the so-called particle-hole symmetry, which will be discussed in later chapters. At $\mu/t = 0.0$, the reciprocal space is divided exactly into two equally large regions, meaning that there are as many occupied as unoccupied states.

At first sight, non-positive values of the chemical potential seem to be of little relevance for metals. Experimental results show that the Fermi energy, which is the highest energy of the occupied states at zero temperature, is typically in the range from 2 to 12 eV [49]. Moreover, this is usually the completely dominating energy scale of metals. In the tight-binding model, the relevant energy scale is the hopping amplitude t, which includes both the kinetic energy of electrons and the potential energy from the interaction with the positive ion lattice. As we have seen above, the energy eigenvalues are not strictly positive, so negative values of the chemical potential are also possible. The important part is that higher values of μ relative to t, lead to more states being occupied.

Chapter 3

Magnetism

In the previous chapter, it was clear that the energy eigenvalues of the tight-binding model are spin degenerate, leading to paramagnetic (PM) order. We are in this chapter going to consider two possible extensions of the tight-binding model giving rise to ferromagnetic (FM) order. The first method is to include the so-called exchange field in the model. The second method is represented by the Hubbard model, which includes electron-electron Coulomb interactions in addition to the hopping term. To get an idea of how the FM and PM phases differ, an analytical phase diagram based on the Stoner criterion is analyzed. In addition, the concept of the particle-hole symmetry is examined.

3.1 Exchange field

The notion of an exchange field was postulated by Weiss in 1907 in his molecular field theory about ferromagnetism [50]. In this theory, the force experienced by an atom in a material is assumed to arise from the fields of the surrounding atoms. However, the physics behind an exchange field leading to interactions as large as observed experimentally, was not explained. The breakthrough occurred with the discovery of electronic spins. The exchange interaction leading to ferromagnetism was explained as an interplay between Coulomb forces and the Pauli principle [51]. A first extension of the tight-binding model facilitating ferromagnetism, can be written as a coupling between the local exchange field $\boldsymbol{h}_i$ and the second-quantized spin operator $\hat{\boldsymbol{S}}_i$ at site i, that is [52, 53]

$$\begin{aligned} \hat{H}_h &= -\sum_i \boldsymbol{h}_i \cdot \hat{\boldsymbol{S}}_i \\ &= -\sum_i \boldsymbol{h}_i \cdot \sum_{\sigma,\sigma'} \hat{c}^\dagger_{i,\sigma} \boldsymbol{\sigma}_{\sigma,\sigma'} \hat{c}_{i,\sigma'}, \end{aligned} \tag{3.1}$$

where $\boldsymbol{\sigma}_{\sigma,\sigma'}$ is the (σ,σ') element of the vector $\boldsymbol{\sigma} = \sigma_x\hat{x} + \sigma_y\hat{y} + \sigma_z\hat{z}$, and $\sigma_x, \sigma_y, \sigma_z$ are the three Pauli matrices. Without dwelling much on the physical origin of the exchange field, it certainly can be thought of as an internal interaction mechanism favoring alignment of spins parallel to each other. The physics behind ferromagnetism will become clearer in the next section when we consider magnetism in the Hubbard model.

The exchange field will be included in the model by making two simplifying assumptions. First of all, because a homogeneous bulk material is modeled, the exchange field is assumed

to be the same at all lattice sites, that is $\boldsymbol{h}_i \to \boldsymbol{h}$. In addition, there will only be a non-zero z-component ($h_z = h$). With these simplifications, the exchange field term can be written as

$$\begin{aligned}\hat{H}_h &= -h \sum_i \hat{S}_i^z \\ &= -h \sum_i \sum_{\sigma,\sigma'} \hat{c}_{i,\sigma}^\dagger \sigma_{\sigma,\sigma'}^z \hat{c}_{i,\sigma'} \\ &= -h \sum_i \left(\hat{n}_{i,\uparrow} - \hat{n}_{i,\downarrow}\right).\end{aligned} \tag{3.2}$$

In effect, this term leads to higher energy of electrons in spin down states than electrons having spin up, so that it favours FM order. The energy difference $2h$ is referred to as the Zeeman energy [54]. Finally, we notice that by inserting the Fourier transformations in equations (2.14) and (2.15), we get

$$\hat{H}_h = -h \sum_{\boldsymbol{k}} \left(\hat{n}_{\boldsymbol{k},\uparrow} - \hat{n}_{\boldsymbol{k},\downarrow}\right). \tag{3.3}$$

3.2 On-site single-band Hubbard model of magnetism

The single-band Hubbard model can be derived by including repulsive Coulomb electron-electron interactions in the Hamiltonian given in equation (2.8), that is the term

$$\hat{H}_v = \frac{1}{2} \sum_{i,j \neq i} v(\boldsymbol{r}_i - \boldsymbol{r}_j). \tag{3.4}$$

Written in this way, $v(\boldsymbol{r}_i - \boldsymbol{r}_j)$ is the potential energy due to the Coulomb repulsion between two electrons located at positions $\boldsymbol{r}_i$ and $\boldsymbol{r}_j$. Here the index j is over all electrons so that $j \neq i$. The purpose of the 1/2-factor is to compensate for the double counting in the summation over electron-electron interactions. Using the same basis functions as in section 2.2, equation (3.4) is in second quantization given by [51]

$$\begin{aligned}\hat{H}_v &= \frac{1}{2} \sum_{i,j,k,l,\sigma,\sigma'} \langle i,j|\, v(\boldsymbol{r} - \boldsymbol{r}')\, |k,l\rangle\, \hat{c}_{i,\sigma}^\dagger \hat{c}_{j,\sigma'}^\dagger \hat{c}_{l,\sigma'} \hat{c}_{k,\sigma} \\ &= \frac{1}{2} \sum_{i,j,k,l,\sigma,\sigma'} v_{i,j,k,l} \hat{c}_{i,\sigma}^\dagger \hat{c}_{j,\sigma'}^\dagger \hat{c}_{l,\sigma'} \hat{c}_{k,\sigma},\end{aligned} \tag{3.5}$$

where

$$v_{i,j,k,l} = \iint \phi^*(\boldsymbol{r} - \boldsymbol{R}_i) \phi^*(\boldsymbol{r}' - \boldsymbol{R}_j) v(\boldsymbol{r} - \boldsymbol{r}') \phi(\boldsymbol{r} - \boldsymbol{R}_k) \phi(\boldsymbol{r}' - \boldsymbol{R}_l) d\boldsymbol{r} d\boldsymbol{r}'. \tag{3.6}$$

If we now only consider on-site electron-electron interactions, the last sum of equation (3.5) is non-zero when $i = j = k = l$, that is $v_{i,j,k,l} = U\delta_{i,j,k,l}$. Accordingly, the Hamiltonian term is reduced to

$$\hat{H}_U = \frac{1}{2} U \sum_{i,\sigma,\sigma'} \hat{c}_{i,\sigma}^\dagger \hat{c}_{i,\sigma'}^\dagger \hat{c}_{i,\sigma'} \hat{c}_{i,\sigma}. \tag{3.7}$$

Based on the fact that each fermionic state can not be occupied by more than one electron, products of creation or annihilation operators with the same quantum numbers are zero, such

as $\hat{c}_{i,\sigma}\hat{c}_{i,\sigma}$. Hence, there are only non-zero terms when σ and σ' are opposite. The single-band Hubbard U-term is then given as [46]

$$\hat{H}_U = U \sum_i \hat{n}_{i,\uparrow}\hat{n}_{i,\downarrow}, \tag{3.8}$$

which is rewritten slightly by using the anticommutation property in equation (2.2). At this stage, we notice that the U-term respects the Pauli exclusion principle by the requirement of having opposite spins for the on-site electrons. Every lattice site where there are two electrons with opposite spin directions, increases the energy of the system by U, and in that way it represents an energy cost. Energetically, this Hamiltonian term by itself prefers FM order. However, when the tight-binding hopping term is also taken into account, the magnitude of U in relation to t determines which magnetic phase is present.

In the numerical treatment of the Hubbard term, we perform a Hartree-Fock mean-field approximation. This is done by writing the number operators as $\hat{n}_{i,\sigma} = \langle n_\sigma \rangle + \Delta\hat{n}_{i,\sigma}$, that is the sum of the mean and the fluctuation of the number operator [55]. In the case of translational invariance in the system, the average number operator has no site dependence. Inserted into the Hubbard term, we get

$$\begin{aligned}
\hat{H}_U &= U \sum_i \hat{n}_{i,\uparrow}\hat{n}_{i,\downarrow} \\
&= U \sum_i \big[\langle n_\uparrow \rangle + \Delta\hat{n}_{i,\uparrow}\big]\big[\langle n_\downarrow \rangle + \Delta\hat{n}_{i,\downarrow}\big] \\
&= U \sum_i \big[\langle n_\uparrow \rangle\langle n_\downarrow \rangle + \Delta\hat{n}_{i,\uparrow}\langle n_\downarrow \rangle + \Delta\hat{n}_{i,\downarrow}\langle n_\uparrow \rangle + \Delta\hat{n}_{i,\uparrow}\Delta\hat{n}_{i,\downarrow}\big].
\end{aligned} \tag{3.9}$$

Assuming small fluctuations $\Delta\hat{n}_{i,\sigma} = \hat{n}_{i,\sigma} - \langle n_\sigma \rangle$, we neglect the product of such differences, which leads to

$$\begin{aligned}
\hat{H}_U &= U \sum_i \big[\langle n_\uparrow \rangle\langle n_\downarrow \rangle + (\hat{n}_{i,\uparrow} - \langle n_\uparrow \rangle)\langle n_\downarrow \rangle + (\hat{n}_{i,\downarrow} - \langle n_\downarrow \rangle)\langle n_\uparrow \rangle + \Delta\hat{n}_{i,\uparrow}\Delta\hat{n}_{i,\downarrow}\big]. \\
&\approx U \sum_i \big[\hat{n}_{i,\uparrow}\langle n_\downarrow \rangle + \hat{n}_{i,\downarrow}\langle n_\uparrow \rangle - \langle n_\uparrow \rangle\langle n_\downarrow \rangle\big].
\end{aligned} \tag{3.10}$$

Exploiting the symmetry of the first two terms, gives

$$\hat{H}_U^{\mathrm{MF}} = U \sum_{i,\sigma} \hat{n}_{i,\sigma}\langle n_{\bar{\sigma}} \rangle + E_U, \tag{3.11}$$

in which

$$E_U = -UN\langle n_\uparrow \rangle\langle n_\downarrow \rangle, \tag{3.12}$$

is a constant. The mean-field approximation has effectively reduced the Hubbard term from being quartic in the fermionic creation and annihilation operators, to a term quadratic in such operators. The Fourier transform of $\hat{H}_U^{\mathrm{MF}}$ is

$$\hat{H}_U^{\mathrm{MF}} = U \sum_{\boldsymbol{k},\sigma} \hat{n}_{\boldsymbol{k},\sigma}\langle n_{\bar{\sigma}} \rangle + E_U. \tag{3.13}$$

3.3 Magnetic phases

In contrast to the exchange field term, a non-zero Hubbard U-term will not always give a splitting of the spin bands. As pointed out in the previous section, depending on how large the magnetic interaction strength U relative to the hopping amplitude t is, the tight-binding model will give PM or FM as the most stable phase. In short, when the system acquires lowest free energy by having equal number of electrons with spin up and down, the phase is PM. The stability of FM is greatest when it is energetically favourable to orient the spins in the same direction. In fact, the Hubbard model can also be used to study antiferromagnetic (AFM) systems, where neighbouring spins are opposite, but this magnetic phase will not be considered here.

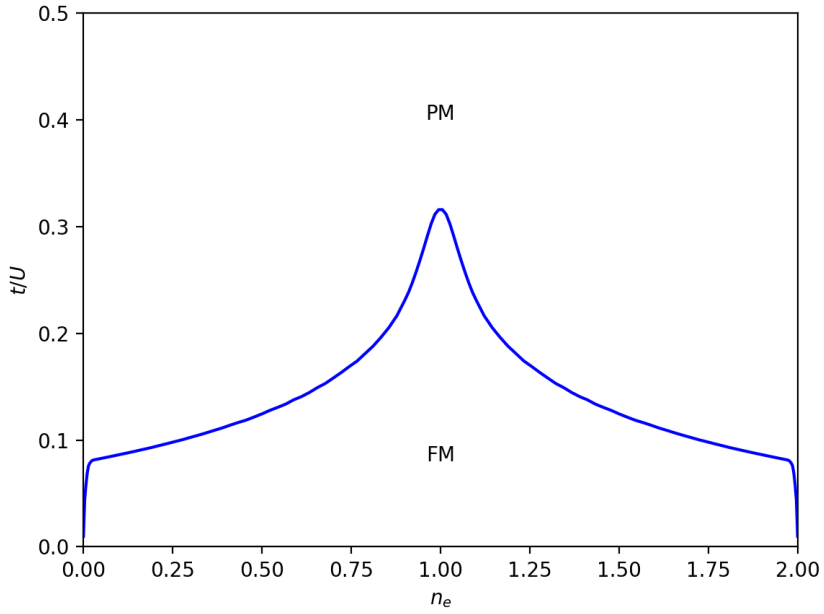

Figure 3.1: Phase diagram showing the PM-FM transition obtained by implementation of the Stoner criterion. The y-axis is plotted as t/U and the number of electron per site is on the x-axis. The temperature is $T/t = 0.0$.

To be more specific about the relation between PM and FM, we should have a look at what is known as the Stoner criterion. Although we are primarily interested to work in the grand canonical ensemble, the approach discussed by Hirsch will be followed here [56]. This means that we will consider the canonical ensemble with the number of electrons per site n_e fixed. The Stoner criterion is a theoretical result that can be used to predict the phase transition from PM to FM [57]. It follows from the properties of the magnetic susceptibility $\chi(\boldsymbol{q})$, which can be expressed as

$$\chi(\boldsymbol{q}) = \frac{\chi_0(\boldsymbol{q})}{1 - U\chi_0(\boldsymbol{q})}. \tag{3.14}$$

For a PM-FM transition, we have $\boldsymbol{q} = (0, 0)$. In the limit where the susceptibility becomes infinite, the PM phase is unstable against FM. The Stoner criterion is therefore

$$U\chi_0(\boldsymbol{q}) = 1, \tag{3.15}$$

where

$$\chi_0(\boldsymbol{q}) = D^{\text{can}}_{\text{spin}}(\mu). \tag{3.16}$$

In equation (3.16), $D^{\text{can}}_{\text{spin}}$ is the density of states per spin in the canonical ensemble, and it is computed in the non-interacting case $U/t = 0$. By implementation of the Stoner criterion numerically, we get the phase transition shown in figure 3.1. Accordingly, FM has lower free energy than PM when U is large compared to t, as predicted above. In other words, when $U \gg t$, the Hubbard U-term is most decisive for the free energy of the system. In what

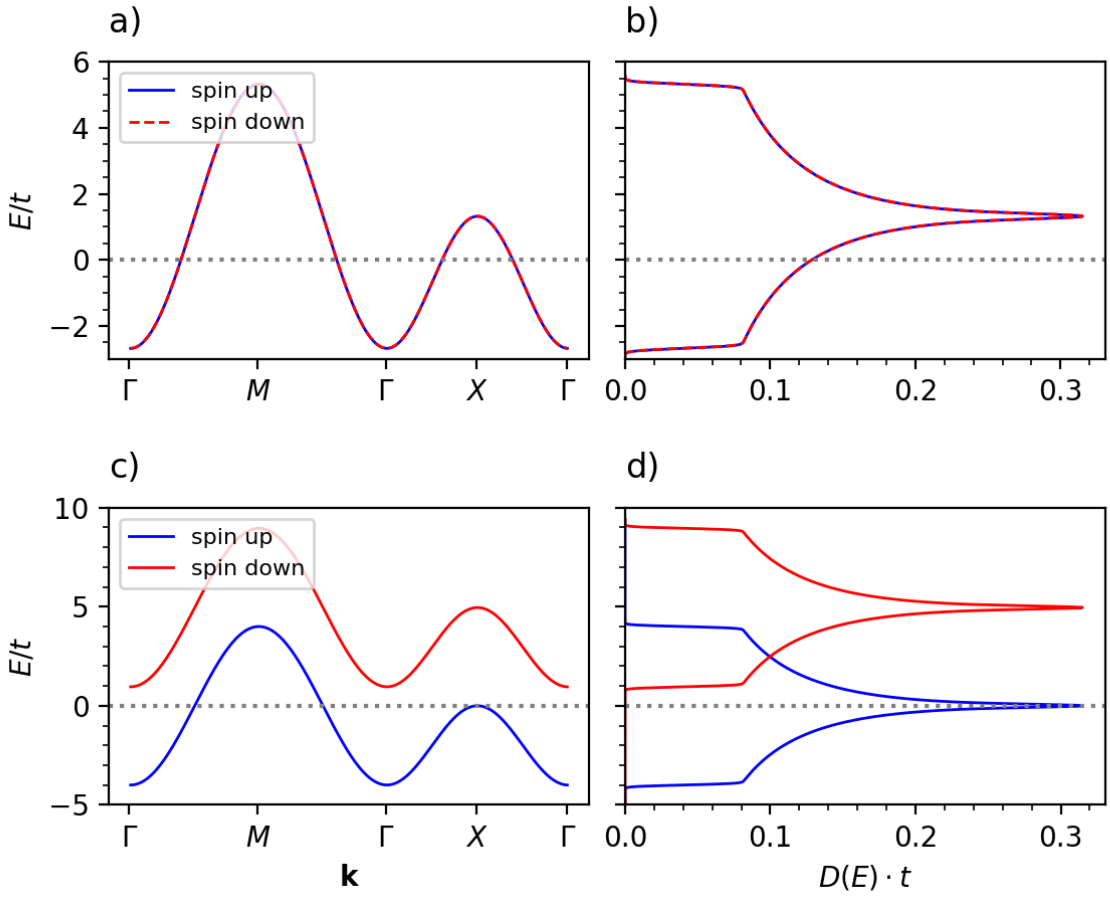

Figure 3.2: Grand canonical energy spectra and DOS in the Hubbard model at zero temperature. The different $\boldsymbol{k}$-points (Γ, M, X) are shown in figure 2.1b. The first row of plots (a and b) are for on-site interaction strength $U/t = 5.0$, resulting in the PM phase. In the second row (c and d), the magnetic phase is FM with $U/t = 10.0$. Energy spectra are in the left column, and the DOS to the right. Each plot distinguishes between up- and down-spin energies. The dashed line at grand canonical energy $E/t = 0.0$ is the Fermi level. All plots are for chemical potential $\mu/t = 0.0$.

is called the band limit ($t/U \to \infty$), the electrons behave as there are no electron-electron interactions, so that the magnetic phase is PM. In addition, the phase diagram is symmetric about half-filling at $n_e = 1.0$ because of the particle-hole symmetry, which is explained in the last section of this chapter. As we move to half-filling from below, the stability of FM against

PM becomes higher. We can understand this by considering what happens when the number of electrons increases in the system. Since it is a higher chance of having doubly occupied sites, the importance of the U-term is larger. At half-filling, there are as many electrons in the system as number of sites, so doubly occupied sites are unavoidable in the case of hopping.

In figure 3.2, the grand canonical energy spectra and density of states (DOS) for the PM and FM phases are shown. Comparing the plots a) and c), we observe that the dispersion for PM (a) is spin degenerate, while there is a splitting in the up- and down-spin band for FM (c). The latter is also the case using the exchange field term instead of the U-term. The associated DOS are illustrated on the right hand side. The shape of the up- and down-spin DOS is characteristic for the tight-binding model, having a centered peak and energy range of $8.0t$.

3.4 Fermi surfaces in the models of magnetism

The inclusion of magnetic interactions by the U- or h-term changes the correspondence between values of the chemical potential and the Fermi surfaces, with respect to what we found in section 2.6. Still, the Fermi surfaces are identical for a given electron density n_e, and the symmetry about half-filling remains. To see this, we first consider the mean-field Hubbard U-term in addition to the grand canonical μ-term, which can be written as

$$\hat{H}_U^{\mathrm{MF}} + \hat{H}_\mu = \sum_{i,\sigma} \big[U\langle n_{\bar{\sigma}}\rangle - \mu\big]\hat{n}_{i,\sigma}. \tag{3.17}$$

Evidently, with regards to the previous discussion about Fermi surfaces, the U-term results in a shift in the chemical potential. If $n_e = 0.0$, which implies $\langle n_\sigma\rangle = 0.0$, the U-term is zero and no shift occurs. Consequently, we have zero degree of filling at $\mu/t = -4.0$ as before. For the maximal electron density $n_e = 2.0$, $\langle n_\sigma\rangle = 1.0$. This means that the upper boundary of the chemical potential is $\mu/t = U/t + 4.0$. In total, the range $n_e = [0.0, 2.0]$ corresponds to $\mu/t = [-4.0, U/t + 4.0]$ with half-filling at $\mu/t = U/(2t)$, when magnetism is modeled by the Hubbard U-term. Hence, in the upper row of plots in figure 3.2, half-filling is obtained at $\mu/t = 2.5$, and in the lower row, this happens at $\mu/t = 5.0$. Likewise, we can write the sum of the exchange field term and the chemical potential term as

$$\hat{H}_h + \hat{H}_\mu = \sum_i \big[(-h-\mu)\hat{n}_{i,\uparrow} + (h-\mu)\hat{n}_{i,\downarrow}\big]. \tag{3.18}$$

The range of interest is then $\mu/t = [-h/t - 4.0, h/t + 4.0]$. Therefore, as opposed to the U-term, the exchange field term does not shift the chemical potential value of half-filling.

3.5 Magnetization

The magnetic order parameter, which is a measure of the degree of alignment of electronic spins in the system, is known as the magnetization. In the case of the Hubbard U-term, the average number operators for up- and down-spin electrons will be determined self-consistently.

Knowing $\langle n_\uparrow \rangle$ and $\langle n_\downarrow \rangle$, the magnetization along the up/down-direction can be computed as

$$M = \frac{1}{N} \sum_i (n_{i,\uparrow} - n_{i,\downarrow}) \tag{3.19}$$

$$= \langle n_\uparrow \rangle - \langle n_\downarrow \rangle. \tag{3.20}$$

In later chapters, a phase transitions from FM to PM will be defined as having the magnetization M becoming lower than a tolerance. This happens in figure 3.3 as the temperature is increased above a critical value. Below this temperature, there exists FM order in the system. The

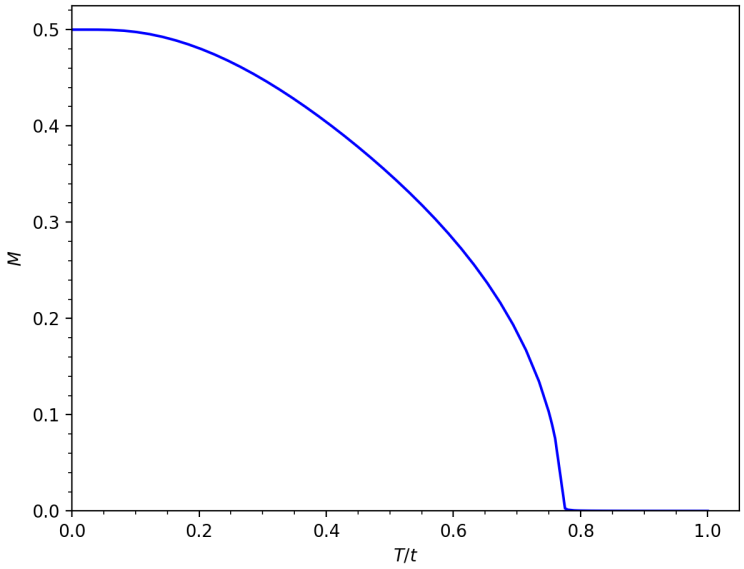

Figure 3.3: Magnetization M as a function of temperature T in units of t. The plot is obtained using interaction strength $U/t = 8.5$ and chemical potential $\mu/t = 0.0$.

transition to PM can be understood physically as a result of increasing thermal fluctuations in the system. With higher energy in the system, the electrons will start to occupy states at higher energy. Eventually, when the temperature is high enough, the energy difference due to spin band splitting will be negligible compared to the thermal energy, and the system enters the PM phase.

3.6 The particle-hole symmetry

We will now discuss the so-called particle-hole symmetry in terms of the Hubbard model and the exchange field term. For this, we divide the square lattice in figure 2.1a into two sublattices A and B. The nearest-neighbours of a site in A are then in B, and the lattice is classified as bipartite. For a bipartite lattice, the particle-hole transformation is defined as [58]

$$\hat{c}^\dagger_{i,\sigma} \to u_i \hat{c}_{i,\sigma}, \qquad u_i = \begin{cases} 1, & \text{if } i \in A \\ -1, & \text{if } i \in B \end{cases}. \tag{3.21}$$

Consequently, the number operator transforms as

$$\hat{n}_{i,\sigma} = \hat{c}^\dagger_{i,\sigma} \hat{c}_{i,\sigma} \to u_i^2 \hat{c}_{i,\sigma} \hat{c}^\dagger_{i,\sigma} = 1 - \hat{c}^\dagger_{i,\sigma} \hat{c}_{i,\sigma} = 1 - \hat{n}_{i,\sigma}, \tag{3.22}$$

where we have used that $u_i^2 = 1$. The particle-hole transformation has therefore turned the number operator for electrons into the one for holes, switching the occupation eigenvalues 0 and 1. Regarding the tight-binding hopping term, the particle-hole transformation of $\hat{c}^\dagger_{i,\sigma}\hat{c}_{j,\sigma}$ is

$$\hat{c}^\dagger_{i,\sigma}\hat{c}_{j,\sigma} \to u_i u_j \hat{c}_{i,\sigma}\hat{c}^\dagger_{j,\sigma} = \hat{c}^\dagger_{i,\sigma}\hat{c}_{j,\sigma}. \tag{3.23}$$

Here $u_i u_j = -1$ if sites i and j are nearest-neighbours, and we also get a factor -1 from the anticommutation of the creation and annihilation operator. Hence, the nearest-neighbour hopping term has the particle-hole symmetry. Next, we consider the interaction term in the Hubbard model. If the U-term is now written as [59]

$$\hat{H}_U = U \sum_i \Big(\hat{n}_{i,\uparrow} - \frac{1}{2}\Big)\Big(\hat{n}_{i,\downarrow} - \frac{1}{2}\Big), \tag{3.24}$$

it clearly has the particle-hole symmetry. Multiplying out, we obtain the extra terms $UN/4$ and $-U/2\sum_{i,\sigma}\hat{n}_{i,\sigma}$. The former leads to a shift in chemical potential, and the latter is a constant contribution to the energy. The modified U-term, which is invariant under the particle-hole transformation, describes the same physics as before. With respect to equation (3.22), the grand canonical term $-\mu\sum_{i,\sigma}\hat{n}_{i,\sigma}$ is not particle-hole-symmetric, but the transformation only gives a change in the sign of μ. Thus, for the Hubbard model, the magnetic phase having lowest free energy at $n_e = x$, will also be the most stable magnetic phase at $n_e = 2 - x$. Indeed, a phase diagram of magnetic phases will be symmetric about half-filling, as seen in figure 3.1.

For the exchange field term, the particle-hole transformation is

$$\begin{aligned} \hat{H}_h \to &- h \sum_i \big[(1 - \hat{n}_{i,\uparrow}) - (1 - \hat{n}_{i,\downarrow})\big] \\ &= h \sum_i (\hat{n}_{i,\uparrow} - \hat{n}_{i,\downarrow}). \end{aligned} \tag{3.25}$$

This demonstrates that the h-term is not particle-hole symmetric. It has an overall sign change because of the transformation. Effectively, this means that if the direction of the exchange field is switched simultaneously, the symmetry is respected. Fixing h, the down-spin becomes energetically preferable under the particle-hole transformation. Therefore, we can predict that the most stable states at symmetric points about half-filling $n_e = 1.0$, will have opposite spin configurations.

Chapter 4

Superconductivity

In the beginning of this chapter, the basic principles in the BCS theory of conventional superconductivity are introduced. Then we move on to the extended single-band Hubbard model, which is used to model unconventional equal-spin p-wave superconductivity in the following chapters. This Hamiltonian interaction term will be mean-field approximated and transformed to Fourier space. In the remaining part of the chapter, properties of equal-spin triplets are discussed. This includes symmetry characteristics of their order parameters in addition to the $\boldsymbol{k}$-space gap functions and DOS.

4.1 Introduction to the BCS theory

This introduction to the BCS theory gives important concepts discussed by Fossheim and Sudbø [60]. The basis of the theory is the net attraction of two electrons in the proximity of the Fermi level, as proposed by Cooper in 1956 [61]. The interaction can be pictured as an electron creating lattice distortions when it moves through a crystal. Displacements of positive ions produce dipole moments, affecting another electron. In quantum mechanics, this is a phonon-mediated scattering process. The Hamiltonian of the BCS model accounts for both the repulsive Coulomb interaction between electrons and the electron-phonon coupling, which in second quantization are respectively given as

$$\hat{H}_{\text{int}} = \frac{1}{4\pi\epsilon_0} \sum_{\boldsymbol{k},\boldsymbol{k}',\boldsymbol{q},\sigma,\sigma'} \frac{2\pi e^2}{\boldsymbol{q}^2} \hat{c}^\dagger_{\boldsymbol{k}+\boldsymbol{q},\sigma} \hat{c}^\dagger_{\boldsymbol{k}'-\boldsymbol{q},\sigma'} \hat{c}_{\boldsymbol{k},\sigma} \hat{c}_{\boldsymbol{k}',\sigma'} + \sum_{\boldsymbol{k},\boldsymbol{q},\sigma} M_{\boldsymbol{q}} (\hat{a}^\dagger_{-\boldsymbol{q}} + \hat{a}_{\boldsymbol{q}}) \hat{c}^\dagger_{\boldsymbol{k}+\boldsymbol{q},\sigma} \hat{c}_{\boldsymbol{k},\sigma}. \tag{4.1}$$

Here the c-operators are fermionic (electrons), and the a-operators are bosonic (phonons). In equation (4.1), the strength of the electron-phonon interaction is given by $\boldsymbol{M_q}$, which decreases with the ion mass and is proportional with the momentum transfer $\boldsymbol{q}$. Assuming that the phonons are free particles with well-defined energies $\omega_{\boldsymbol{q}}$, it can be shown that

$$\hat{H}_{\text{int}} = \sum_{\boldsymbol{k},\boldsymbol{k}',\boldsymbol{q},\sigma,\sigma'} \Big(\frac{1}{4\pi\epsilon_0} \frac{2\pi e^2}{\boldsymbol{q}^2} + \frac{2|M_{\boldsymbol{q}}|^2 \omega_{\boldsymbol{q}}}{\omega^2 - \omega^2_{\boldsymbol{q}}} \Big) \hat{c}^\dagger_{\boldsymbol{k}+\boldsymbol{q},\sigma} \hat{c}^\dagger_{\boldsymbol{k}'-\boldsymbol{q},\sigma'} \hat{c}_{\boldsymbol{k},\sigma} \hat{c}_{\boldsymbol{k}',\sigma'}, \tag{4.2}$$

where ω is the energy transferred between two electrons. By considering the fermionic creation and annihilation operators, we see that the Hamiltonian describes a two-step process where an electron in the state $|\boldsymbol{k},\sigma\rangle$ is scattered into the state $|\boldsymbol{k}+\boldsymbol{q},\sigma\rangle$, followed by the scattering of another electron in $|\boldsymbol{k}',\sigma'\rangle$ to $|\boldsymbol{k}'-\boldsymbol{q},\sigma'\rangle$. Both scatterings are caused by the same phonon

with momentum $\boldsymbol{q}$, propagating from the latter to the former electron. It is also clear that the attractive electron-electron interaction is predicted by the BCS theory. The second term of equation (4.2) is negative whenever $|\omega| < \omega_{\boldsymbol{q}}$, and it diverges in the limit where all the phonon energy is transferred between the electrons. At this stage, the Hamiltonian in equation (4.2) can be simplified by assuming that the sum of the two terms in the parenthesis is a negative constant for a thin shell about the Fermi surface, that is when $|\omega| \ll \omega_D$ (ω_D is the Debye frequency), and zero otherwise. This is in accordance with the BCS theory introduced in 1957 [9].

Figure 4.1 illustrates another important concept of the BCS theory. We observe that when the initial momenta of the two electrons are opposite ($\boldsymbol{k}_1 = -\boldsymbol{k}_2$), both electrons are guaranteed to stay inside the thin shell after the phonon scattering events whenever one of them does. In general, this is not the case when $\boldsymbol{k}_1 \neq -\boldsymbol{k}_2$, so the phonon-mediated electron-electron attraction is dominated by electrons having opposite momenta.

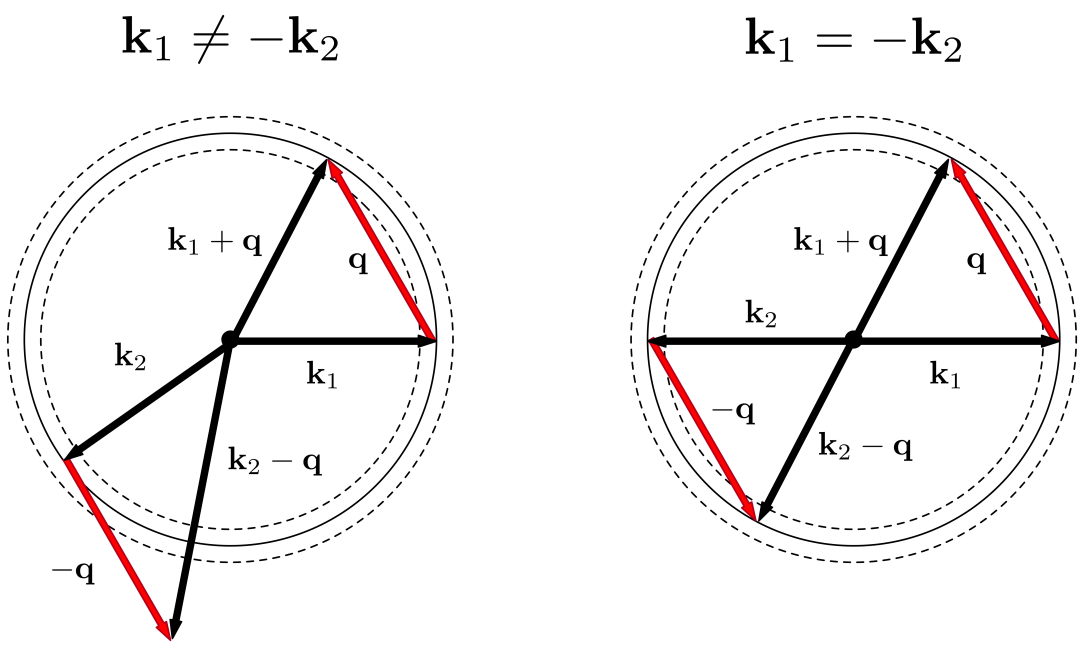

Figure 4.1: The figure illustrates two cases of phonon-mediated attraction between electrons. The two electrons have initial momenta $\boldsymbol{k}_1$ and $\boldsymbol{k}_2$. These momentum vectors have endpoints between the two dashed surfaces, representing the range where there is a non-zero attraction. The red arrows indicate phonon scattering events. The electron with momentum $\boldsymbol{k}_1$ is scattered by an incoming phonon with momentum $\boldsymbol{q}$. This electron then acquires a momentum of $\boldsymbol{k}_1 + \boldsymbol{q}$. The electron having momentum $\boldsymbol{k}_2$ is scattered by the same outgoing phonon, that is an incoming phonon with momentum of $-\boldsymbol{q}$. This figure is adapted from reference [60].

In context of the Pauli exclusion principle, these electrons will also preferably have opposite spins. The reason is that the attractive interaction is expected to be of short range, as it is mediated by phonons. By requiring opposite spins, we allow the electrons to approach each other in space without violating the Pauli principle. Two electrons interacting attractively and

having opposite spins and momenta, are a referred to as a Cooper pair in the BCS theory. The electron-electron interaction part of the Hamiltonian can now be written as

$$\hat{H}_{\text{int}} = \frac{1}{2} V_{\text{eff}} \sum_{\boldsymbol{k},\boldsymbol{k}',\sigma} \hat{c}^{\dagger}_{\boldsymbol{k},\sigma} \hat{c}^{\dagger}_{-\boldsymbol{k},\bar{\sigma}} \hat{c}_{-\boldsymbol{k}',\bar{\sigma}} \hat{c}_{\boldsymbol{k}',\sigma}, \tag{4.3}$$

where $V_{\text{eff}} < 0$, $(\boldsymbol{k}+\boldsymbol{q},\, \boldsymbol{k})$ is set to $(\boldsymbol{k},\, \boldsymbol{k}')$, and the Cooper pair relations $\boldsymbol{k}' = -\boldsymbol{k}$ and $\sigma' = \bar{\sigma}$ are used. Performing a mean-field approximation, we finally get [52]

$$\hat{H}^{\text{MF}}_{\text{BCS}} = \sum_{\boldsymbol{k},\sigma} (\epsilon_{\boldsymbol{k}} - \mu) \hat{c}^{\dagger}_{\boldsymbol{k},\sigma} \hat{c}_{\boldsymbol{k},\sigma} + V_{\text{eff}} \sum_{\boldsymbol{k},\boldsymbol{k}'} \langle c^{\dagger}_{\boldsymbol{k},\uparrow} c^{\dagger}_{-\boldsymbol{k},\downarrow} \rangle \hat{c}_{-\boldsymbol{k}',\downarrow} \hat{c}_{\boldsymbol{k}',\uparrow} + \text{h.c.}, \tag{4.4}$$

where $\epsilon_{\boldsymbol{k}}$ is the energy of an electron with momentum $\boldsymbol{k}$ in the absence of electron-electron interactions, and μ is the chemical potential of the system. The average in the interaction term is of special importance in the study of superconductors as we have

$$\Delta_0 = V_{\text{eff}} \sum_{\boldsymbol{k}} \langle c_{-\boldsymbol{k},\downarrow} c_{\boldsymbol{k},\uparrow} \rangle. \tag{4.5}$$

Here Δ_0 is the order parameter for the conventional s-wave superconductor, and it is a measure for the degree of Cooper pair ordering in the superconductor. Additionally, the BCS theory shows that there is a gap in the DOS of the superconductor, with magnitude $E_g = 2|\Delta_0|$ and centered about the normal-state Fermi level. Hence, in a superconductor, the Cooper pairs of electrons will create a superconducting condensate, occupying states below the energy gap. To break a Cooper pair, that is to excite an electron to the conduction band, an energy $E \geq E_g$ is required.

4.2 Extended single-band Hubbard model of equal-spin superconductivity

The BCS theory considered so far, gives a superconducting gap structure that is isotropic in $\boldsymbol{k}$-space. In the tight-binding model, the conventional s-wave superconducting order parameter is obtained if an on-site opposite-spin interaction term is used. Order parameters obeying other orbital symmetries, which are not predicted by the standard BCS theory, have been observed experimentally. For instance, experimental results indicate that cuprates have a d-wave superconducting gap structure [62]. Moreover, Sr_2RuO_4, which is a perovskite, has several properties reminiscent of a spin-triplet p-wave superconductor [63, 64]. In general, superconducting order is accepted to be related to an effective electron-electron attraction [65]. At the same time, the physical processes leading to the attraction is not fully understood for unconventional superconductors [66]. A complete justification for how a net attraction can arise physically for unconventional superconductors is beyond the scope of this thesis. Hence, there will not be any special assumptions about the form of Cooper paring mechanism. We are only seeking a Hamiltonian interaction term leading to the condensation of electron pairs into the superconducting state in more general terms than the standard BCS theory.

To model unconventional superconductivity, that is to allow for more complex gap structures, we should consider an extended form of the Hubbard model [65]. It turns out that if we

use an nearest-neighbour Hubbard interaction term given by

$$\hat{H}_V = \frac{1}{2}V \sum_{\langle i,j\rangle,\sigma} \hat{n}_{i,\sigma}\hat{n}_{j,\sigma}, \tag{4.6}$$

we will be able to construct superconducting order parameters with p-wave symmetry properties. Indeed, this will become clear in the remainder of the chapter where we examine the superconducting p-wave order parameters, similar to what is done in the PhD-thesis of Terrade [52]. In addition, the superconducting interactions expressed by equation (4.6) are between electrons having the same spin direction as we are interested in equal-spin triplets. We will also use negative values of V in the following, reflecting the effective attraction between electrons forming a Cooper pair.

4.2.1 Mean-field approximation

In the mean-field approximation scheme used here, we approximate the product of operators $\hat{A}$ and $\hat{B}$ as [6]

$$\hat{A}\hat{B} \approx \langle A\rangle\hat{B} + \hat{A}\langle B\rangle - \langle A\rangle\langle B\rangle, \tag{4.7}$$

like we did for the magnetic Hubbard term. The difference is that we choose other operators $\hat{A}$ and $\hat{B}$. Analogous to the BCS mean-field Hamiltonian in equation (4.4), $\hat{A} = \hat{c}_{i,\sigma}\hat{c}_{j,\sigma}$ and $\hat{B} = \hat{c}^\dagger_{j,\sigma}\hat{c}^\dagger_{i,\sigma} = \hat{A}^\dagger$. The resulting mean-field approximation of equation (4.6) is

$$\hat{H}_V^{\mathrm{MF}} = \frac{1}{2}V \sum_{\langle i,j\rangle,\sigma} \left[F^{\sigma,\sigma}_{i,j}\hat{c}^\dagger_{j,\sigma}\hat{c}^\dagger_{i,\sigma} + \mathrm{h.c.}\right] + E_V, \tag{4.8}$$

where the constant is given as

$$E_V = -\frac{1}{2}V \sum_{\langle i,j\rangle,\sigma} |F^{\sigma,\sigma}_{i,j}|^2, \tag{4.9}$$

In equation (4.8), the so-called equal-spin pairing amplitudes are generally defined as

$$F^{\sigma,\sigma}_{i,j} = \langle c_{i,\sigma}c_{j,\sigma}\rangle. \tag{4.10}$$

which is the correlation between the two electrons of an equal-spin Cooper pair at lattice sites i and j.

4.2.2 Fourier transformation

As before, in the treatment of a bulk superconductor, it is convenient to transform the Hamiltonian term to $\boldsymbol{k}$-space. The Fourier transformations of the creation and annihilation operators are given in equations (2.14) and (2.15). Inserting these into the mean-field superconducting

term, excluding the constant E_V, gives

$$\begin{aligned}\hat{H}_V^{\mathrm{MF}} &= \frac{1}{2}V\sum_{\langle i,j\rangle,\sigma}\left[F_{i,j}^{\sigma,\sigma}\hat{c}_{j,\sigma}^{\dagger}\hat{c}_{i,\sigma}^{\dagger}+\mathrm{h.c.}\right]\\ &= \frac{1}{2}V\sum_{i,\sigma}\left[F_{i,\sigma,\sigma}^{x+}\hat{c}_{i+\hat{\boldsymbol{x}},\sigma}^{\dagger}\hat{c}_{i,\sigma}^{\dagger}+F_{i,\sigma,\sigma}^{x-}\hat{c}_{i-\hat{\boldsymbol{x}},\sigma}^{\dagger}\hat{c}_{i,\sigma}^{\dagger}+F_{i,\sigma,\sigma}^{y+}\hat{c}_{i+\hat{\boldsymbol{y}},\sigma}^{\dagger}\hat{c}_{i,\sigma}^{\dagger}+F_{i,\sigma,\sigma}^{y-}\hat{c}_{i-\hat{\boldsymbol{y}},\sigma}^{\dagger}\hat{c}_{i,\sigma}^{\dagger}+\mathrm{h.c.}\right]\\ &= \frac{1}{2}V\sum_{\boldsymbol{k},\sigma}\Big[\big(F_{\sigma,\sigma}^{x+}e^{-ik_x}+F_{\sigma,\sigma}^{x-}e^{ik_x}+F_{\sigma,\sigma}^{y+}e^{-ik_y}+F_{\sigma,\sigma}^{y-}e^{ik_y}\big)\hat{c}_{\boldsymbol{k},\sigma}^{\dagger}\hat{c}_{-\boldsymbol{k},\sigma}^{\dagger}+\mathrm{h.c.}\Big].\end{aligned} \tag{4.11}$$

In the last line, the relation in equation (2.17) has been used leading to $\boldsymbol{k}' \to -\boldsymbol{k}$. Furthermore, the notation $F_{i,\sigma,\sigma}^{x(y)\pm} = F_{i,i\pm\hat{\boldsymbol{x}}(\hat{\boldsymbol{y}})}^{\sigma,\sigma}$ is introduced for brevity. In addition, the site index i has been removed from the paring amplitudes, reflecting that they are the same on each lattice site. The latter is because of the translational invariance in the x- and y-direction. Simplifying further, we get

$$\begin{aligned}\hat{H}_V^{\mathrm{MF}} &= \frac{1}{2}V\sum_{\boldsymbol{k},\sigma}\Big[\big(F_{\sigma,\sigma}^{x+}e^{-ik_x}+F_{\sigma,\sigma}^{x-}e^{ik_x}+F_{\sigma,\sigma}^{y+}e^{-ik_y}+F_{\sigma,\sigma}^{y-}e^{ik_y}\big)\hat{c}_{\boldsymbol{k},\sigma}^{\dagger}\hat{c}_{-\boldsymbol{k},\sigma}^{\dagger}+\mathrm{h.c.}\Big]\\ &= \frac{1}{2}V\sum_{\boldsymbol{k},\sigma}\Big[-2i\big(F_{\sigma,\sigma}^{x+}\sin k_x+F_{\sigma,\sigma}^{y+}\sin k_y\big)\hat{c}_{\boldsymbol{k},\sigma}^{\dagger}\hat{c}_{-\boldsymbol{k},\sigma}^{\dagger}+\mathrm{h.c.}\Big]\\ &= \frac{1}{2}V\sum_{\boldsymbol{k},\sigma}\left[F_{\boldsymbol{k},\sigma}\hat{c}_{\boldsymbol{k},\sigma}^{\dagger}\hat{c}_{-\boldsymbol{k},\sigma}^{\dagger}+\mathrm{h.c.}\right],\end{aligned} \tag{4.12}$$

where

$$F_{\boldsymbol{k},\sigma} = -2i(F_{\sigma,\sigma}^{x+}\sin k_x + F_{\sigma,\sigma}^{y+}\sin k_y). \tag{4.13}$$

In the derivation of equation (4.12), the fact that $F_{\sigma,\sigma}^{x(y)+} = -F_{\sigma,\sigma}^{x(y)-}$ has been used. To see this, we consider the general definition of the paring amplitudes, that is

$$\begin{aligned}F_{i,\sigma,\sigma}^{x(y)+} &= \langle c_{i,\sigma}c_{i+\hat{\boldsymbol{x}}(\hat{\boldsymbol{y}}),\sigma}\rangle\\ &= -\langle c_{i+\hat{\boldsymbol{x}}(\hat{\boldsymbol{y}}),\sigma}c_{i,\sigma}\rangle.\end{aligned} \tag{4.14}$$

The point is now that in the particular case of a homogeneous system, we can write

$$\begin{aligned}\langle c_{i+\hat{\boldsymbol{x}}(\hat{\boldsymbol{y}}),\sigma}c_{i,\sigma}\rangle &= \langle c_{i,\sigma}c_{i-\hat{\boldsymbol{x}}(\hat{\boldsymbol{y}}),\sigma}\rangle\\ &= F_{i,\sigma,\sigma}^{x(y)-}.\end{aligned} \tag{4.15}$$

4.3 Equal-spin p-wave triplets

In the following chapters, different combinations of p-wave equal-spin triplets are investigated. The paring amplitudes for these superconducting phases are defined as [52]

$$F_{p_{x(y)}}^{\sigma,\sigma} = \frac{F_{\sigma,\sigma}^{x(y)+} - F_{\sigma,\sigma}^{x(y)-}}{2} = F_{\sigma,\sigma}^{x(y)+}. \tag{4.16}$$

Here we again have used the property in equation (4.15). These p-wave paring amplitudes are related to the p_x and p_y superconducting order parameters $\Delta_{p_x}^{\sigma,\sigma}$ and $\Delta_{p_y}^{\sigma,\sigma}$ simply by

$$\Delta_{p_{x(y)}}^{\sigma,\sigma} = VF_{p_{x(y)}}^{\sigma,\sigma}. \tag{4.17}$$

4.3.1 Symmetries of the superconducting order parameters

The different symmetries of Cooper pair correlation functions can be reviewed in terms of the two-fermion anomalous Green function, which is given as [67]

$$\Delta_{\sigma,\sigma'}(\boldsymbol{r},t) = V\Big\langle \mathcal{T}_t\big(c_\sigma(\boldsymbol{r},t)c_{\sigma'}(0,0)\big)\Big\rangle. \tag{4.18}$$

Here $\mathcal{T}_t$ is the time-ordering operator ensuring that operators appear in a chronological order, with the time of the leftmost operator being the largest, that is [47]

$$\mathcal{T}_t\big(c_\sigma(\boldsymbol{r},t)c_{\sigma'}(0,0)\big) = \begin{cases} c_\sigma(\boldsymbol{r},t)c_{\sigma'}(0,0) & \text{if } t>0 \\ -c_{\sigma'}(0,0)c_\sigma(\boldsymbol{r},t) & \text{if } t<0 \end{cases}, \tag{4.19}$$

in the fermionic case. In equation (4.18), the possibility of an additional band degree of freedom for the operators is ignored as we use a single-band model of superconductivity. Further, we stress that the the position vector $\boldsymbol{r}$ and the time coordinate t are both relative quantities. Accordingly, under a permutation of the time or spatial coordinates, we will have a sign change of $\boldsymbol{r}$ and t, respectively. Nevertheless, this is not the same as the inversion of the spatial or time coordinates of the two particles forming the Cooper pair, only the relative coordinate is inverted. In context of the antisymmetry of fermionic wave functions, we require an overall parity of -1 for the superconducting correlation function, under a permutation of spin (S), spatial (P) and time (T) coordinates. This leads to the different combinations of parities summarized in table 4.1. With regards to the BCS correlation function in equation (4.5), a permutation of spins

Table 4.1: Parities for the permutation of spins (S), positions (P) and time coordinates (T). The rightmost column represents the total parity of all the permutations combined (SPT). A similar table can be found in the references [67, 68].

S	P	T	SPT
$+1$	$+1$	-1	-1
$+1$	-1	$+1$	-1
-1	$+1$	$+1$	-1
-1	-1	-1	-1

results in a sign change. This means that the S-parity is odd. The permutation of positions can equivalently be considered as a $\boldsymbol{k}$-space inversion, that is $\boldsymbol{k} \to -\boldsymbol{k}$, as the Fourier transform of the relative spatial coordinate $\boldsymbol{r}$ is the momentum. Since we are summing over all momenta $\boldsymbol{k}$, the P-parity is even. Hence, the permutation of time coordinates should be even in order to have a total parity of -1. This is fulfilled if the time coordinates of the electrons are equal, so that the time degree of freedom can be neglected. In fact, the symmetry properties of the BCS order parameter are in accordance with the third instance of table 4.1.

When it comes to the equal-spin p-wave correlations, the exchange of spins is trivially determined to be symmetric, that is a parity of $+1$. To inspect the parity for a momentum inversion, we should write the p-wave paring amplitudes in equation (6.18) on a similar form as equation (4.5) for the BCS case. This can easily be done by using the $\boldsymbol{k}$-space transformation in equation (2.14) and the relation in equation (2.17). The result is

$$F^{\sigma,\sigma}_{p_{x(y)}} = \frac{1}{N}\sum_{\boldsymbol{k}} \langle c_{\boldsymbol{k},\sigma} c_{-\boldsymbol{k},\sigma}\rangle e^{ik_{x(y)}}. \tag{4.20}$$

In comparison with the BCS case, the extra factor $e^{ik_{x(y)}}$ causes the P-parity be odd. This is in agreement with p-orbitals having orbital quantum number $l = 1$ and spatial parity of $(-1)^l = -1$. Again, the SP-product is antisymmetric, and the T-parity is then even. For this reason, we can ignore the time coordinates of the equal-spin p-wave superconducting order parameters in the following.

4.3.2 The Fourier space superconducting gap function

The group of p-wave correlations under study will have three different orbital symmetries. First of all, the pure p_x-wave symmetry will be analyzed. In the case of translational invariance in the x- and y-direction, the p_y-phase will not be considered explicitly. Additionally, we include the combined phases $p_x + ip_y$ and $p_x + p_y$ in the analysis. For a bulk superconductor, $p_x + ip_y$ will have the same free energy as $p_x - ip_y$, and the same holds for $p_x + p_y$ and $p_x - p_y$ [69]. Regarding the spin part of the p-wave phases, we distinguish between three distinct equal-spin configurations, that is $|\uparrow,\uparrow\rangle$, $|\downarrow,\downarrow\rangle$ and $|\uparrow,\uparrow\rangle + |\downarrow,\downarrow\rangle$.

In the comparison of the $\boldsymbol{k}$-space properties of p_x, $p_x + ip_y$ and $p_y + p_y$, it is interesting to examine the $\boldsymbol{k}$-space superconducting gap function $\Delta_{\boldsymbol{k}}$. To obtain the expression of this function, we first calculate the Fourier transformation of $F_{i,j}^{\sigma,\sigma}$ as

$$\begin{aligned} F_{\boldsymbol{k}}^{\sigma,\sigma} &= \frac{1}{N}\sum_{\langle i,j\rangle} F_{i,j}^{\sigma,\sigma} e^{i\boldsymbol{k}\cdot(\boldsymbol{r}_i - \boldsymbol{r}_j)} \\ &= F_{\sigma,\sigma}^{x+} e^{-ik_x} + F_{\sigma,\sigma}^{x-} e^{ik_x} + F_{\sigma,\sigma}^{y+} e^{-ik_y} + F_{\sigma,\sigma}^{y-} e^{ik_y} \\ &= -2i(F_{p_x}^{\sigma,\sigma}\sin k_x + F_{p_y}^{\sigma,\sigma}\sin k_y). \end{aligned} \tag{4.21}$$

By summing over spins and multiplying with the interaction strength V, the $\boldsymbol{k}$-space gap function for equal-spin p-wave superconductivity is [52]

$$\Delta_{\boldsymbol{k}} = -2iV\sum_{\sigma}(F_{p_x}^{\sigma,\sigma}\sin k_x + F_{p_y}^{\sigma,\sigma}\sin k_y). \tag{4.22}$$

The p_x-phase is characterized by having non-zero real part of $F_{p_x}^{\sigma,\sigma}$, $p_x + ip_y$ has finite real part of $F_{p_x}^{\sigma,\sigma}$ and imaginary part of $F_{p_y}^{\sigma,\sigma}$, and $p_x + p_y$ has significant real part of both $F_{p_x}^{\sigma,\sigma}$ and $F_{p_y}^{\sigma,\sigma}$. All the other p-wave components are zero for the respective phases. To illuminate the differences between the gap functions of the p-wave states, the absolute value of the momentum dependencies are plotted in figure 4.2. In addition, figure 4.3 shows the $\boldsymbol{k}$-space gaps when the chemical potential is set to $\mu/t = -2.5$. The extended curves go through points in Fourier space where the energy of the superconducting phase equals the absolute value of $\Delta_{\boldsymbol{k}}$ in equation (4.22). The Fermi surface is the same as for the normal conducting state, like the ones in figure 2.2. According to plot a) in figure 4.2, the p_x-phase has nodal lines at $k_x = 0, \pm\pi$. The nodal line at $k_x = 0$ is also apparent from plot a) in figure 4.3, where the $\boldsymbol{k}$-space gap becomes zero. There are no nodal lines for the $p_x + ip_y$ superconducting phase. At low chemical potentials, the gap function is approximately isotropic, as in plot b) in figure 4.3. According to figure 4.2, the $p_x + p_y$-phase has a nodal line along the diagonal $k_x = -k_y$. Thus, its gap function overlaps with the Fermi surface along this diagonal in figure 4.3.

The associated DOS are plotted in figure 4.4. We observe that $p_x + ip_y$ has a fully gapped DOS centered at grand canonical energy value $E/t = 0.0$, which corresponds to the Fermi surface. This means that there are only forbidden electron states inside the gap, while there

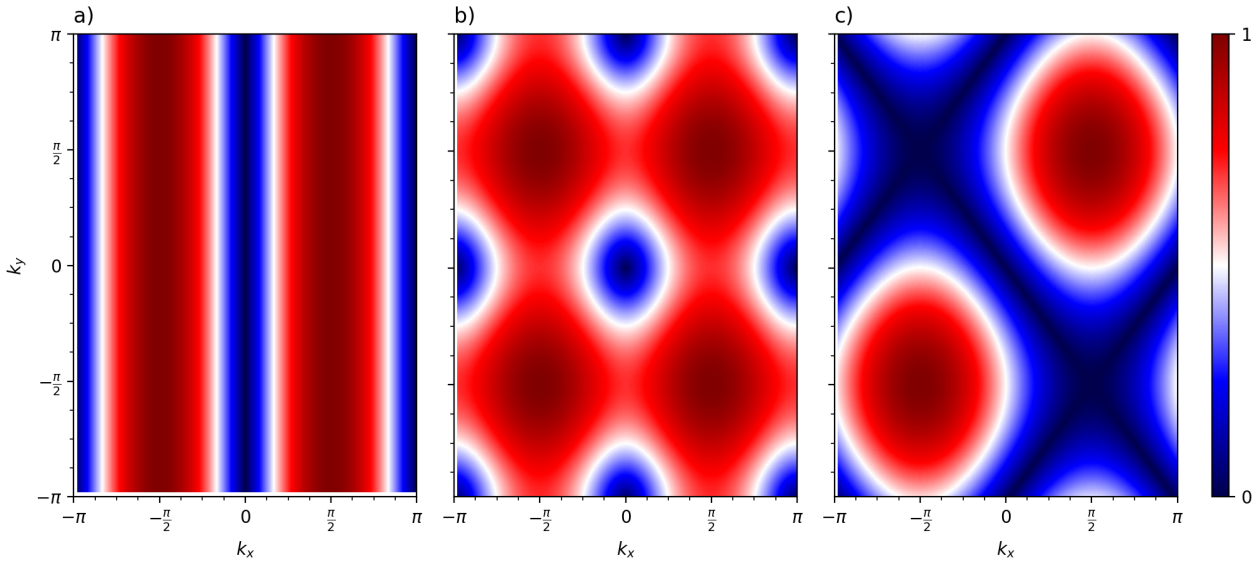

Figure 4.2: Momentum dependencies of the order parameters of the p-wave phases p_x (a), $p_x + ip_y$ (b) and $p_x + p_y$ (c). The plots are normalized with respect to the maximum $\boldsymbol{k}$-space value. The colorbar of the plots is included.

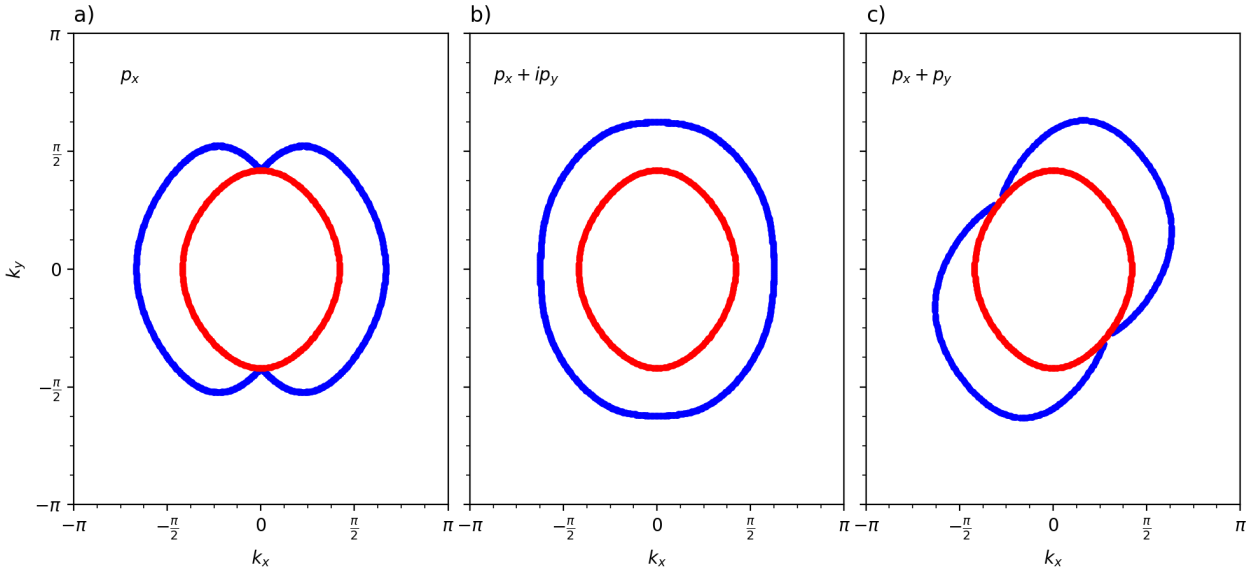

Figure 4.3: $\boldsymbol{k}$-space gap functions (blue) for p_x (a), $p_x + ip_y$ (b) and $p_x + p_y$ (c). The normal-state Fermi surface at chemical potential $\mu/t = -2.5$ is also plotted (red). The superconducting interaction strength is $V/t = -4.0$ and the temperature is $T/t = 0.0$.

are allowed states below and above the gap. The situation is different in the case of p_x- and $p_x + p_y$-wave superconductivity. For these phases, we see that the DOS are not fully gapped as there exist electron states inside the gap. In fact, the DOS decrease as the centers are approached, and the DOS are zero at $E/t = 0.0$. The V-shape of the DOS is characteristic

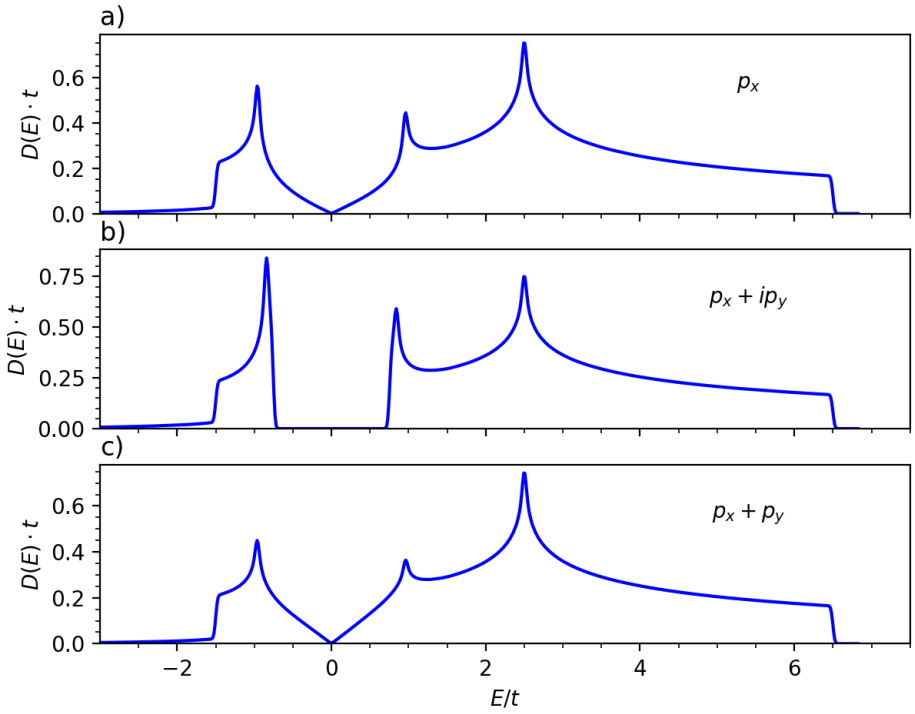

Figure 4.4: DOS of the phases p_x (a), $p_x + ip_y$ (b) and $p_x + p_y$ (c). Parameters are $\mu/t = -2.5$, $T/t = 0.0$ and $V/t = -4.0$. The axis values are in units of t.

for orbital symmetries having $\boldsymbol{k}$-space gap functions with nodal lines intersecting the Fermi surface. As we have seen, this is the case for both p_x and $p_x + p_y$.

Chapter 5

FM equal-spin p-wave superconductors in zero magnetic field

In this chapter, the theory and models from the previous chapters will be used to study FM equal-spin p-wave superconductors in zero magnetic field. We start by deriving the BdG equations of the total Hamiltonian including magnetism and superconductivity. Thereafter, the self-consistent algorithm is explained, including the strategy for obtaining phase diagrams. In the last part, the results are discussed, before some concluding remarks are given.

5.1 Total Hamiltonian and BdG equations

In order to study FM superconductors in the absence of a magnetic field, we add the second-quantized Hamiltonian terms introduced in the previous chapters. The total Hamiltonian of the FM spin-triplet system is then

$$\begin{aligned}\hat{H} = &-t\sum_{\langle i,j\rangle,\sigma}\hat{c}^{\dagger}_{i,\sigma}\hat{c}_{j,\sigma} - \mu\sum_{i,\sigma}\hat{n}_{i,\sigma} + \frac{1}{2}V\sum_{\langle i,j\rangle,\sigma}\hat{n}_{i,\sigma}\hat{n}_{j,\sigma} - h\sum_{i}(\hat{n}_{i,\uparrow}-\hat{n}_{i,\downarrow}) \\ &+ U\sum_{i}\hat{n}_{i,\uparrow}\hat{n}_{i,\downarrow}.\end{aligned} \tag{5.1}$$

The parameters of this equation have been defined previously. Since the two last terms in this Hamiltonian can be used to model the FM state as explained in chapter 3, we will distinguish between the two cases $h \neq 0, U = 0$ and $h = 0, U \neq 0$. Furthermore, the total mean-field Hamiltonian is

$$\begin{aligned}\hat{H} = &-t\sum_{\langle i,j\rangle,\sigma}\hat{c}^{\dagger}_{i,\sigma}\hat{c}_{j,\sigma} - \mu\sum_{i,\sigma}\hat{n}_{i,\sigma} + \frac{1}{2}V\sum_{\langle i,j\rangle,\sigma}\left[F^{\sigma\sigma}_{i,j}\hat{c}^{\dagger}_{j,\sigma}\hat{c}^{\dagger}_{i,\sigma} + \text{h.c.}\right] \\ &- h\sum_{i}(\hat{n}_{i,\uparrow}-\hat{n}_{i,\downarrow}) + U\sum_{i,\sigma}\langle n_{\bar{\sigma}}\rangle\hat{n}_{i,\sigma},\end{aligned} \tag{5.2}$$

where we have neglected the constant terms E_U (equation (3.12)) and E_V (equation (4.9)). This can be done in the search for the BdG equations as constants do not contribute in the determination of eigenvalues and eigenvectors. The definition of the equal-spin paring amplitude $F^{\sigma,\sigma}_{i,j}$ is given in equation (4.10). Using the Fourier transforms derived earlier in this thesis, the

$\boldsymbol{k}$-space form of $\hat{H}$ is

$$\begin{aligned}\hat{H} =& \sum_{\boldsymbol{k},\sigma} \epsilon_{\boldsymbol{k}} \hat{c}^{\dagger}_{\boldsymbol{k},\sigma} \hat{c}_{\boldsymbol{k},\sigma} + \frac{1}{2} V \sum_{\boldsymbol{k},\sigma} \left[F_{\boldsymbol{k},\sigma} \hat{c}^{\dagger}_{\boldsymbol{k},\sigma} \hat{c}^{\dagger}_{-\boldsymbol{k},\sigma} + \text{h.c.} \right] \\ & - h \sum_{\boldsymbol{k}} (\hat{c}^{\dagger}_{\boldsymbol{k},\uparrow} \hat{c}_{\boldsymbol{k},\uparrow} - \hat{c}^{\dagger}_{\boldsymbol{k},\downarrow} \hat{c}_{\boldsymbol{k},\downarrow}) + U \sum_{\boldsymbol{k},\sigma} \hat{c}^{\dagger}_{\boldsymbol{k},\sigma} \hat{c}_{\boldsymbol{k},\sigma} \langle n_{\bar{\sigma}} \rangle,\end{aligned} \tag{5.3}$$

where $\epsilon_{\boldsymbol{k}}$ is the tight-binding energy in equation (2.18), and the definition of $F_{\boldsymbol{k},\sigma}$ is given in equation (4.13). In this Hamiltonian, the up- and down-spin creation and annihilation operators are not coupled. Therefore, we define the spinor

$$\hat{\boldsymbol{D}}_{\boldsymbol{k},\sigma} = \begin{pmatrix} \hat{c}_{\boldsymbol{k},\sigma} \\ \hat{c}^{\dagger}_{-\boldsymbol{k},\sigma} \end{pmatrix}, \tag{5.4}$$

and express equation (5.3) on matrix form as

$$\hat{H} = \frac{1}{2} \sum_{\boldsymbol{k},\sigma} \hat{\boldsymbol{D}}^{\dagger}_{\boldsymbol{k},\sigma} \boldsymbol{H}_{\boldsymbol{k},\sigma} \hat{\boldsymbol{D}}_{\boldsymbol{k},\sigma}, \tag{5.5}$$

where

$$\boldsymbol{H}_{\boldsymbol{k},\sigma} = \begin{pmatrix} \epsilon_{\boldsymbol{k}} - \sigma h + U \langle n_{\bar{\sigma}} \rangle & V F_{\boldsymbol{k},\sigma} \\ V F^{*}_{\boldsymbol{k},\sigma} & -\epsilon_{\boldsymbol{k}} + \sigma h - U \langle n_{\bar{\sigma}} \rangle \end{pmatrix}. \tag{5.6}$$

In equation (5.6), $\sigma = 1$ and $\sigma = -1$ in the up- and down-spin case, respectively. The analytical eigenvalues of this matrix can easily be derived, which is done in appendix A.1. Yet, in the self-consistent algorithm, we will diagonalize $\boldsymbol{H}_{\boldsymbol{k},\sigma}$ by a Bogoliubov transformation of the creation and annihilation c-operators to a new set of operators, the so-called Bogoliubov quasiparticle α-operators. The transformations are given as [52]

$$\hat{c}_{\boldsymbol{k},\sigma} = \sum_{n} u_{n,\boldsymbol{k},\sigma} \hat{\alpha}_{n,\boldsymbol{k},\sigma} \tag{5.7}$$

$$\hat{c}^{\dagger}_{-\boldsymbol{k},\sigma} = \sum_{n} v_{n,\boldsymbol{k},\sigma} \hat{\alpha}_{n,\boldsymbol{k},\sigma}. \tag{5.8}$$

Moreover, we have

$$\hat{\alpha}_{n,\boldsymbol{k},\sigma} = u_{n,\boldsymbol{k},\sigma} \hat{c}_{\boldsymbol{k},\sigma} + v_{n,\boldsymbol{k},\sigma} \hat{c}^{\dagger}_{-\boldsymbol{k},\sigma}. \tag{5.9}$$

In the Bogoliubov transformations, $u_{n,\boldsymbol{k},\sigma}$, $v_{n,\boldsymbol{k},\sigma}$ are referred to as coherence factors. According to equation (5.9), the Bogoliubov annihilation operator $\alpha_{n,\boldsymbol{k},\sigma}$ is a linear combination of electronic creation and annihilation operators. Equivalently, this can be considered as a linear combination of annihilation operators for electrons and holes. Thus, the coherence factors are amplitudes determining the electron- and hole-like nature of the Bogoliubov quasiparticles. The resulting eigenvalue problem, that is the BdG equations, can be expressed

$$\boldsymbol{H}_{\boldsymbol{k},\sigma} \boldsymbol{A}_{n,\boldsymbol{k},\sigma} = E_{n,\boldsymbol{k},\sigma} \boldsymbol{A}_{n,\boldsymbol{k},\sigma}, \tag{5.10}$$

where

$$\boldsymbol{A}_{n,\boldsymbol{k},\sigma} = \begin{pmatrix} u_{n,\boldsymbol{k},\sigma} \\ v_{n,\boldsymbol{k},\sigma} \end{pmatrix}, \tag{5.11}$$

are eigenvectors and $E_{n,\boldsymbol{k},\sigma}$ are eigenvalues of $\boldsymbol{H}_{\boldsymbol{k},\sigma}$ $(n = 1, 2)$.

5.2 Numerical procedure

In this section, the numerical procedures for the computation of phase diagrams are outlined. Additionally, it is demonstrated how the DOS in the grand canonical ensemble can be computed by deriving the spectral function.

5.2.1 Self-consistent solution

Considering the matrices $\boldsymbol{H}_{\boldsymbol{k},\sigma}$, the electron densities $\langle n_\sigma \rangle$ are not known from the outset. This is also the case for the paring amplitudes $F^{x+}_{\sigma,\sigma}$ and $F^{y+}_{\sigma,\sigma}$, which are included in $F_{\boldsymbol{k},\sigma}$. However, the eigenvalue problem can be solved self-consistently. The procedure is shown as a flowchart diagram in figure 5.1. First of all, initial conditions of all the average number operators and

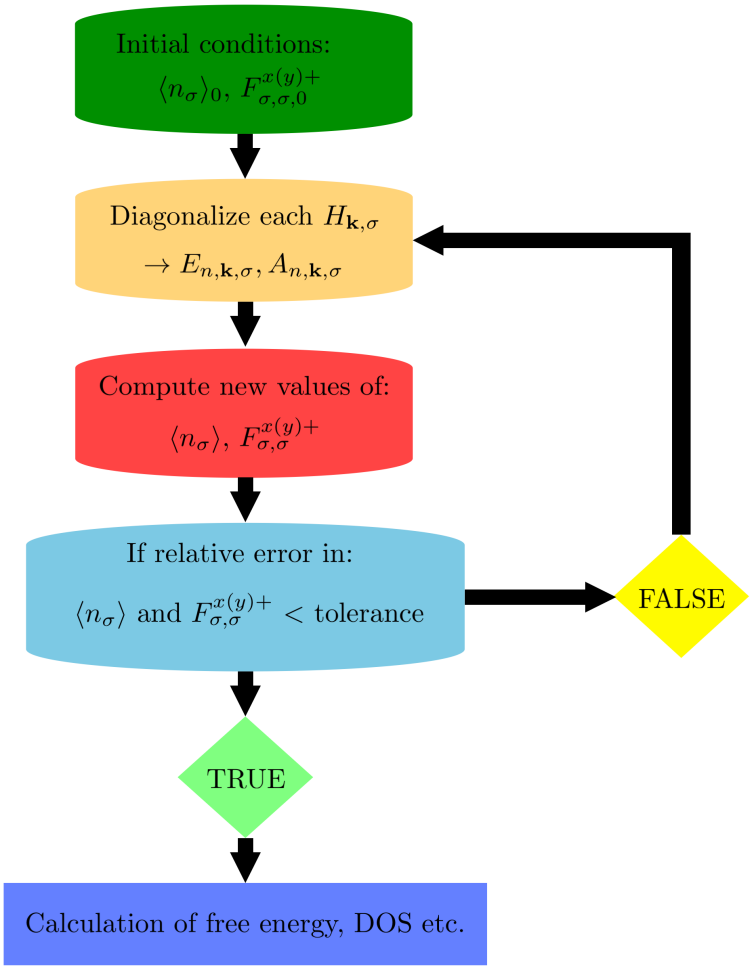

Figure 5.1: Schematic illustration of the steps in the self-consistent procedure. The order of the different steps is demonstrated by the arrows.

the paring amplitudes are set. In the case of the exchange field term instead of the Hubbard U-term, the electron densities are of course not included in the algorithm. Since we are interested in FM superconductors, we initialize the U-term with $\langle n_\uparrow \rangle > \langle n_\downarrow \rangle$, that is a higher number

of up- than down-spin electrons and a net magnetization (equation (3.19)) in the system. As outlined in section 4.3, we will be interested in the p-wave orbital symmetries p_x, $p_x + ip_y$ and $p_x + p_y$. The equal-spin triplets under study will be the single spin configurations $|\uparrow,\uparrow\rangle$ and $|\downarrow,\downarrow\rangle$ in addition to the combined configuration $|\uparrow,\uparrow\rangle + |\downarrow,\downarrow\rangle$. The initial conditions of the paring amplitudes are then chosen in accordance with table 5.1. For instance, the phase

Table 5.1: Start values of the pairing amplitudes $F^{x(y)+}_{\sigma,\sigma}$ in the self-consistent algorithm.

Equal-spin p-wave phase	$F^{x+}_{\uparrow,\uparrow}$	$F^{y+}_{\uparrow,\uparrow}$	$F^{x+}_{\downarrow,\downarrow}$	$F^{y+}_{\downarrow,\downarrow}$
$p_x\|\uparrow,\uparrow\rangle$	1	0	0	0
$(p_x + ip_y)\|\uparrow,\uparrow\rangle$	1	i	0	0
$(p_x + p_y)\|\uparrow,\uparrow\rangle$	1	1	0	0
$p_x\|\downarrow,\downarrow\rangle$	0	0	1	0
$(p_x + ip_y)\|\downarrow,\downarrow\rangle$	0	0	1	i
$(p_x + p_y)\|\downarrow,\downarrow\rangle$	0	0	1	1
$p_x(\|\uparrow,\uparrow\rangle + \|\downarrow,\downarrow\rangle)$	1	0	1	0
$(p_x + ip_y)(\|\uparrow,\uparrow\rangle + \|\downarrow,\downarrow\rangle)$	1	i	1	i
$(p_x + p_y)(\|\uparrow,\uparrow\rangle + \|\downarrow,\downarrow\rangle)$	1	1	1	1

$(p_x + ip_y)(|\uparrow,\uparrow\rangle + |\downarrow,\downarrow\rangle)$ is initialized so that $\mathrm{Re}[F^{\uparrow,\uparrow}_{p_x}]$, $\mathrm{Re}[F^{\downarrow,\downarrow}_{p_x}]$, $\mathrm{Im}[F^{\uparrow,\uparrow}_{p_y}]$ and $\mathrm{Im}[F^{\uparrow,\uparrow}_{p_y}]$ are non-zero, and the other real and imaginary parts are zero. This gives finite real part of the up- and down-spin Δ_{p_x} and finite imaginary part of the up- and down-spin Δ_{p_y}, as required.

After the initialization of the unknowns in $\boldsymbol{H}_{\boldsymbol{k},\sigma}$, the matrices are diagonalized in order to obtain eigenvalues and eigenvectors. For a lattice containing N sites, there are N distinct momenta $\boldsymbol{k}$ in the first Brillouin zone. This means that $2N$ 2×2 matrices have to diagonalized, leading to $2N$ eigenvalues and eigenvectors.

The next step in the self-consistent procedure is to compute new values of the average number operators and the paring amplitudes. We first look at how the average number operators can be calculated. Starting from the definition of the number operator $\langle n_{i,\sigma}\rangle$, we get

$$\begin{aligned}\langle n_{i,\sigma}\rangle =& \langle c^\dagger_{i,\sigma} c_{i,\sigma}\rangle \\ =& \frac{1}{N}\sum_{\boldsymbol{k},\boldsymbol{k}'}\langle c^\dagger_{\boldsymbol{k},\sigma} c_{\boldsymbol{k}',\sigma}\rangle e^{-i(\boldsymbol{k}-\boldsymbol{k}')\cdot\boldsymbol{r}_i}.\end{aligned} \tag{5.12}$$

Averaging over all sites i and inserting the Bogoliubov transformation in equation (5.7), give

$$\begin{aligned}\langle n_\sigma\rangle =& \frac{1}{N}\sum_i \frac{1}{N}\sum_{\boldsymbol{k},\boldsymbol{k}'}\langle c^\dagger_{\boldsymbol{k},\sigma} c_{\boldsymbol{k}',\sigma}\rangle e^{-i(\boldsymbol{k}-\boldsymbol{k}')\cdot\boldsymbol{r}_i} \\ =& \frac{1}{N}\sum_{\boldsymbol{k}}\langle c^\dagger_{\boldsymbol{k},\sigma} c_{\boldsymbol{k},\sigma}\rangle \\ =& \frac{1}{N}\sum_{\boldsymbol{k}}\sum_{n,n'} u^*_{n,\boldsymbol{k},\sigma} u_{n',\boldsymbol{k},\sigma}\langle \alpha^\dagger_{n,\boldsymbol{k},\sigma}\alpha_{n',\boldsymbol{k},\sigma}\rangle \\ =& \frac{1}{N}\sum_{n,\boldsymbol{k}} |u_{n,\boldsymbol{k},\sigma}|^2 f(E_{n,\boldsymbol{k},\sigma}),\end{aligned} \tag{5.13}$$

where f is the Fermi function. In the last step, we have used that the α-operators are fermionic, so that

$$\langle \alpha^{\dagger}_{n,\boldsymbol{k},\sigma}\alpha_{n',\boldsymbol{k},\sigma}\rangle = f(E_{n,\boldsymbol{k},\sigma})\delta_{n,n'}. \tag{5.14}$$

In a similar way, it can be shown that the expression for the pairing amplitudes is

$$F^{x(y)\pm}_{\sigma,\sigma} = \frac{1}{N}\sum_{n,\boldsymbol{k}} u_{n,\boldsymbol{k},\sigma}v^{*}_{n,\boldsymbol{k},\sigma}\big(1-f(E_{n,\boldsymbol{k},\sigma})\big)e^{\mp ik_{x(y)}}. \tag{5.15}$$

Finally, the new values of the magnetic and superconducting order parameters are compared to the previous ones. If the relative error in one of the number densities or paring amplitudes are greater than the tolerance, the self-consistent iteration continues. Otherwise, the eigenvalue problem has been solved numerically.

5.2.2 Free energy

The computation of phase diagrams is based on the minimization of the free energy. For a given set of input parameters, the phase present in the diagram will be the one having lowest free energy. We therefore seek an expression relating the free energy to the calculated eigenvalues and eigenvectors. Bearing in mind that the Hamiltonian is given in the grand canonical ensemble, we use the thermodynamical relation between the grand canonical partition function Z and the free energy F, that is

$$F = -T\ln Z, \tag{5.16}$$

where the Boltzmann constant is not included ($k_{\mathrm{B}} = 1$). The partition function can be related to the Hamiltonian as [47]

$$Z = \mathrm{Tr}\Big\{e^{-\hat{H}/T}\Big\}. \tag{5.17}$$

It is now convenient to write the Hamiltonian in terms of the Bogoliubov quasiparticle operators. Transforming the spinors to this representation, gives

$$\begin{aligned}\hat{H} &= E_V + E_U + \frac{1}{2}\sum_{\boldsymbol{k},\sigma}\hat{\boldsymbol{D}}^{\dagger}_{\boldsymbol{k},\sigma}\boldsymbol{H}_{\boldsymbol{k},\sigma}\hat{\boldsymbol{D}}_{\boldsymbol{k},\sigma}\\ &= E_V + E_U + \frac{1}{2}\sum_{\boldsymbol{k},\sigma}(\boldsymbol{P}_{\boldsymbol{k},\sigma}\hat{\boldsymbol{D}}_{\boldsymbol{k},\sigma})^{\dagger}(\boldsymbol{P}_{\boldsymbol{k},\sigma}\boldsymbol{H}_{\boldsymbol{k},\sigma}\boldsymbol{P}^{\dagger}_{\boldsymbol{k},\sigma})(\boldsymbol{P}_{\boldsymbol{k},\sigma}\hat{\boldsymbol{D}}_{\boldsymbol{k},\sigma})\\ &= E_V + E_U + \frac{1}{2}\sum_{n,\boldsymbol{k},\sigma}E_{n,\boldsymbol{k},\sigma}\hat{\alpha}^{\dagger}_{n,\boldsymbol{k},\sigma}\hat{\alpha}_{n,\boldsymbol{k},\sigma},\end{aligned} \tag{5.18}$$

where $\boldsymbol{P}_{\boldsymbol{k},\sigma}$ is the transformation matrix. Inserting this into equation (5.17), the expression of Z is

$$\begin{aligned} Z &= \mathrm{Tr}\left\{ e^{-(E_V+E_U)/T} \prod_{n,\boldsymbol{k},\sigma} e^{-E_{n,\boldsymbol{k},\sigma}\hat{n}_{n,\boldsymbol{k},\sigma}/2T} \right\} \\ &= e^{-(E_V+E_U)/T} \prod_{n,\boldsymbol{k},\sigma} \mathrm{Tr}\left\{ e^{-E_{n,\boldsymbol{k},\sigma}\hat{n}_{n,\boldsymbol{k},\sigma}/2T} \right\} \\ &= e^{-(E_V+E_U)/T} \prod_{n,\boldsymbol{k},\sigma} \sum_{n_{n,\boldsymbol{k},\sigma}=0,1} e^{-E_{n,\boldsymbol{k},\sigma}\hat{n}_{n,\boldsymbol{k},\sigma}/2T} \\ &= e^{-(E_V+E_U)/T} \prod_{n,\boldsymbol{k},\sigma} \left(1 + e^{-E_{n,\boldsymbol{k},\sigma}/2T}\right). \end{aligned} \tag{5.19}$$

Thus, the free energy can be expressed as

$$F = E_V + E_U - T \sum_{n,\boldsymbol{k},\sigma} \ln\left(1 + e^{-E_{n,\boldsymbol{k},\sigma}/2T}\right). \tag{5.20}$$

Here the critical limit is $T/t \to 0$ as the exponential becomes infinite for negative eigenvalues. For such energies, the logarithm can be approximated as

$$\ln\left(1 + e^{-E_{n,\boldsymbol{k},\sigma}/2T}\right) \approx -E_{n,\boldsymbol{k},\sigma}/2T. \tag{5.21}$$

In particular, the free energy at $T/t = 0.0$, which is the ground state energy, is half the sum of all the negative energy eigenvalues and the constant terms E_V and E_U.

5.2.3 Phase diagrams

Taking into account the two magnetic states (PM and FM) and the 9 possible superconducting p-phases in addition to the normal conducting state, there are in total 20 different phases to compare in the free energy minimization procedure. In general, a transition from one phase to another will be found as the intersection of the free energy curves of the two phases having the lowest free energy of all states on opposite sides of the intersection point. However, there are exceptions to this method if the free energy of one phase converges to, but do not intersect the free energy of another phase. This can for instance happen in a transition from a superconducting phase to the normal conducting state, in which the paring amplitudes become very small. To find the transition point, the absolute value of superconducting order parameters, that is $|VF|$, is compared to the hopping amplitude t, which is the relevant energy scale of the system. When each of the paring amplitudes satisfies $|VF| < 1.0\text{E-}4t$, we define a transition to the non-superconducting state. Similarly, the criterion for a FM-PM transition is $U|M| < 1.0\text{E-}4t$. This means that the magnetic order parameter M multiplied with the magnetic interaction strength U, is required to be smaller than $1.0\text{E-}4t$. Using the exchange field to model the FM state, the transition to PM does not occur.

Because of the high number of possible states, the free energy curves of all the phases will be compared simultaneously as in figure 5.2. Such plots show where we have critical regions, like intersections and convergences. To increase the resolution in the determination of phase transitions, the bisection method has been used with a tolerance in temperature of $1.0\text{E-}3t$. For instance, in the zoomed window of figure 5.2, we observe that there is a transition from

$(p_x+ip_y)(|\uparrow,\uparrow\rangle+|\downarrow,\downarrow\rangle)$ (blue) to $(p_x+ip_y)|\uparrow,\uparrow\rangle$ (red), as the temperature has increased from $T/t = 0.27$ to $T/t = 0.29$. Thus, the bisection method on that interval can be used to find the phase transition point. Another possibility could have been to apply the bisection method throughout the minimization procedure. On the other hand, the problem is that the method only compares two phases at a time, which makes it cumbersome to use in the comparison of a large number of phases.

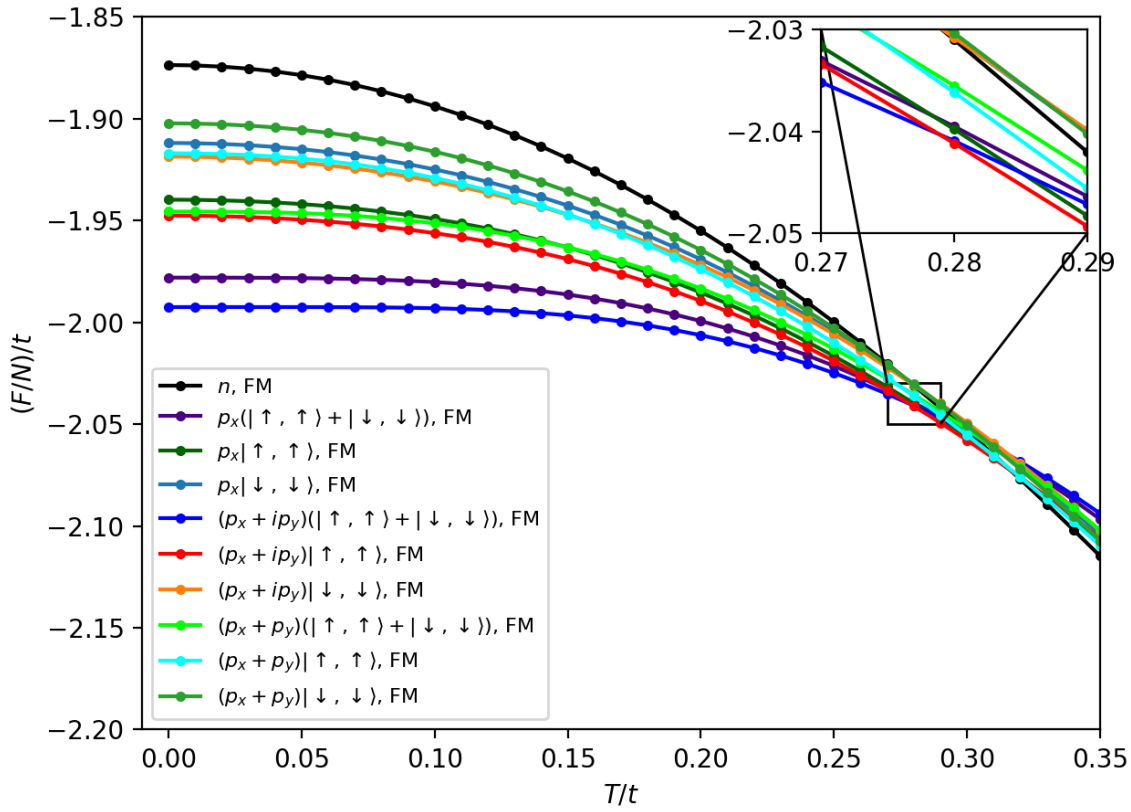

Figure 5.2: Free energy per site in units of t ($(F/N)/t$) on a limited temperature interval in the case of $h/t = 0.5$, $U/t = 0$, $V/t = -4.0$ and $\mu/t = -2.0$. All possible phases are in the FM state because of the exchange field. In this figure, the normal conducting state is labeled as n.

5.2.4 Density of states

The DOS can be computed knowing the eigenvalues and eigenvectors of the Hamiltonian. In this thesis, we are interested in the DOS of up- and down-spin electrons as they will be useful in the discussion of the phase diagrams. The spectral function $A(\boldsymbol{k}, \sigma, E)$, which can be interpreted as a probability density function for quasiparticles having quantum numbers $\boldsymbol{k}, \sigma, E$, is related to the DOS as

$$D(E) = \frac{1}{N}\sum_{\boldsymbol{k},\sigma} A(\boldsymbol{k}, \sigma, E), \tag{5.22}$$

and

$$A(\boldsymbol{k},\sigma,E) = -\frac{1}{\pi}\mathrm{Im}\big[G^{\mathrm{R}}(\boldsymbol{k},\sigma,E)\big]. \tag{5.23}$$

The objective is then to find an expression of the retarded Green function $G^{\mathrm{R}}(\boldsymbol{k},\sigma,E)$. This function is defined as

$$G^{\mathrm{R}}(\boldsymbol{k},\sigma,t) = -i\theta(t)\langle\{c_{\boldsymbol{k},\sigma}(t), c^{\dagger}_{\boldsymbol{k},\sigma}(0)\}\rangle, \tag{5.24}$$

where $\theta(t)$ is the step function, which leads to zero contribution when $t < 0$. We now transform the creation and annihilation operators to the Bogoliubov basis. This gives

$$\begin{aligned}\langle\{c_{\boldsymbol{k},\sigma}(t), c^{\dagger}_{\boldsymbol{k},\sigma}(0)\}\rangle = \sum_{n,n'} \big(&u_{n,\boldsymbol{k},\sigma}u^{*}_{n',\boldsymbol{k},\sigma}\langle\alpha_{n,\boldsymbol{k},\sigma}(t)\alpha^{\dagger}_{n',\boldsymbol{k},\sigma}(0)\rangle \\ &+ u^{*}_{n,\boldsymbol{k},\sigma}u_{n',\boldsymbol{k},\sigma}\langle\alpha^{\dagger}_{n,\boldsymbol{k},\sigma}(0)\alpha_{n',\boldsymbol{k},\sigma}(t)\rangle\big).\end{aligned} \tag{5.25}$$

Because it can be shown that $\alpha_{n,\boldsymbol{k},\sigma}(t) = \alpha_{n,\boldsymbol{k},\sigma}(0)e^{-iE_{n,\boldsymbol{k},\sigma}t}$ [47], the quantum mechanical thermal average is

$$\langle\{c_{\boldsymbol{k},\sigma}(t), c^{\dagger}_{\boldsymbol{k},\sigma}(0)\}\rangle = \sum_{n} |u_{n,\boldsymbol{k},\sigma}|^2 e^{-iE_{n,\boldsymbol{k},\sigma}t}. \tag{5.26}$$

Here we have also used the property in equation (5.14). The next step is to transform the time coordinate of $G^{\mathrm{R}}(\boldsymbol{k},\sigma,t)$ to energy space by calculating the integral

$$G^{\mathrm{R}}(\boldsymbol{k},\sigma,E) = \int_{-\infty}^{\infty} G^{\mathrm{R}}(\boldsymbol{k},\sigma,t)e^{iEt}dt. \tag{5.27}$$

This gives

$$G^{\mathrm{R}}(\boldsymbol{k},\sigma,E) = \sum_{n} \frac{|u_{n,\boldsymbol{k},\sigma}|^2}{E - E_{n,\boldsymbol{k},\sigma} + i\eta}. \tag{5.28}$$

Finally, applying the relation $\mathrm{Im}\frac{1}{x+i\eta} = -\pi\delta(x)$, leads to

$$A(\boldsymbol{k},\sigma,E) = \sum_{n} |u_{n,\boldsymbol{k},\sigma}|^2 \delta(E - E_{n,\boldsymbol{k},\sigma}), \tag{5.29}$$

and

$$D_{\sigma}(E) = \frac{1}{N}\sum_{n,\boldsymbol{k}} |u_{n,\boldsymbol{k},\sigma}|^2 \delta(E - E_{n,\boldsymbol{k},\sigma}). \tag{5.30}$$

In the numerical calculation of the DOS, the δ-functions are approximated as normalized Gaussian functions with a small standard deviation equal to $0.06t$.

5.2.5 Hubbard U-term

Owing to the symmetry of the Hubbard U-term for a fixed U, the free energy of phases in the spin state $|\uparrow,\uparrow\rangle$ with magnetization $M = |M_0|$ is the same as in the spin state $|\downarrow,\downarrow\rangle$ with $M = -|M_0|$. Indeed, if we initialize $|\uparrow,\uparrow\rangle$-states with $\langle n_{\uparrow}\rangle > \langle n_{\downarrow}\rangle$ and $|\downarrow,\downarrow\rangle$-states with $\langle n_{\uparrow}\rangle < \langle n_{\downarrow}\rangle$, the phases will be degenerate in free energy. The point is that even if we start with $\langle n_{\uparrow}\rangle > \langle n_{\downarrow}\rangle$, the self-consistent algorithm for down-spin phases converges to solutions with negative magnetization. Therefore, the case of finite U will be treated using $M > 0$ as initial condition, and only the spin configurations $|\uparrow,\uparrow\rangle$ and $|\uparrow,\uparrow\rangle + |\downarrow,\downarrow\rangle$ are included in the analysis. This is not a concern when having a non-zero exchange field as the sign of the magnetization is determined by h.

5.3 Results and discussion

The phase diagrams are obtained for a 100×100 square lattice, and the relative iteration tolerance is 1.0E-5 for the average number operators and the paring amplitudes.

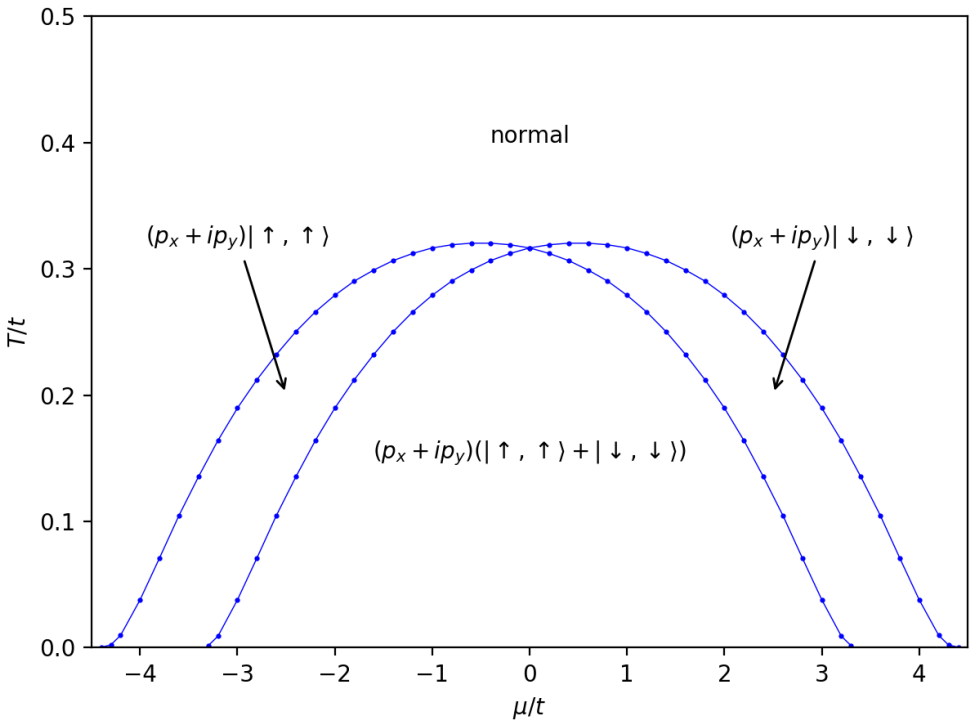

Figure 5.3: μ-T phase diagram for $h/t = 0.5$ and $V/t = -4.0$. The phases in the diagram are named with respect to the superconducting properties as FM order is present for all the states. The interval $\mu/t = [-4.5, 4.5]$ corresponds to all electron densities from minimal to maximal degree of filling.

The computed phase diagram with non-zero exchange field h is shown in figure 5.3. According to this figure, the most stable superconducting phase has the $p_x + ip_y$ momentum symmetry. At the phase transitions to the normal conducting phase, the free energies of all the superconducting states become higher. This is not found to be a result of the superconductivity being completely destroyed. For instance, the self-consistent solution of $(p_x + ip_y)(|\uparrow,\uparrow\rangle + |\downarrow,\downarrow\rangle)$ at $\mu/t = 0.0$ gives significant superconducting order parameters up to the temperature $T/t = 0.77$. As a matter of fact, it is energetically favourable for the system to enter the FM state without superconductivity when the temperature is higher than a certain level. At which temperatures this happens, is expressed by the phase diagram. To explain this, we have to consider the effect of both the magnetic and the superconducting interactions on the stability of the system. In the case of the exchange field term, the contribution of magnetism to the free energy is determined by the magnetization. The magnitudes of the superconducting order parameters are decisive for the influence of superconductivity on the free energy. Intuitively, one might think that having both the magnetic and superconducting order present in the system, will give the state of lowest free energy. Yet, this is not always the case. For a given chemical potential, the self-consistent solution gives higher degree of FM order in the normal conducting state than

in the superconducting state. The point is that with higher thermal energy in the system, both the magnetization and the superconductivity decay. As the temperature is increased, the lowering of the free energy because of superconductivity eventually becomes smaller than the reduction caused be the higher magnetization in the normal conducting state.

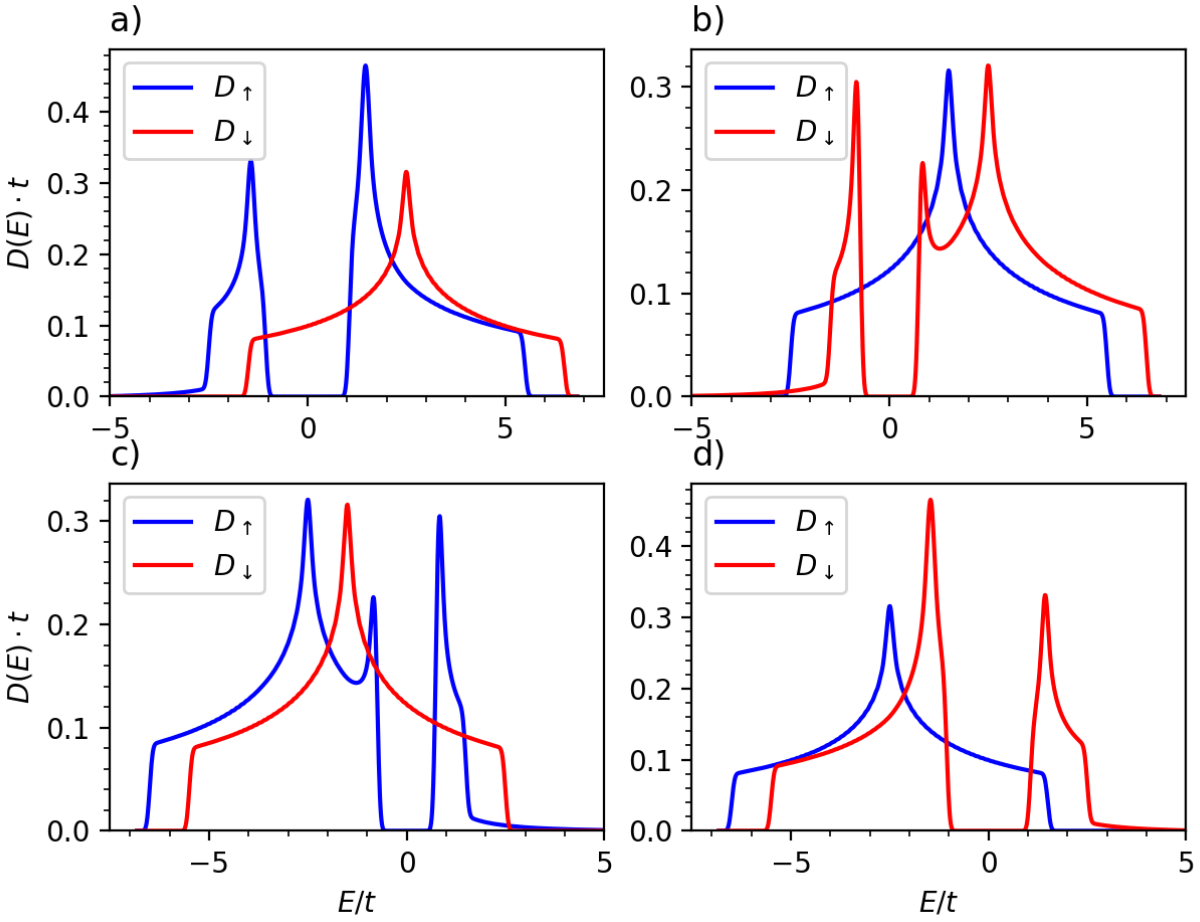

Figure 5.4: Up- ($D_\uparrow$) and down-spin DOS ($D_\downarrow$) of $(p_x + ip_y)|\uparrow,\uparrow\rangle$ (a and c) and $(p_x + ip_y)|\downarrow,\downarrow\rangle$ (b and d). Chemical potentials are $\mu/t = -2.0$ (a and b) and $\mu/t = 2.0$ (c and d), and the temperature is $T/t = 0.2$.

As predicted in chapter 3, the phase diagram is not symmetric about half-filling at $\mu/t = 0.0$, as the exchange field term does not obey the particle-hole symmetry. However, if we shift the sign of the exchange field for a symmetric point about half-filling, the most stable phase will be the same. In figure 5.3, the result is that the down-spin state has lowest free energy at high degree of filling and the up-spin state is the most stable at low electron densities. Between these regions, both spin directions are present in the superconducting state. Figure 5.4 illuminates the relation between $(p_x + ip_y)|\uparrow,\uparrow\rangle$ and $(p_x + ip_y)|\downarrow,\downarrow\rangle$. First of all, we observe that the up-spin DOS ($D_\uparrow$) is located at lower energy values than the down-spin DOS ($D_\downarrow$). Thus, the positive exchange field splits the spin bands, favoring the occupation of up-spin states. The effect is that a higher number of electrons have spin up than down, causing FM order in the system. Furthermore, due to the fact that the spin configurations $|\uparrow,\uparrow\rangle$ and $|\downarrow,\downarrow\rangle$ do not couple the up- and down-spin, they only have a superconducting gap in one of the spin

bands, respectively the up- and down-spin band. Comparing plots a) and b) in figure 5.4 at $\mu/t = -2.0$, we see that the superconducting gap in $D_\uparrow$ is larger for $(p_x + ip_y)|\uparrow,\uparrow\rangle$ than the gap in $D_\downarrow$ for $(p_x + ip_y)|\downarrow,\downarrow\rangle$. Hence, the free energy of the up-spin phase is lower than the down-spin phase, so that $(p_x + ip_y)|\uparrow,\uparrow\rangle$ is the preferred state.

It is now interesting to look at what happens with the DOS of $(p_x + ip_y)|\uparrow,\uparrow\rangle$ at the symmetric chemical potential value $\mu/t = 2.0$. As evident from plot c), the up-spin DOS is the same as the down-spin DOS of $(p_x + ip_y)|\downarrow,\downarrow\rangle$ at $\mu/t = -2.0$ in plot b), as long as it is reflected about the chemical potential level at $E/t = 0.0$. The same is true for $D_\downarrow$ of $(p_x + ip_y)|\uparrow,\uparrow\rangle$ with respect to $D_\uparrow$ of $(p_x + ip_y)|\downarrow,\downarrow\rangle$. Considering plots a) and d), this symmetry also holds for $(p_x+ip_y)|\uparrow,\uparrow\rangle$ at $\mu/t = -2.0$ compared to $(p_x+ip_y)|\downarrow,\downarrow\rangle$ at $\mu/t = 2.0$. Accordingly, the most stable state has opposite spin configuration at $\mu/t = 2.0, T/t = 0.2$ relative to $\mu/t = -2.0, T/t = 0.2$.

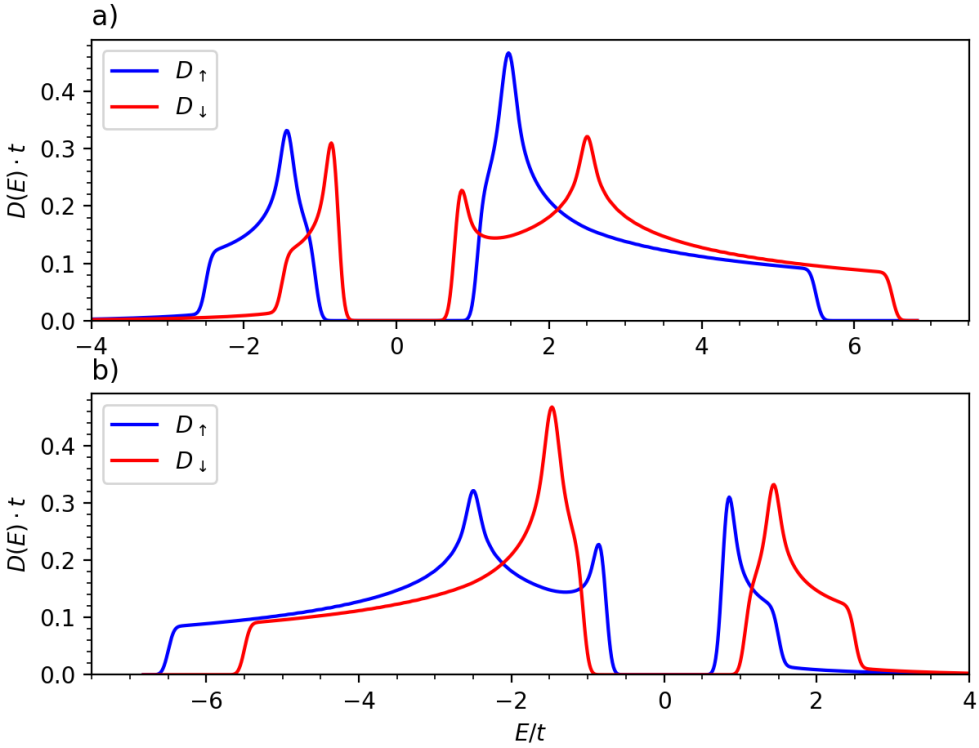

Figure 5.5: $D_\uparrow$ and $D_\downarrow$ of $(p_x+ip_y)(|\uparrow,\uparrow\rangle+|\downarrow,\downarrow\rangle)$ for chemical potentials $\mu/t = -2.0$ (a) and $\mu/t = 2.0$ (b). The value of the temperature is $T/t = 0.0$.

The phase diagram indicates that by reducing the temperature from about $T/t = 0.2$ at $\mu/t = \pm 2.0$, $(p_x + ip_y)(|\uparrow,\uparrow\rangle + |\downarrow,\downarrow\rangle)$ becomes the state of highest stability. When it comes to the stability of this phase relative to $(p_x + ip_y)|\uparrow,\uparrow\rangle$ and $(p_x + ip_y)|\downarrow,\downarrow\rangle$, we must again find out whether it is the magnetism or superconductivity that dominates the free energy. As evident from figure 5.5, superconducting phases with spin configuration $|\uparrow,\uparrow\rangle + |\downarrow,\downarrow\rangle$ have gaps in both spin bands. Arguably, this is energetically preferable instead of having a gap in just one of them. Nonetheless, it turns out that the free energy can be reduced even more by the FM order in the system. This is what happens in figure 5.3. For instance, at $\mu/t = -2.0$, the magnetization of $(p_x+ip_y)|\uparrow,\uparrow\rangle$ is greater than $(p_x+ip_y)(|\uparrow,\uparrow\rangle+|\downarrow,\downarrow\rangle)$ for both $T/t = 0.0$ and $T/t = 0.2$. As the temperature is increased, the paring amplitudes become progressively

smaller, and the effect of having a gap also in the down-spin band of $(p_x + ip_y)(|\uparrow,\uparrow\rangle + |\downarrow,\downarrow\rangle)$ is eventually surpassed by the higher magnetization of $(p_x + ip_y)|\uparrow,\uparrow\rangle$.

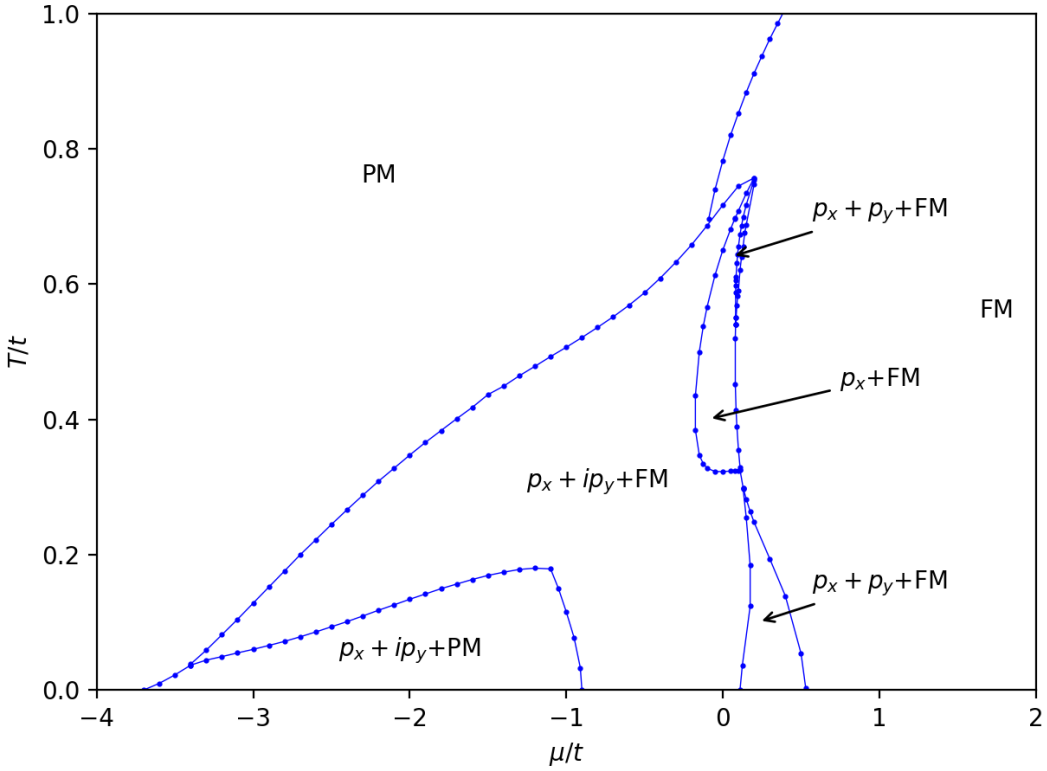

Figure 5.6: μ-T phase diagram for $U/t = 8.5$ and $V/t = -4.0$. For brevity, the phases are named in a slightly different manner. Here $p_x + ip_y$+PM is the phase $(p_x + ip_y)(|\uparrow,\uparrow\rangle + |\downarrow,\downarrow\rangle)$ without FM order. The other superconducting phases having FM order is in the $|\uparrow,\uparrow\rangle$-state.

Figure 5.6 shows a μ-T phase diagram when the Hubbard U-term is included in the Hamiltonian. The entire interval of chemical potentials from minimal to maximal filling degree is $\mu/t = [-4.0, 12.5]$ when $U/t = 8.5$. The choice of limiting the phase diagram up to $\mu/t = 2.0$ is justified by the fact that the non-superconducting phases FM and PM dominate at higher electron densities. In fact, when both superconductivity and magnetism are combined in terms of the Hubbard model, the particle-hole symmetry is broken. This is somewhat unexpected since this symmetry is present when these phenomena are not combined. Examining the impact of the Hubbard U-term, it is clear that it breaks the symmetry when superconductivity is included. Contrary to the exchange field term, which is only affected by the magnetization, the magnitude of the Hubbard U-term depends on the number of electrons per lattice site. More specifically, the free energy of a magnetic phase is lower at $n_e = 2.0 - x$ relative to $n_e = x$, despite the magnetization being the same. This does not break the particle-hole symmetry if the free energy of different magnetic phases are compared, but it does when phases also can be superconducting. This explains why the influence of the magnetic interaction is more prominent at higher electron densities when the Hubbard U-term is included in the Hamiltonian.

The phase diagram in figure 5.6 suggests that the FM and PM states are present, both in the form of superconducting phases and the normal conducting state. Of the superconducting

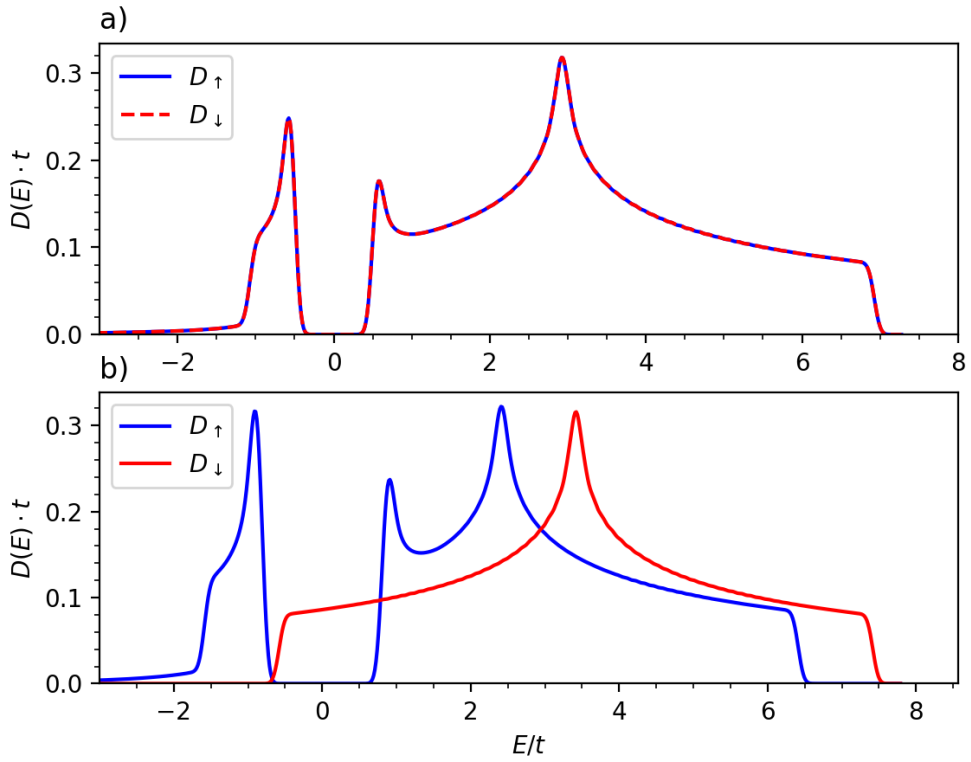

Figure 5.7: DOS of $(p_x + ip_y)(|\uparrow,\uparrow\rangle + |\downarrow,\downarrow\rangle)$ at $T/t = 0.12$ (a), and $(p_x + ip_y)|\uparrow,\uparrow\rangle$ at $T/t = 0.14$ (b). The chemical potential is set to $\mu/t = -2.0$, and the other parameters are the same as in figure 5.6.

phases, the $p_x + ip_y$-state dominates. This is in accordance with the exchange field phase diagram. To discuss which orbital p-wave symmetry is most likely to be present at different chemical potentials, we consider the $\boldsymbol{k}$-space gap function introduced in chapter 4. At very low chemical potentials, the superconducting gaps are negligible for all the momentum symmetries considered in this thesis. Thus, it is reasonable that the normal conducting state is present here in the two phase diagrams. As the filling degree is increased, the gap function of $p_x + ip_y$ is nearly isotropic, while the other p-phases have nodal lines. Since the gap vanishes along these lines, the free energy due to superconductivity is lowest for $p_x + ip_y$. Still, both p_x and $p_x + p_y$ are present for chemical potentials near $\mu/t = 0.0$ in figure 5.6. Considering the region of p_x+FM, the free energy of $(p_x + ip_y)|\uparrow,\uparrow\rangle$ is very close to $p_x|\uparrow,\uparrow\rangle$. For instance, at $\mu/t = 0.0, T/t = 0.4$, the magnetization and the electron density are somewhat higher for p_x than for $p_x + ip_y$+FM, but the difference is large enough to cancel the effect of having a slightly lower superconducting condensation energy in $p_x + ip_y$+FM. For higher temperatures, the difference in free energy relative to $(p_x + p_y)|\uparrow,\uparrow\rangle$ becomes smaller, and it is lowest for $p_x + p_y$+FM in a tiny region between p_x+FM and FM. $(p_x + p_y)|\uparrow,\uparrow\rangle$ is also the most stable phase at low temperature, up to around $\mu/t = 0.5$ for $T/t = 0.0$. Here the presence of $p_x + p_y$ order is caused by a higher FM order than in p_x and $p_x + ip_y$. This makes sense as we are about to enter the region where the magnetic interaction has the greatest influence on the free energy. In this part of the phase diagram, the appearance of FM is not a consequence of the superconductivity becoming insignificant. The reason is that the magnetic Hubbard U-term, which gives highest stability

for the normal conducting state, is here most decisive for the free energy of the system.

There is also a transition from $(p_x + ip_y)(|\uparrow,\uparrow\rangle + |\downarrow,\downarrow\rangle)$ to $(p_x + ip_y)|\uparrow,\uparrow\rangle$ in figure 5.6. As opposed to figure 5.3, the $(p_x + ip_y)(|\uparrow,\uparrow\rangle + |\downarrow,\downarrow\rangle)$-phase has no significant magnetization, so it is in the PM state. What happens here is evident from figure 5.7, which presents the DOS of the most stable phase at both sides of the transition curve. In the PM state of $(p_x + ip_y)(|\uparrow,\uparrow\rangle + |\downarrow,\downarrow\rangle)$ (a), the up- and down-spin bands overlap. This means that energy of the system is not lowered by spin alignment, which is characteristic for the PM state. When the temperature is increased to around $T/t = 0.14$, the self-consistent solution converges to the $p_x + ip_y$-phase with a superconducting gap in the up-spin band, that is the $|\uparrow,\uparrow\rangle$ spin configuration with FM order. Moreover, we observe that the gap in the particular band is about two times larger. The latter is in accordance with the phases having equal free energy at the transition. We also note that when magnetism is included in the model with the possibility of FM order of electrons, the superconducting gap in the up-spin band is more stable than in the down-spin band. As we have seen, the gap in the down-spin band becomes zero at significantly lower temperatures than what is the case for the superconductivity in the up-spin band. At chemical potential $\mu/t = -2.0$, the gap in the up-spin band vanishes first in the transition to PM.

5.4 Concluding remarks

In this chapter, we have analyzed μ-T phase diagrams for FM equal-spin p-wave superconductors in the absence of a magnetic field. We have seen that $p_x + ip_y$ is the dominating orbital symmetry, and that the combined spin-triplet configuration $|\uparrow,\uparrow\rangle + |\downarrow,\downarrow\rangle$ as well as $|\uparrow,\uparrow\rangle$ or $|\downarrow,\downarrow\rangle$ can appear as the most stable. It has become clear that the superconducting spin-triplets $|\uparrow,\uparrow\rangle$ and $|\downarrow,\downarrow\rangle$ have a superconducting gap in only one of the spin bands, while the combined spin configuration has a gap in both. Modeling the FM state by the exchange field, resulted in a shift of the spins of the most stable state about half-filling, which was predicted from the particle-hole transformation of the exchange field term (see equation (3.25)). Interestingly, combining superconductivity and magnetism, the particle-hole symmetry has not been found when magnetism is modeled by the on-site U-term. Our conclusion is that it is due to the U-term increasing in magnitude for higher electron densities and for a fixed magnetization. Examining the phase diagrams, we have found that the FM order is generally greatest in the normal conducting state. The presence of the superconducting states at sufficiently low temperatures is due to the superconducting gaps being large. For increasing temperatures, the gaps become smaller and eventually, it is energetically favourable to have a higher FM order in the non-superconducting state. In this respect, we can understand the phase diagrams in terms of a competition between having a condensate of Cooper pairs in the superconducting state and a higher FM order in the normal conducting state.

Chapter 6

Vortex phase of equal-spin p-wave superconductors with self-consistent vector potential

The objective of this chapter is to give a detailed explanation about how we have tried to obtain self-consistency in the magnetic vector potential for an equal-spin p-wave superconductor. For simplicity, an external magnetic field will be applied to check whether it is possible to obtain a convergent solution, and the magnetic interaction will be set to zero in the testing. In this respect, the spontaneity of the vortex phase arising from the magnetization and the supercurrent in the absence of an external magnetic field, will not be explored in this chapter. We also present the theoretical foundation of the Peierls phase, which is utilized to include a magnetic field in the Hamiltonian. Then the BdG equations in real space are given in addition to the self-consistent equations of the magnetic and superconducting order parameters. We will also show how the supercurrent is calculated in the tight-binding treatment, and how the Maxwell equation can be solved numerically in the finite-difference scheme. When it comes to the formation of vortices, a way to detect them by their complex phase is outlined. Additionally, we will have a look at how different gauges can result in distinct vortex configurations, pointing to the importance of initial conditions chosen for the order parameter. The chapter ends by some concluding remarks.

6.1 Peierls phase

The derivation of the Peierls phase given here, follows the main steps in the book of Zhu [70], which refers to the original article of Luttinger (1951) [71]. Considering electrons affected by a periodic potential $u(\boldsymbol{r})$ due to the positive ion lattice, and a magnetic vector potential $\boldsymbol{A}$, the first quantized Hamiltonian in the grand canonical ensemble is

$$\hat{H} = \frac{\left(\hat{\boldsymbol{p}} + e\boldsymbol{A}(\boldsymbol{r})\right)^2}{2m} + u(\boldsymbol{r}) - \mu, \tag{6.1}$$

where e is the charge of an electron. The vector potential is related to the magnetic field by

$$\boldsymbol{B} = \nabla \times \boldsymbol{A}. \tag{6.2}$$

To go to second quantization, we again use a linear combination of atomic orbitals (LCAO). In addition, complex phases Λ_i are added to the atomic orbitals, that is

$$|i\rangle = \phi(\boldsymbol{r} - \boldsymbol{r}_i) \to \phi(\boldsymbol{r} - \boldsymbol{r}_i)e^{-ie\Lambda_i}, \tag{6.3}$$

where

$$\Lambda_i = \int_{\boldsymbol{r}_i}^{\boldsymbol{r}} \boldsymbol{A}(\boldsymbol{l})d\boldsymbol{l} = \int_0^1 (\boldsymbol{r} - \boldsymbol{r}_i) \cdot \boldsymbol{A}\big(\boldsymbol{r}_i + \lambda(\boldsymbol{r} - \boldsymbol{r}_i)\big)d\lambda. \tag{6.4}$$

In equation (6.4), the path integral is along the straight line connecting the points $\boldsymbol{r}_i$ and $\boldsymbol{r}$, parameterized as $\boldsymbol{l} = \boldsymbol{r}_i + \lambda(\boldsymbol{r} - \boldsymbol{r}_i)$. The next step in second quantization is to compute $H_{i,j} = \langle i|\hat{H}|j\rangle$. Acting with $\hat{\boldsymbol{p}}$ in the first term of equation (6.1) on an atomic orbital (equation (6.3)), gives $\nabla\Lambda_i$ from the exponential. It can be shown that with Λ_i given by equation (6.4), we have

$$\nabla\Lambda_i = \boldsymbol{A}(\boldsymbol{r}) + \int_0^1 \lambda(\boldsymbol{r} - \boldsymbol{r}_i) \times \boldsymbol{B}\big(\boldsymbol{r}_i + \lambda(\boldsymbol{r} - \boldsymbol{r}_i)\big)d\lambda. \tag{6.5}$$

Moreover, acting with the first term of $\hat{H}$ on an atomic orbital, leads to

$$\begin{aligned}\big(\hat{\boldsymbol{p}} + e\boldsymbol{A}(\boldsymbol{r})\big)^2\phi(\boldsymbol{r} - \boldsymbol{r}_i)e^{-ie\Lambda_i} &= e^{-ie\Lambda_i}\big[\hat{\boldsymbol{p}} - e\nabla\Lambda_i + e\boldsymbol{A}(\boldsymbol{r})\big]^2 \\ &= e^{-ie\Lambda_i}\big[\hat{\boldsymbol{p}} - e\int_0^1 \lambda(\boldsymbol{r} - \boldsymbol{r}_i) \times \boldsymbol{B}\big(\boldsymbol{r}_i + \lambda(\boldsymbol{r} - \boldsymbol{r}_i)\big)d\lambda\big]^2.\end{aligned} \tag{6.6}$$

Hence, the second-quantized Hamiltonian is

$$\hat{H} = \sum_{i,j,\sigma} H_{i,j}\hat{c}^\dagger_{i,\sigma}\hat{c}_{j,\sigma}, \tag{6.7}$$

where

$$\begin{aligned}H_{i,j} = \int \phi^*(\boldsymbol{r} - \boldsymbol{r}_i)e^{ie(\Lambda_i - \Lambda_j)}\Bigg[\frac{1}{2m}\Big(\hat{\boldsymbol{p}} - e\int_0^1 \lambda(\boldsymbol{r} - \boldsymbol{r}_i) \times \boldsymbol{B}\big(\boldsymbol{r}_i + \lambda(\boldsymbol{r} - \boldsymbol{r}_i)\big)d\lambda\Big)^2 \\ + u(\boldsymbol{r}) - \mu\Bigg]\phi(\boldsymbol{r} - \boldsymbol{r}_j)d\boldsymbol{r}.\end{aligned} \tag{6.8}$$

Assuming that the vector potential does not vary significantly, we can neglect the λ-integral as $\boldsymbol{r} \approx \boldsymbol{r}_i$, since the orbitals are localized. Thus, $H_{i,j} = -t_{i,j}e^{i\phi_{i,j}} - \mu$, and the usual hopping term has now acquired a complex phase $\phi_{i,j}$, the so-called Peierls phase, which is given by

$$\begin{aligned}\phi_{i,j} &= -\frac{e}{\hbar}\int_{\boldsymbol{r}_j}^{\boldsymbol{r}_i} \boldsymbol{A}(\boldsymbol{r}) \cdot d\boldsymbol{r} \\ &= -\frac{\pi}{\Phi_0}\int_{\boldsymbol{r}_j}^{\boldsymbol{r}_i} \boldsymbol{A}(\boldsymbol{r}) \cdot d\boldsymbol{r}.\end{aligned} \tag{6.9}$$

Here $\hbar$, which was set equal to 1 in the derivation, is included to write the prefactor in terms of the superconducting flux quanta $\Phi_0 = h/2e$.

6.2 BdG equations and self-consistent order parameters

Adding the Peierls phase $\phi_{i,j}$ to the hopping term in the Hamiltonian of equation (5.1), a magnetic field can be included in the system. Analogous to the previous chapter, the mean-field approximation is given by

$$\begin{aligned}\hat{H} = &-t\sum_{\langle i,j\rangle,\sigma} e^{i\phi_{i,j}}\hat{c}^\dagger_{i,\sigma}\hat{c}_{j,\sigma} - \mu\sum_{i,\sigma}\hat{n}_{i,\sigma} + \frac{1}{2}V\sum_{\langle i,j\rangle,\sigma}\left[F^{\sigma\sigma}_{i,j}\hat{c}^\dagger_{j,\sigma}\hat{c}^\dagger_{i,\sigma} + \text{h.c.}\right] \\ &- h\sum_i(\hat{n}_{i,\uparrow} - \hat{n}_{i,\downarrow}) + U\sum_{i,\sigma}\langle n_{i,\bar{\sigma}}\rangle\hat{n}_{i,\sigma},\end{aligned} \tag{6.10}$$

where $\phi_{i,j}$ is defined by equation (6.9), in which $\boldsymbol{r}_i$ and $\boldsymbol{r}_j$ are the position vectors for the lattice sites i and j, respectively. The inclusion of the Peierls phase breaks the translational symmetry of the system in the x- and y-direction as the vector potential $\boldsymbol{A}(\boldsymbol{r})$ is position dependent. In addition, the average number operator is now site dependent as the system is inhomogeneous. Therefore, we will not consider a $\boldsymbol{k}$-space transformation of the Hamiltonian. Defining the spinor

$$\hat{\boldsymbol{D}}_{i,\sigma} = \begin{pmatrix}\hat{c}_{i,\sigma}\\ \hat{c}^\dagger_{i,\sigma}\end{pmatrix}, \tag{6.11}$$

equation (6.10) can be written on matrix form as

$$\hat{H} = \frac{1}{2}\sum_{\langle i,j\rangle,\sigma}\hat{\boldsymbol{D}}^\dagger_{i,\sigma}\boldsymbol{H}_{i,j,\sigma}\hat{\boldsymbol{D}}_{j,\sigma}, \tag{6.12}$$

where

$$\boldsymbol{H}_{i,j,\sigma} = \begin{pmatrix}-te^{i\phi_{i,j}} - (\mu + \sigma h - U\langle n_{\bar{\sigma}}\rangle)\delta_{i,j} & -VF^{\sigma,\sigma}_{i,j}\\ VF^{\sigma,\sigma *}_{i,j} & te^{-i\phi_{i,j}} + (\mu + \sigma h - U\langle n_{\bar{\sigma}}\rangle)\delta_{i,j}\end{pmatrix}. \tag{6.13}$$

Because of the site dependence, it is worth to emphasize that the site index i has two components, that is $i = (i_x, i_y)$. As used so far in this thesis, $i + \hat{\boldsymbol{x}}$ means the nearest-neighbour of i in the positive x-direction. In the corresponding eigenvalue problem, the index j is over all the N sites of the lattice when i is fixed. Since $\boldsymbol{H}_{i,j,\sigma}$ is a 2×2 sub-matrix, we then have to diagonalize a $2N \times 2N$ matrix for each of the two spin directions. The Bogoliubov transformations used in this respect are defined by

$$\hat{c}_{i,\sigma} = \sum_n u_{n,i,\sigma}\hat{\alpha}_{n,\sigma} \tag{6.14}$$

$$\hat{c}^\dagger_{i,\sigma} = \sum_n v_{n,i,\sigma}\hat{\alpha}_{n,\sigma}, \tag{6.15}$$

where $n = 1, 2, ..., 2N$. For each spin, the solution of the eigenvalue problem consists of $2N$ eigenvalues $E_{n,\sigma}$ and $2N$ eigenvectors on the form

$$\boldsymbol{A}_{n,\sigma} = \begin{pmatrix}\boldsymbol{a}_{n,1,\sigma}\\ \boldsymbol{a}_{n,2,\sigma}\\ \vdots\\ \boldsymbol{a}_{n,N,\sigma}\end{pmatrix}, \quad \boldsymbol{a}_{n,i,\sigma} = \begin{pmatrix}u_{n,i,\sigma}\\ v_{n,i,\sigma}\end{pmatrix}. \tag{6.16}$$

According to the operator basis defined by equations (6.14) and (6.15), the paring amplitudes are given by

$$F^{x(y)\pm}_{i,\sigma,\sigma} = \sum_n u_{n,i,\sigma} v^*_{n,i\pm\hat{\boldsymbol{x}}(\hat{\boldsymbol{y}}),\sigma}\big(1 - f(E_{n,\sigma})\big). \tag{6.17}$$

Due to the site dependence of the paring amplitudes, the simplification shown in equation (4.15) is not valid any longer. Hence, the general equal-spin p-wave superconducting correlations on the form

$$F^{\sigma,\sigma}_{i,p_{x(y)}} = \frac{F^{x(y)+}_{i,\sigma,\sigma} - F^{x(y)-}_{i,\sigma,\sigma}}{2}, \tag{6.18}$$

will be considered. The number densities are determined self-consistently from the expression

$$\langle n_{i,\sigma}\rangle = \sum_n |u_{n,i,\sigma}|^2 f(E_{n,\sigma}). \tag{6.19}$$

Furthermore, the average magnetization of the system is obtained by summing over the local magnetization M_i at each site and dividing by the total number of sites, that is

$$M = \frac{1}{N}\sum_i M_i = \frac{1}{N}\sum_i \big(\langle n_{i,\uparrow}\rangle - \langle n_{i,\downarrow}\rangle\big). \tag{6.20}$$

In the rest of this chapter, the magnetic interaction strengths U and h are set to zero, and there will be no magnetization in the system. The magnetic field due to ferromagnetic order will be considered in the next chapter, where the global finite-size system magnetization M in equation (6.20) is used.

6.3 Peierls phase on a square lattice

In order to compute the Peierls phase of the hopping term, we consider the lattice drawn in figure 6.1, and discussed by Aidelsburger [72]. On a square lattice, it is convenient to distinguish between the phases

$$\phi^{x(y)}_{m_x,m_y} = -\frac{\pi}{\Phi_0}\int_{m_{x(y)}}^{m_{x(y)}+1} \boldsymbol{A}(\boldsymbol{r})\cdot d\boldsymbol{r} = -\frac{\pi}{\Phi_0}\int_{m_{x(y)}}^{m_{x(y)}+1} A_{x(y)}(\boldsymbol{r})dx(y). \tag{6.21}$$

Here (m_x, m_y) denotes the indices of a given site, and $\phi^x_{m_x,m_y}$ and $\phi^y_{m_x,m_y}$ are the Peierls phases picked up by an electron tunneling to sites (m_x+1, m_y) and (m_x, m_y+1), respectively. With respect to equation (6.9), we have $i = (m_x+1, m_y)$ and $j = (m_x, m_y)$ in the x-case of equation (6.21), and $i = (m_x, m_y+1)$ and $j = (m_x, m_y)$ in the y-case. In addition, the total phase acquired by an electron in the closed counterclockwise path in figure 6.1, can be related to the magnetic flux Φ_{m_x,m_y} through unit cell (m_x, m_y) as

$$\begin{aligned}\phi^x_{m_x,m_y} + \phi^y_{m_x+1,m_y} - \phi^x_{m_x,m_y+1} - \phi^y_{m_x,m_y} &= -\frac{\pi}{\Phi_0}\oint \boldsymbol{A}(\boldsymbol{r})\cdot d\boldsymbol{r} = -\frac{\pi}{\Phi_0}\iint \boldsymbol{B}\cdot d\boldsymbol{S} \\ &= -\pi\frac{\Phi_{m_x,m_y}}{\Phi_0}.\end{aligned} \tag{6.22}$$

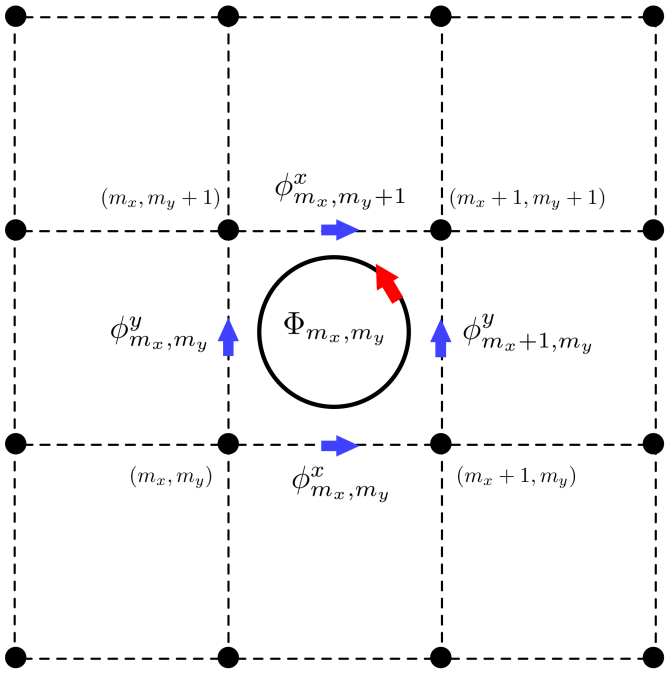

Figure 6.1: Peierls phase of electrons on a square lattice. In the presence of a magnetic field, $\phi^x_{m_x,m_y}$ is the phase acquired by an electron tunneling from site (m_x, m_y) to (m_x+1, m_y), that is an electron creation at (m_x+1, m_y) and annihilation at (m_x, m_y). The blue arrows indicate the direction of the path integral of the respective Peierls phase. An electron tunneling in the opposite direction, gets a phase with opposite sign. Φ_{m_x,m_y} is the magnetic flux through unit cell (m_x, m_y), and it is related to the total phase of an electron moving along the boundaries of the cell in the direction of the red arrow. The figure is analogous to figure in the reference [72].

In the case of a homogeneous magnetic field, the flux through each of the unit cells will be the same, that is $\Phi_{m_x,m_y} = \Phi$. Denoting the total magnetic flux through the system as Φ_{tot} and using open boundary conditions, the flux through a cell is

$$\Phi = \frac{\Phi_{\text{tot}}}{(L_x - 1)(L_y - 1)}, \tag{6.23}$$

where L_x and L_y are the number of lattice sites in the x- and y-direction. Having open boundary conditions, there are in total $(L_x - 1)(L_y - 1)$ unit cells.

6.4 The vortex phase

In the theory of superconductors, it is usual to distinguish between two general classes of superconductors, that is superconductors of type I and type II. The classification is based on how the superconductors behave in an increasing external magnetic field [60, 73]. According to the Meissner effect, the field is expelled from the interior of a superconductor as long as the field is not too strong. If the field exceeds a critical value for the particular superconductor, the

induced supercurrent, which sets up a magnetic field counteracting the external field, can not increase further without destroying the superconducting state. For a type I superconductor, there will be a phase transition to the normal conducting phase. On the other hand, a type-II superconductor enters the vortex phase with partial penetration of magnetic field lines, corresponding to one superconducting flux quanta Φ_0 through each vortex core. Eventually, with increasing field strength, the density of vortices will become so high that the vortex phase breaks down, transitioning to the normal state.

In order to make a more quantitative distinction between superconductors of type I and II, two characteristic length scales can be compared, the superconducting coherence length ξ and the penetration depth λ. The coherence length is a parameter of the Ginzburg-Landau (GL) theory of superconductivity, and it gives a measure for the length over which the superconducting order parameter varies [74]. The penetration depth determines how fast the magnetic field decays moving into the superconducting region, and it is included in the London equation [73]. In fact, the ratio $\kappa = \lambda/\xi$, the so-called GL parameter, determines if the superconductor is of type I or II. The critical value of κ in the GL theory is $1/\sqrt{2}$, and it is found to be higher for type II superconductors than for superconductors of type I [75]. In the conventional BCS theory, the coherence length is given as [76]

$$\xi_{\mathrm{BCS}} = \frac{v_{\mathrm{F}}}{\pi|\Delta|}. \tag{6.24}$$

In this equation, $\hbar$ in the numerator is set to 1, and v_{F} is the Fermi velocity. Accordingly, the coherence length decreases with increasing magnitude of the electron-electron attraction strength V. Defining the width of the vortex as $2\xi_{\mathrm{BCS}}$, broader vortices are expected for smaller $|V|$.

6.5 Self-consistent vector potential

The magnetic field produced by the supercurrent can be accounted for by the integration of the Maxwell equation in the self-consistent procedure. In this chapter, the external magnetic field $\boldsymbol{B}_{\mathrm{ext}}$ is uniform, pointing in the positive z-direction. With $\boldsymbol{B}_{\mathrm{ext}} = B_{\mathrm{ext}}\hat{\boldsymbol{z}}$, a possible gauge is

$$\boldsymbol{A}_{\mathrm{ext}}(\boldsymbol{r}) = B_{\mathrm{ext}}(-y, 0), \tag{6.25}$$

since $\boldsymbol{A}$ and $\boldsymbol{B}$ are related by equation (6.2). If we only consider the external field, the x- and y-component of the Peierls phase are

$$\phi^x_{m_x,m_y} = \frac{\pi}{\Phi_0} B_{\mathrm{ext}} m_y \tag{6.26}$$

$$\phi^y_{m_x,m_y} = 0. \tag{6.27}$$

Generally, the vector potential varies among sites in the lattice, and the Peierls phase in the x- and y-direction will therefore be computed as

$$\phi^x_{m_x,m_y} = -\frac{\pi}{2\Phi_0}\big[A_x(m_x, m_y) + A_x(m_x+1, m_y)\big] \tag{6.28}$$

$$\phi^y_{m_x,m_y} = -\frac{\pi}{2\Phi_0}\big[A_y(m_x, m_y) + A_y(m_x, m_y+1)\big]. \tag{6.29}$$

The magnetic field is related to the supercurrent density by the Maxwell equation known as the Ampere's law. On differential form, it is given by

$$\nabla \times \boldsymbol{B} = \boldsymbol{J}, \tag{6.30}$$

where $\boldsymbol{J}$ is here the supercurrent density, and the permeability μ_0 is 1 in the chosen system of units. The gauge freedom of $\boldsymbol{A}$ can now be used to set $\nabla \cdot \boldsymbol{A} = 0$, which is referred to as the Coulomb gauge. In this gauge, equation (6.30) can in terms of $\boldsymbol{A}$ be written as

$$\nabla^2 \boldsymbol{A} = -\boldsymbol{J}, \tag{6.31}$$

which is referred to as the Poisson equation of $\boldsymbol{A}$.

6.5.1 Finite-difference method (FDM)

Equation (6.31) will be solved numerically with the finite-difference method (FDM). In this method, the Laplace operator $\nabla^2 = \partial_x^2 + \partial_y^2$ can be discretized by second-order central differences, defined as [77]

$$\partial_x^2 f(x,y) = \frac{f(x+\Delta x, y) - 2f(x,y) + f(x-\Delta x, y)}{\Delta x^2} + \mathcal{O}(\Delta x^2) \tag{6.32}$$

$$\partial_y^2 f(x,y) = \frac{f(x, y+\Delta y) - 2f(x,y) + f(x, y-\Delta y)}{\Delta y^2} + \mathcal{O}(\Delta y^2), \tag{6.33}$$

where Δx and Δy denote the lattice spacings, which are set to 1 in our model. If the Laplace operator act on the x-component of the vector potential, the finite-difference representation is

$$\begin{aligned}\nabla^2 A_x(m_x, m_y) \approx & A_x(m_x+1, m_y) + A_x(m_x-1, m_y) + A_x(m_x, m_y+1) \\ & + A_x(m_x, m_y-1) - 4A_x(m_x, m_y).\end{aligned} \tag{6.34}$$

The Poisson equation of A_x is therefore

$$\begin{aligned}J_x(m_x, m_y) = & 4A_x(m_x, m_y) - A_x(m_x+1, m_y) - A_x(m_x-1, m_y) \\ & - A_x(m_x, m_y+1) - A_x(m_x, m_y-1).\end{aligned} \tag{6.35}$$

With the x-component of the supercurrent known, $A_x(m_x, m_y)$ can be determined by solving the coupled set of equations, that is the matrix equation $\boldsymbol{W}\boldsymbol{x} = \boldsymbol{b}$. The matrix $\boldsymbol{W}$ is given by

$$\boldsymbol{W} = \begin{pmatrix} \boldsymbol{D} & -\mathbb{1} & 0 & \cdots & 0 \\ -\mathbb{1} & \boldsymbol{D} & -\mathbb{1} & \cdots & 0 \\ \vdots & \ddots & \ddots & \ddots & \vdots \\ 0 & \cdots & -\mathbb{1} & \boldsymbol{D} & -\mathbb{1} \\ 0 & \cdots & 0 & -\mathbb{1} & \boldsymbol{D} \end{pmatrix}, \tag{6.36}$$

in which $\mathbb{1}$ is the identity matrix, and the matrix $\boldsymbol{D}$ is

$$\boldsymbol{D} = \begin{pmatrix} 4 & -1 & 0 & \cdots & 0 \\ -1 & 4 & -1 & \cdots & 0 \\ \vdots & \ddots & \ddots & \ddots & \vdots \\ 0 & \cdots & -1 & 4 & -1 \\ 0 & \cdots & 0 & -1 & 4 \end{pmatrix}. \tag{6.37}$$

Fixing the components of the vector potential $\boldsymbol{A}$ on the boundary of the lattice, $\boldsymbol{W}$ is a matrix of size $(L_x-2)(L_y-2)\times(L_x-2)(L_y-2)$ when there are $N=L_xL_y$ lattice sites in total. Here D and $\mathbb{1}$ have $(L_x-2)\times(L_x-2)$ entries. The column vectors $\boldsymbol{x}$ and $\boldsymbol{b}$ are given by

$$\boldsymbol{x}=\begin{pmatrix} A_x(2,2)\\ A_x(3,2)\\ \vdots\\ A_x(L_x-1,2)\\ \vdots\\ A_x(L_x-1,L_y-1)\end{pmatrix}, \tag{6.38}$$

and

$$\boldsymbol{b}=\begin{pmatrix} J_x(2,2)+A_x(2,1)+A_x(1,2)\\ J_x(3,2)+A_x(3,1)\\ \vdots\\ J_x(L_x-1,2)+A_x(L_x-1,1)+A_x(L_x,2)\\ \vdots\\ J_x(L_x-1,L_y-1)+A_x(L_x-1,L_y)+A_x(L_x,L_y-1)\end{pmatrix}. \tag{6.39}$$

Similarly, the Poisson equation of A_y can be solved.

6.5.2 Supercurrents in the tight-binding model

In the self-consistent algorithm of the vector potential, there is a need for an expression relating the supercurrent to the solution of the eigenvalue problem. A way to express the supercurrent in terms of eigenvalues and eigenvectors will be explained in the following [78].

The continuity equation at site i is

$$\frac{\partial\hat{\rho}_i}{\partial t}=-\nabla\cdot\hat{\boldsymbol{J}}_i, \tag{6.40}$$

where $\hat{\rho}_i$ is the positive charge density operator, and $\hat{\boldsymbol{J}}_i$ is the supercurrent density operator at site i. The positive charge density is considered because of the electric current direction being the direction of movement for positive charges. Integrating over the 2D volume Ω centered at site i and with faces at $i\pm\hat{\boldsymbol{x}}/2, i\pm\hat{\boldsymbol{y}}/2$, we obtain

$$\frac{\partial\hat{Q}_i}{\partial t}=-\hat{I}_i. \tag{6.41}$$

This follows from the Gauss divergence theorem where

$$\int_\Omega\nabla\cdot\hat{\boldsymbol{J}}_i d\Omega=\int_{\partial\Omega}\hat{\boldsymbol{J}}_i\cdot d\boldsymbol{S}=\hat{I}_i. \tag{6.42}$$

$\hat{I}_i$ is the operator for the net supercurrent at site i out of Ω, and $Q_i=e\hat{n}_i$. The quantum mechanical time derivative of $\hat{n}_i$ is

$$\begin{aligned}\frac{\partial\hat{n}_i}{\partial t}&=i[\hat{H},\hat{n}_i]\\ &=it\sum_{j,\sigma}\left(e^{i\phi_{i,j}}\hat{c}^\dagger_{i,\sigma}\hat{c}_{j,\sigma}-\text{h.c.}\right).\end{aligned} \tag{6.43}$$

The derivation can be found in appendix A.2. Here $\hat{H}$ is not the mean-field approximated Hamiltonian as it should conserve the particle number. Taking the average, the time derivative is (see appendix A.3)

$$\left\langle \frac{\partial n_i}{\partial t} \right\rangle = it \sum_{n,j,\sigma} \left(e^{i\phi_{i,j}} u^*_{n,i,\sigma} u_{n,j,\sigma} - \text{h.c.} \right) f(E_{n,\sigma}), \tag{6.44}$$

and equation (6.41) gives

$$\langle I_i \rangle = -e \left\langle \frac{\partial \hat{n}_i}{\partial t} \right\rangle. \tag{6.45}$$

As the Maxwell equation is given in terms of the supercurrent density, we define the supercurrent densities in the x- and y-direction at site i as

$$\langle J_i^x \rangle = \langle J_i^{x+} \rangle - \langle J_i^{x-} \rangle \tag{6.46}$$

$$\langle J_i^y \rangle = \langle J_i^{y+} \rangle - \langle J_i^{y-} \rangle. \tag{6.47}$$

In equation (6.46), $\langle J_i^{x+} \rangle$ is the net current density out of the face at $i + \hat{\boldsymbol{x}}/2$, and $\langle J_i^{x-} \rangle$ is out of the face at $i - \hat{\boldsymbol{x}}/2$. Since the lattice spacing is equal to unity, there is no difference between the supercurrent and the supercurrent density in this model. Therefore, we have

$$\langle J_i^{x\pm} \rangle = -iet \sum_{n,\sigma} \left(e^{i\phi_{i,i\pm\hat{\boldsymbol{x}}}} u^*_{n,i,\sigma} u_{n,i\pm\hat{\boldsymbol{x}},\sigma} - \text{h.c.} \right) f(E_{n,\sigma}), \tag{6.48}$$

and analogously for the y-direction.

6.5.3 Self-consistent procedure

The self-consistent algorithm of the vector potential starts by the initialization of $\boldsymbol{A} = (A_x, A_y)$ on each site of the lattice. In the testing, we have generally used the initial condition of having no supercurrent or magnetization in the system, that is $\boldsymbol{A} = \boldsymbol{A}_{\text{ext}}$. In each iteration, $\boldsymbol{A}$ is updated. The computed vector potential from the preceding iteration enters the Hamiltonian through the Peierls phase. Diagonalization of the Hamiltonian up- and down-spin matrices gives us new eigenvalues and eigenvectors. Using the method described in the previous subsection, the tight-binding supercurrent is calculated from the eigenvalues, eigenvectors and the Peierls phase. The next step is to solve the Maxwell equation with respect to $\boldsymbol{A}$ by the finite-difference method. In this way, the vector potential and new values of the Peierls phase are determined on all non-boundary sites. This procedure is repeated until the relative difference in $\boldsymbol{A}$ on all sites of lattice between an iteration and the next, is below a tolerance.

6.6 Gauge invariance of the theory

In this section the gauge invariance of the theory will be discussed. Because of $\boldsymbol{B}$ being the physical observable quantity and not $\boldsymbol{A}$, we are free to choose the vector potential as long as equation (6.2) is fulfilled. According to this equation, the non-uniqness of $\boldsymbol{A}$ can be expressed as

$$\boldsymbol{A} \to \boldsymbol{A} + \nabla\lambda, \tag{6.49}$$

since $\nabla \times \nabla\lambda = 0$, irrespective of what λ is. Under a gauge transformation, the creation and annihilation operators are also transformed. The transformation is given by [79]

$$\hat{c}_{i,\sigma} \to e^{-ie\lambda(\boldsymbol{r}_i)}\hat{c}_{i,\sigma}. \tag{6.50}$$

We can now check whether the Hamiltonian in equation (6.10) is gauge-invariant. Since the Peierls phase transforms as

$$\phi_{i,j} \to -\frac{\pi}{\Phi_0}\int_{\boldsymbol{r}_j}^{\boldsymbol{r}_i}\big[\boldsymbol{A}(\boldsymbol{r}) + \nabla\lambda(\boldsymbol{r})\big]\cdot d\boldsymbol{r} \tag{6.51}$$

$$= \phi_{i,j} + \frac{\pi}{\Phi_0}\big[\lambda(\boldsymbol{r}_j) - \lambda(\boldsymbol{r}_i)\big], \tag{6.52}$$

and $\pi/\Phi_0 = e$, the hopping term is gauge-invariant. The extra term in the Peierls phase is canceled by the exponential factors acquired by the creation and annihilation operators. Moving on to the superconducting interaction term, the phase of the product of two creation or two annihilation operators is canceled by the respective paring amplitudes. Therefore, also this term of the Hamiltonian is gauge-invariant. Finally, it is trivial to see that the on-site U- and μ-term are invariant under a gauge transformation. The supercurrent is an observable quantity. Thus, it should also be independent of what gauge is used. Regarding equations (6.14) and (6.15), the coherence factors transform as

$$u_{n,i,\sigma} = e^{-ie\lambda(\boldsymbol{r}_i)}u_{n,i,\sigma} \tag{6.53}$$

$$v_{n,i,\sigma} = e^{ie\lambda(\boldsymbol{r}_i)}v_{n,i,\sigma}. \tag{6.54}$$

Combined with the transformation property of the Peierls phase in equation (6.51), $\langle J_i^{x\pm}\rangle$ in equation (6.48) respects the gauge invariance. This is also the case for $\langle J_i^{y\pm}\rangle$, so that $\langle J_i^x\rangle$ and $\langle J_i^y\rangle$ obey this symmetry.

In total, the theory is therefore gauge-invariant. However, depending on the choice of gauge, the self-consistent solution can converge to different metastable states when superconductivity is included in the model. The gauge invariance of the theory is respected if we for two different gauges, choose the initial conditions of the superconducting order parameters in an appropriate manner. This observation has also been pointed out by Uranga [80]. To give an explanation of how this can be done, let us consider a opposite-spin s-wave superconductor without self-consistent vector potential for simplicity. The explanation for equal-spin p-wave will be analogous. The superconducting interaction term for conventional s-wave is

$$\hat{H}_V^s = \sum_i[\Delta_i\hat{c}_{i,\downarrow}^\dagger\hat{c}_{i,\uparrow}^\dagger + \text{h.c.}], \tag{6.55}$$

where

$$\Delta_i = V_s\langle c_{i,\uparrow}c_{i,\downarrow}\rangle. \tag{6.56}$$

Figures 6.2 and 6.3 show the absolute value of the order parameter. The former has gauge $\boldsymbol{A} = B(-y, 0)$ and the latter is for $\boldsymbol{A} = 1/2B(-y, x)$. Additionally, the respective supercurrents are plotted in figure 6.4. The figures clearly give distinct vortex configurations in these gauges. In fact, the number of isolated vortices are 5 and 4, respectively. The explanation for this is a bit subtle. In accordance with equation (6.49), two different gauges $\boldsymbol{A}_1$ and $\boldsymbol{A}_2$ are related by

$$\boldsymbol{A}_1 = \boldsymbol{A}_2 + \nabla\lambda, \tag{6.57}$$

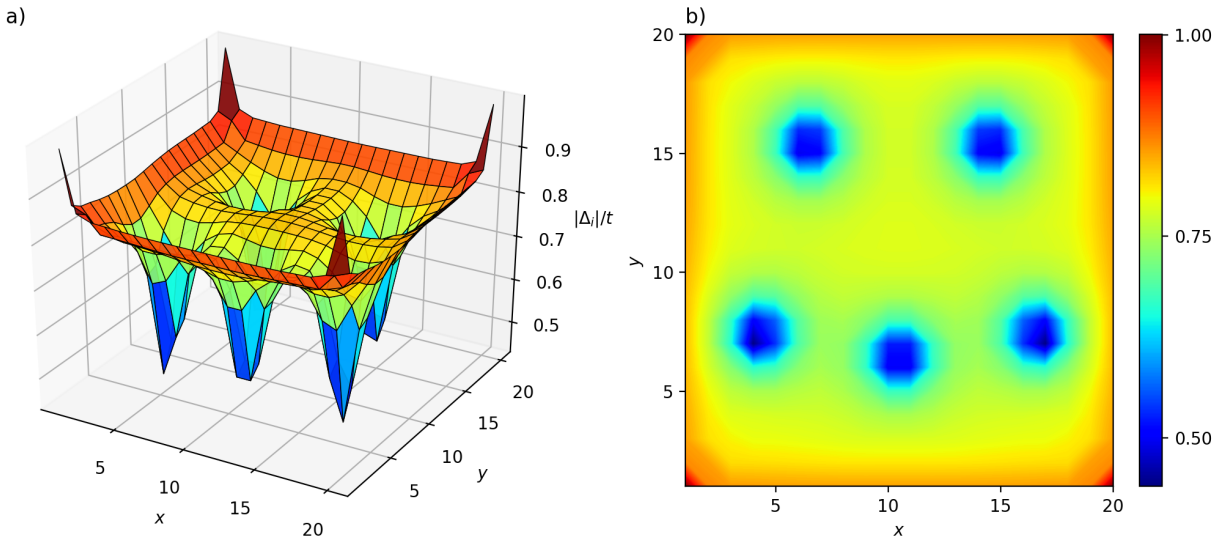

Figure 6.2: Surface plot (a) and colormap (b) of $|\Delta_i|$ for the conventional s-wave superconductor for the gauge $\boldsymbol{A} = B(-y, 0)$. Input parameters are $V_s/t = -3.0$, $T/t = 0.25$, $\mu/t = 0.0$ and $\Phi_{\text{tot}} = 6\Phi_0$.

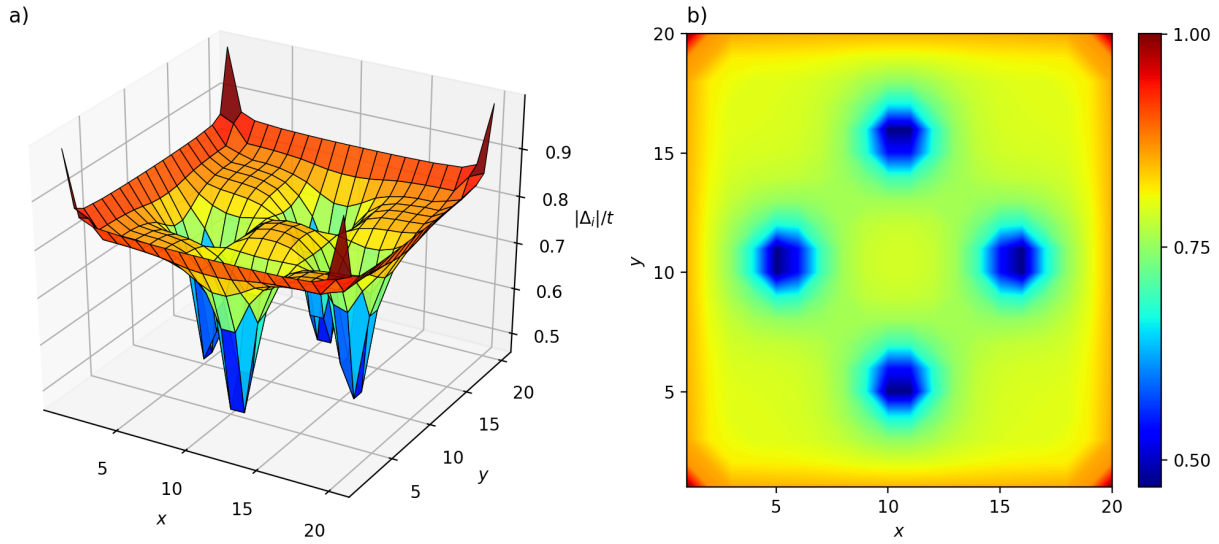

Figure 6.3: Similar plots as in figure 6.2, but for the gauge $\boldsymbol{A} = 1/2B(-y, x)$.

for a suitable choice of λ. The point is now that unless the order parameters in the two cases are related by

$$\Delta_i^1 = e^{-i2e\lambda(\boldsymbol{r}_i)}\Delta_i^2, \tag{6.58}$$

the self-consistent solution will be different. For instance, if we consider gauges $\boldsymbol{A}_1 = B(-y, 0)$ and $\boldsymbol{A}_2 = 1/2B(-y, x)$, $\lambda(\boldsymbol{r})$ can be set to

$$\lambda(\boldsymbol{r}) = \frac{1}{2}Bxy. \tag{6.59}$$

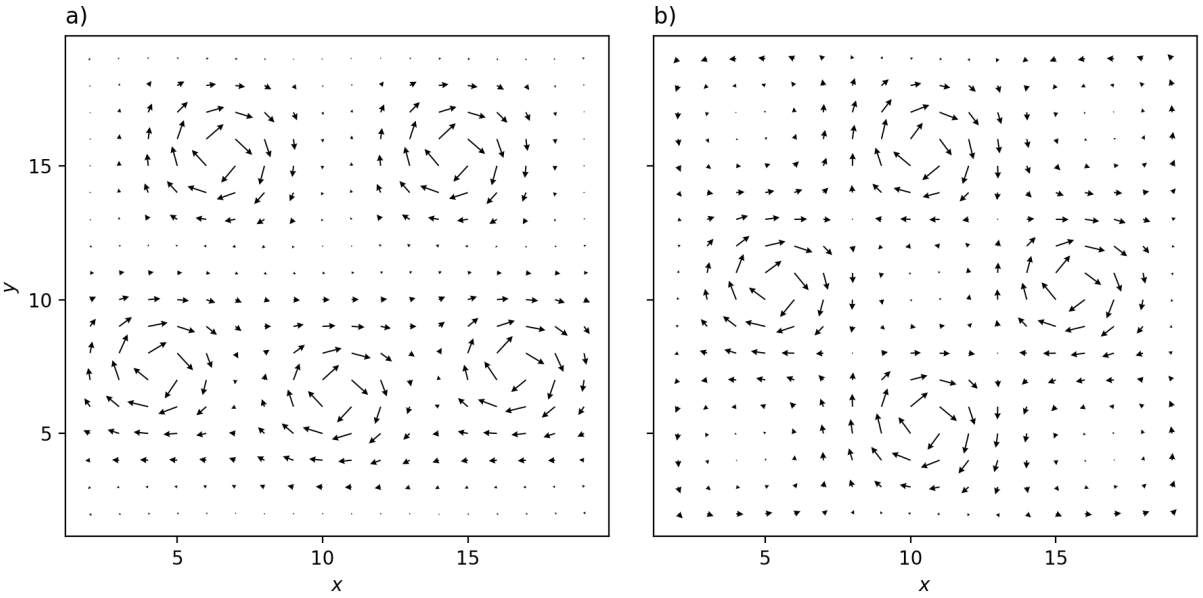

Figure 6.4: The associated supercurrents of figure 6.2 (a) and figure 6.3 (b). The vectors are in units of $t\Phi_0$.

The self-consistent solution respects the gauge invariance of the theory if the initial conditions of Δ_i^1 and Δ_i^2 are in accordance with equation (6.58). For equal-spin p-wave superconductivity, this is the case when the start values of the nearest-neighbour paring amplitudes are related by

$$\left(F_{i,j}^{\sigma,\sigma}\right)^1 = e^{-ie[\lambda(\boldsymbol{r}_i)+\lambda(\boldsymbol{r}_j)]}\left(F_{i,j}^{\sigma,\sigma}\right)^2, \tag{6.60}$$

in the two gauges of equation (6.57). We also note that in the presence of a magnetic field, it is common to define the superconducting correlations in a gauge-invariant way. This means that the nearest-neighbour paring amplitudes should be defined as [81]

$$F_{i,j}^{\sigma,\sigma} = e^{i\phi_{i,j}}\langle c_{i,\sigma}c_{j,\sigma}\rangle. \tag{6.61}$$

The fact that different initial conditions of the superconducting order parameters, or equivalently different gauges for a fixed set of initial conditions, can result in distinct metastable vortex configurations, should be taken into account in the comparison of free energies. For instance, using the same gauge and the physical parameters as in figure 6.2, only varying the start values of Δ_i, another convergent solution consists of 6 vortices. Given that the free energy of a superconducting phase depends on the magnitude of the order parameter, distinct vortex configurations do not have the same free energy in general. In principle, we should therefore apply a vast number of gauges to compare the free energy of different metastable states corresponding to a particular phase and the same physical parameters.

6.7 Phase of the superconducting order parameter

The figures presented in the last section, indicate the presence of vortices. The plots of $|\Delta_i|$ show there are regions where the order parameter becomes considerable smaller in magnitude

than in the superconducting bulk. If the system size (L_x, L_y) is increased further, the minima become even smaller. In fact, superconducting electron-electron correlations are expected to vanish sufficiently close to the vortex centers. In figure 6.4, we observe that the supercurrent is circulating in the proximity of the vortex cores, and it becomes more prominent as we move to the centers. This means that the induced magnetic field, which counteract the external field, are greatest where the order parameter drops to zero. The direction is clockwise, so that the magnetic field caused by the supercurrent is opposite to the external field, which points in the positive z-direction.

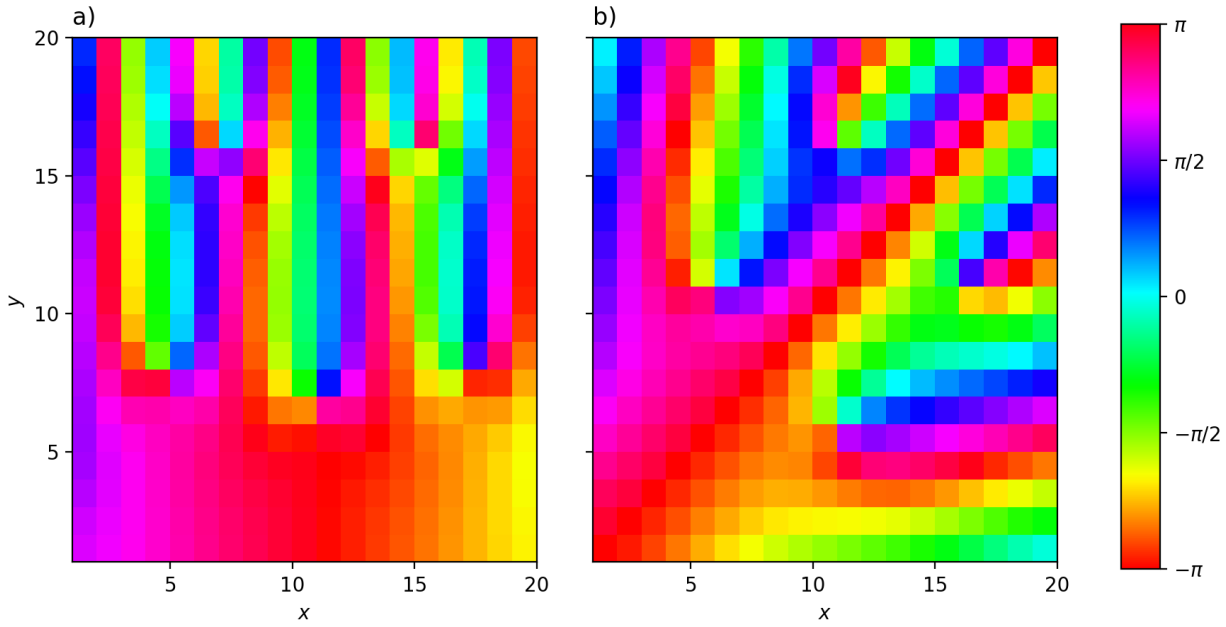

Figure 6.5: Colormaps of α_i for the two gauge choices discussed in the previous section. The connectivity of the phases at $\pm\pi$ is illustrated by the colorbar where these phases have the same color.

Despite these characteristics of vortices, we will look at the behaviour of the phase of the order parameter to decide if the vortex state really is present. In this section, the order parameter of the conventional s-wave superconductor will be considered for brevity. Based on the fact that the order parameter is a complex number, it can be written as

$$\Delta_i = |\Delta_i| e^{i\alpha_i}, \tag{6.62}$$

where α_i is its phase at site i. A discussion about how a vortex can be identified by the calculation of the phase change along the path enclosing the vortex, is given by Taylor [82]. In general, the phase change around a vortex is found to be $\Delta\alpha = 2\pi m$, $m \in \mathbb{Z}$. However, if the phase change between all points along the path

$$\Delta\alpha_{1,2} = \alpha_2 - \alpha_1, \tag{6.63}$$

is required to lie in the principal interval $-\pi < \Delta\alpha_{1,2} \leq \pi$, the total change about one vortex

will be $\pm 2\pi$. The rule to follow in order to achieve this, is

$$\begin{aligned} \Delta\alpha_{1,2} < -\pi \rightarrow & \Delta\alpha_{1,2} + 2\pi \\ \Delta\alpha_{1,2} > \pi \rightarrow & \Delta\alpha_{1,2} - 2\pi. \end{aligned} \tag{6.64}$$

This means that 2π is added whenever the phase change between two points is less than $-\pi$, and 2π is subtracted if it is greater than π. Here the fact that a phase change $\Delta\alpha$ is equivalent to $\Delta\alpha \pm 2\pi$, is exploited. To ensure that all occurring vortices are detected, the closed path will be along the system boundary. Additionally, the variations between all the nearest-neighbour sites on this path are taken into account, and they are added to the total, following the rule in equation (6.64). In figure 6.5, the phases of the cases treated previously, are shown. Computation of the total phase change gives $5 \cdot 2\pi$ in a) and $4 \cdot 2\pi$ in b), meaning that there are respectively 5 and 4 vortices present, as expected regarding the plots of $|\Delta_i|$ and the supercurrents. In the following, we will refer to the integer multiple of 2π as the winding number.

6.8 Difficulties in obtaining a self-consistent vector potential

Following the numerical procedure described so far in this chapter, we have not been successful in determining the vector potential self-consistently. First of all, we have tried to use a set of Dirichlet boundary conditions where A_x and A_y are fixed at boundary of the lattice, as depicted in figure 6.6. At each of the faces, $\boldsymbol{A}$ has been set equal to the vector potential only due to

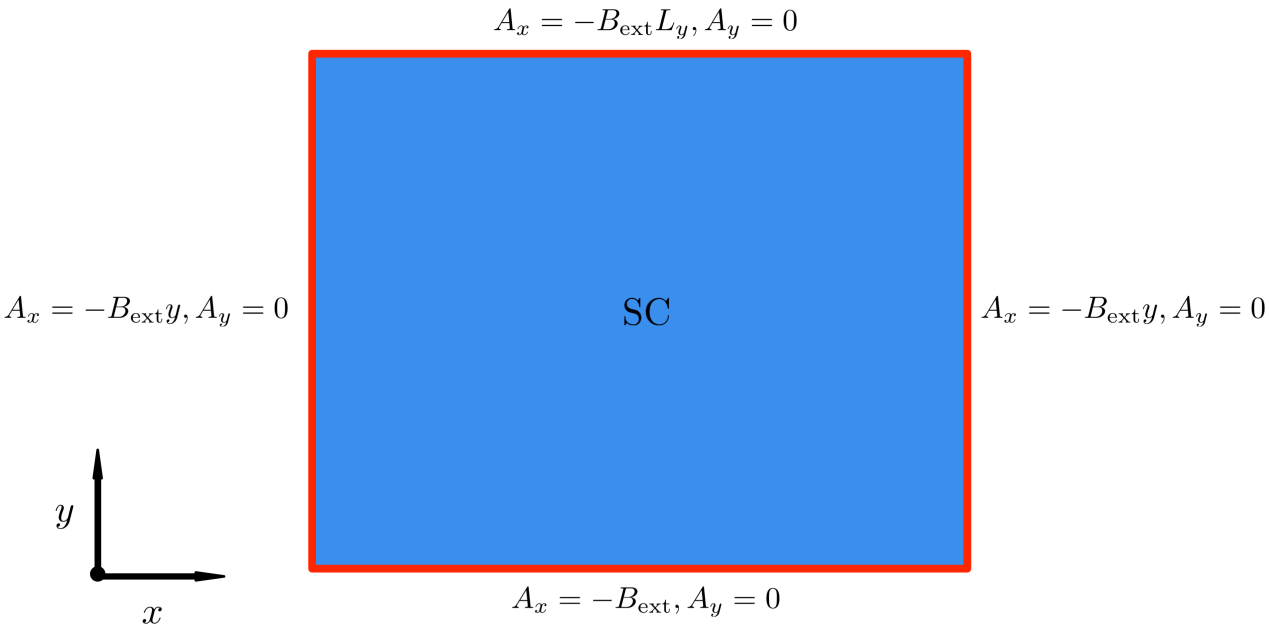

Figure 6.6: A possible choice of boundary conditions for the vector potential in the gauge $\boldsymbol{A}_{\text{ext}} = B_{\text{ext}}(-y, 0)$ for the external field. The red line marks the boundary of the system.

the external field, that is $\boldsymbol{A} = \boldsymbol{A}_{\text{ext}}$. Running the self-consistent algorithm described in section

6.5.3, there are no signs of convergence for $\boldsymbol{A}$. The vector potential takes on a new configuration in each iteration, in which both the magnitude and direction of $\boldsymbol{A}$ vary. This behaviour does not only occur when superconductivity is included in the system. Testing shows that the convergence is not improved significantly for the normal conducting state. Decomposing the different parts of the algorithm and testing each part individually, no sources of error are found. Comparison with analytical solutions of the Poisson equation indicate that the method of finite-differences is implemented properly. As well, the expression for the supercurrent should be correct.

This has forced us to look at alternative strategies for the implementation of self-consistent $\boldsymbol{A}$. These will be outlined in the following.

6.8.1 Alternative system configurations

A concern for the determination of a self-consistent vector potential is the uniqueness of $\boldsymbol{A}$. It could be that the changes in $\boldsymbol{A}$ from an iteration to the next appear as a consequence of the vector potential not being determined in a unique way. However, when $\boldsymbol{A}$ is fixed at each of the boundaries, this should not be the problem.

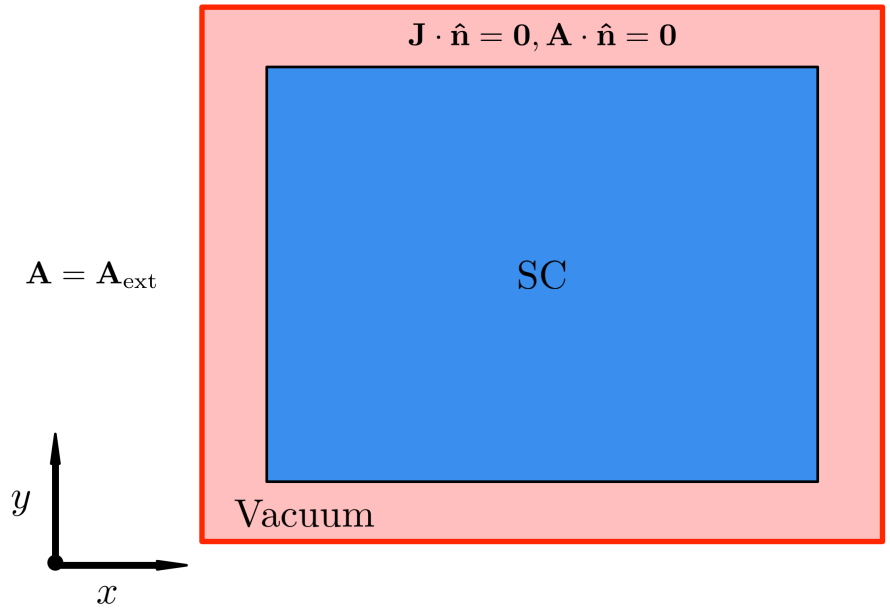

Figure 6.7: Alternative strategy of boundary conditions for self-consistency in $\boldsymbol{A}$. The boundary of the system (red line) is separated from the superconductor by a region of vacuum.

On the other hand, plotting the vector potential after a number of iterations, $\boldsymbol{A}$ tends to be too large out to the edges of the system, relative to its boundary values. The reason seems to be that the supercurrent is significant here. When the nearest-neighbour change in the vector potential between a non-boundary site and a boundary site is large, it could be that the self-consistent solution becomes unstable. If the supercurrent is too large in the proximity of the boundary, the influence of $\boldsymbol{A}$ being fixed at the boundary, is reduced. This is

a problem as it is the boundary values of the vector potential, and not the supercurrent that is known from the outset. To cope with this, we should find a way to enforce the supercurrent to decrease in magnitude as we move to the boundary. A first attempt is to add a region of vacuum from the superconductor and out to the boundary of the system. This is illustrated in figure 6.7. Here we keep the condition of $\boldsymbol{A} = \boldsymbol{A}_{\text{ext}}$ at the boundary of the system. At the interface between the superconductor and vacuum, we require that there is no supercurrent leaking into vacuum, that is having both the normal component of the supercurrent density ($\boldsymbol{J} \cdot \hat{\boldsymbol{n}}$) and the vector potential ($\boldsymbol{A} \cdot \hat{\boldsymbol{n}}$) equal to zero. In the tight-binding formalism used here, the vacuum will be modeled by having no hopping between nearest-neighbours. This means that the hopping amplitude is set to zero in this region of the system. To be more

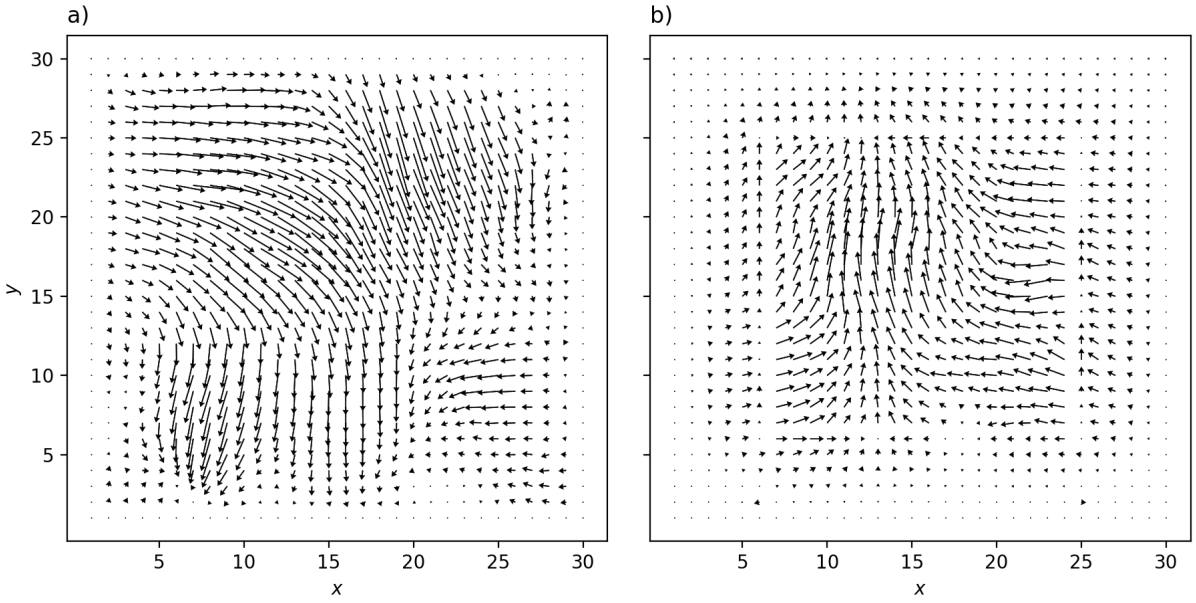

Figure 6.8: Vector potentials for the cases illustrated in figure 6.6 and 6.7. The number of iterations of the self-consistent algorithm is 100 in both plots. Input parameters are $V/t = -2.5$, $T/t = 0.0$, $\mu/t = 0.0$ and $\Phi_{\text{tot}} = 6\Phi_0$. $\boldsymbol{A}$ is plotted in units of $3\Phi_0$ in a) and $2\Phi_0$ in b), whereas the prefactors come from the scaling.

specific, setting the system size to $L_x = 30, L_y = 30$, there will be 5 vacuum sites on each side of the superconductor, including the boundary of the system. The vacuum-superconductor interfaces are then located between the vacuum and superconducting sites. The condition $\boldsymbol{J} \cdot \hat{\boldsymbol{n}}$ is implemented by having $t_{i,j} = 0$ when one of the sites is located in the vacuum and the other in the superconductor. Furthermore, the superconducting interaction strength is only non-zero inside the superconductor. The restriction of having only a non-vanishing parallel component of the vector potential at the vacuum-superconductor interfaces, is ensured by manipulating the finite-difference matrix in the Poisson equation. All matrix elements corresponding to the normal component of $\boldsymbol{A}$ at these interfaces are set to zero. Since the solution of Maxwell equation gives new values of $\boldsymbol{A}$ at all non-boundary sites, the normal component of the vector potential at sites of the interface is also manually set to zero.

Using this method, we do not find any significant improvements in the convergence of $\boldsymbol{A}$. Yet, the behaviour of the vector potential is somewhat improved in the sense that there are

smaller variations in $\boldsymbol{A}$ from non-boundary to boundary sites. This is exemplified by figure 6.8, which shows the vector potentials obtained after the same number of iterations using the two solution strategies discussed so far. In both cases, the system is initialized with non-zero paring amplitudes of the $(p_x + ip_y)(|\uparrow,\uparrow\rangle + |\downarrow,\downarrow\rangle)$-phase.

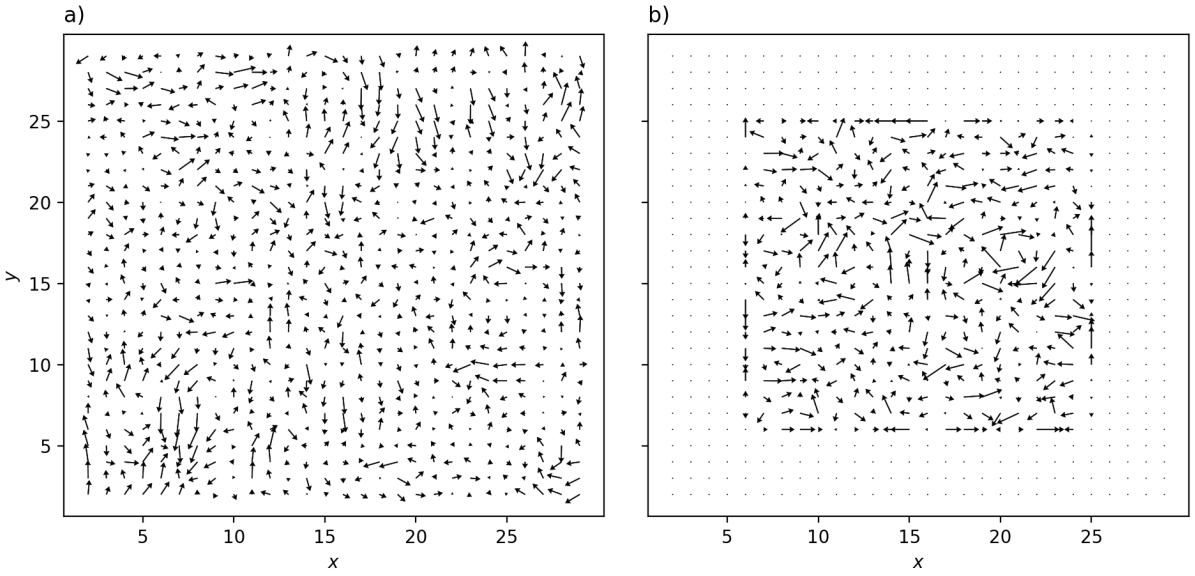

Figure 6.9: The corresponding supercurrents of figure 6.8. The vectors are plotted in units of $1.5t\Phi_0$ in a) and $t\Phi_0$ in b).

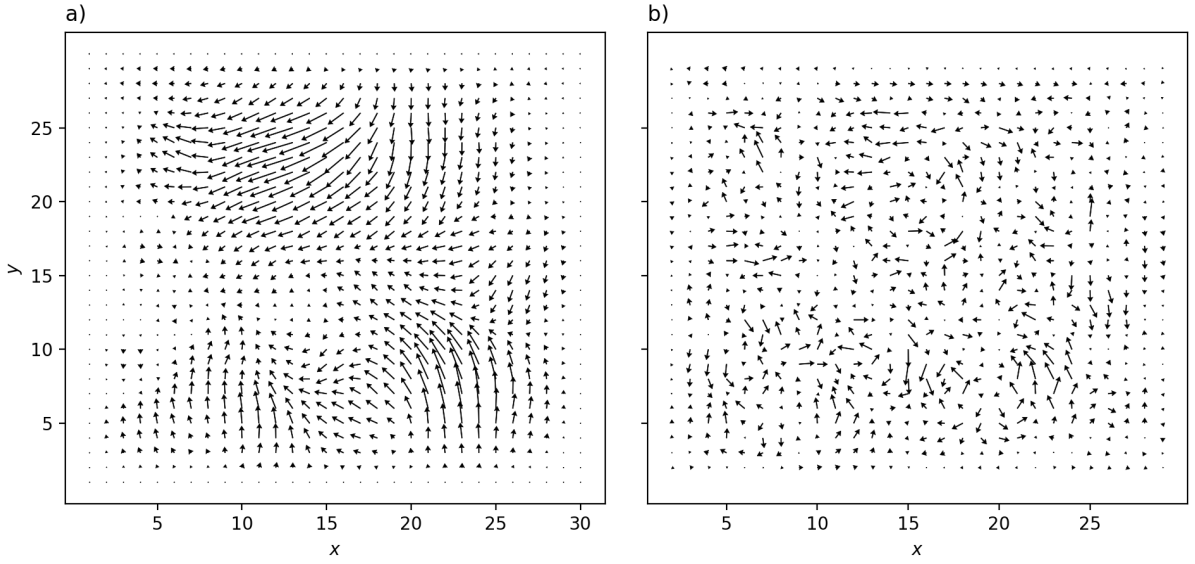

Figure 6.10: Vector potential (a) and supercurrent (b) when the hopping amplitude is successively reduced as elaborated in the main text. The parameters of the model are the same as before. The units are $3\Phi_0$ for $\boldsymbol{A}$ and $1.5t\Phi_0$ for the supercurrent.

A possible drawback of this solution strategy is that it still can be an abrupt drop in supercurrent from sites in the superconductor to sites in the vacuum. A better method can be

to reduce the conductivity in steps in the proximity of the edges of the system. In the search for a stable solution, the vacuum is replaced by a region of successively decreased magnitude of the supercurrent. On the basis of the supercurrent being proportional to t, we stepwise adjust the hopping amplitude. Numbering sites on the system boundary as 1, sites just inside these as 2, and continuing this counting up to 6, $t_{i,j}$ between 6 and 5, 5 and 4, 4 and 3, 3 and 2, and 2 and 1, is multiplied by factors of 0.8, 0.6, 0.4, 0.2 and 0.0, respectively. The probability of electron tunneling between sites of the same type will also be affected. The factor is 0.0 for tunneling $1 \leftrightarrow 1$, 0.2 for $2 \leftrightarrow 2$, 0.4 for $3 \leftrightarrow 3$, 0.6 for $4 \leftrightarrow 4$, and 0.8 for $5 \leftrightarrow 5$. To maintain the same relative magnitude of superconducting interaction strength and the hopping amplitude, $V_{i,j}$ is also made smaller at these sites by multiplication of the same factors as $t_{i,j}$.

Testing with a system size of $L_x = 30, L_y = 30$ as before, the self-consistent algorithm gives the vector potential and the supercurrent in figure 6.10. Of the cases discussed so far, the obtained vector potential is to some extent smoother than in figure 6.8. The changes of the vector potential are more gradual taking all lattice sites into consideration. Still, the self-consistent solution of $\boldsymbol{A}$ does not converge.

6.8.2 General form of the Maxwell equation

Another possibility is to solve the Maxwell equation directly, that is without the gauge condition $\nabla \cdot \boldsymbol{A} = 0$. Equation (6.31) then takes the form

$$\nabla^2 \boldsymbol{A} - \nabla(\nabla \cdot \boldsymbol{A}) = -\boldsymbol{J}. \tag{6.65}$$

The second term in $\boldsymbol{A}$, which is set to zero in the Coulomb gauge, couples A_x and A_y. Written out on component form, we have

$$\partial_y^2 A_x - \partial_x \partial_y A_y = -J_x \tag{6.66}$$

$$\partial_x^2 A_y - \partial_x \partial_y A_x = -J_y. \tag{6.67}$$

Using finite-differences, a representation of the mixed partial derivative in equations (6.66) and (6.67) is [77]

$$\begin{aligned} \partial_x \partial_y f(x,y) = &\frac{f(x+\Delta x, y+\Delta y) + f(x-\Delta x, y-\Delta y) - f(x+\Delta x, y-\Delta y)}{4\Delta x \Delta y} \\ &\underline{\frac{-f(x-\Delta x, y+\Delta y)}{}} + \mathcal{O}(\Delta x, \Delta y). \end{aligned} \tag{6.68}$$

Defining the column vectors

$$\boldsymbol{x} = \begin{pmatrix} A_x(2,2) \\ A_y(2,2) \\ \vdots \\ A_x(L_x-1, L_y-1) \\ A_y(L_x-1, L_y-1) \end{pmatrix}, \tag{6.69}$$

and

$$\boldsymbol{b} = \begin{pmatrix} J_x(2,2) + A_x(2,1) - \frac{1}{4}\big[A_y(1,1) - A_y(1,3) - A_y(3,1)\big] \\ J_y(2,2) + A_y(2,1) - \frac{1}{4}\big[A_x(1,1) - A_x(1,3) - A_x(3,1)\big] \\ \vdots \\ J_x(L_x-1, L_y-1) + A_x(L_x-1, L_y) - \frac{1}{4}\big[A_y(L_x, L_y) - A_y(L_x-2, L_y) - A_y(L_x, L_y-2)\big] \\ J_y(L_x-1, L_y-1) + A_y(L_x-1, L_y) - \frac{1}{4}\big[A_x(L_x, L_y) - A_x(L_x-2, L_y) - A_x(L_x, L_y-2)\big] \end{pmatrix}, \tag{6.70}$$

the matrix of the linear system of equations $\boldsymbol{W}\boldsymbol{x} = \boldsymbol{b}$ is

$$\boldsymbol{W} = \begin{pmatrix} 2 & 0 & 0 & 0 & -1 & 0 & 0 & \frac{1}{4} \\ 0 & 2 & 0 & -1 & 0 & 0 & \frac{1}{4} & 0 \\ 0 & 0 & 2 & 0 & 0 & -\frac{1}{4} & -1 & 0 \\ 0 & -1 & 0 & 2 & -\frac{1}{4} & 0 & 0 & 0 \\ -1 & 0 & 0 & -\frac{1}{4} & 2 & 0 & 0 & 0 \\ 0 & 0 & -\frac{1}{4} & 0 & 0 & 2 & 0 & -1 \\ 0 & \frac{1}{4} & -1 & 0 & 0 & 0 & 2 & 0 \\ \frac{1}{4} & 0 & 0 & 0 & 0 & -1 & 0 & 2 \end{pmatrix}, \tag{6.71}$$

in the special case of $L_x = 4$, $L_y = 4$. Numerically, for larger systems the entries of the matrix

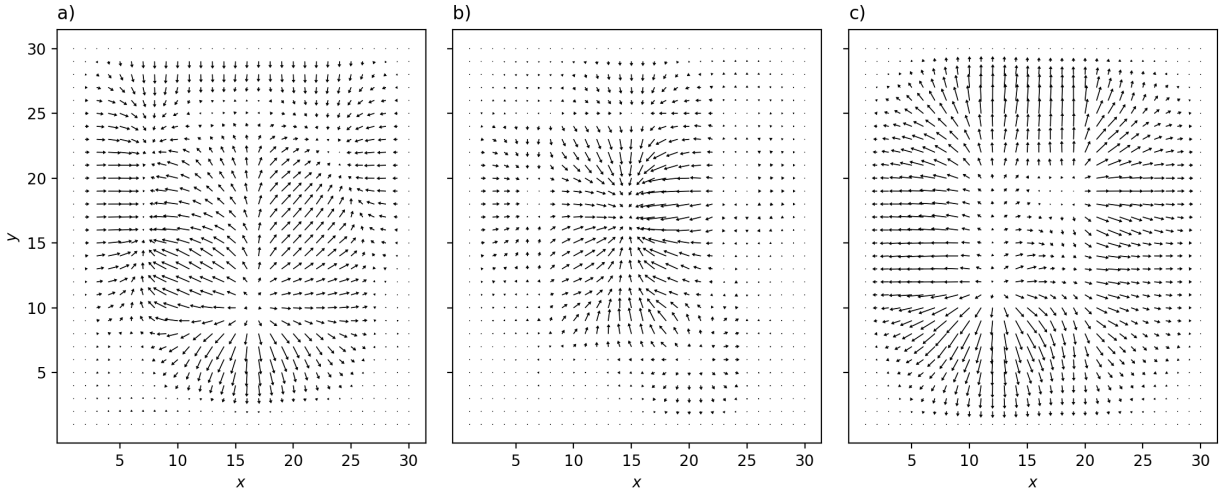

Figure 6.11: $\boldsymbol{A}$ in the three system configurations for the general form of the Maxwell equation. The parameters of the model are the same as in the previous subsection, and the plots are obtained after 100 iterations. The naming of the plots corresponds to the order of which these concepts were introduced. All plots are heavily scaled, that is units of $200\Phi_0$ for a), $150\Phi_0$ for b), and $200\Phi_0$ for c).

are determined by exploiting the 8-point stencil structure of this system of equations. The matrix size is $2(L_x - 2)(L_y - 2) \times 2(L_x - 2)(L_y - 2)$, and A_x and A_y are fixed at the system boundary as we are considering Dirichlet boundary conditions.

Figure 6.8 demonstrates the effect of solving the general form of the Maxwell equation. According to these plots, the divergence of the vector potential, that is $\nabla \cdot \boldsymbol{A}$, now completely dominates. Anyhow, this part of $\boldsymbol{A}$ can be gauged away, so it is not of physical importance. What matters is that solving equation (6.65) instead of equation (6.31), has not led to any improvements in the convergence of the vector potential.

6.9 Concluding remarks

Regarding all the testing done to find any sources of error, it is quite unlikely that the methods outlined in this chapter are implemented in a wrong way. Probably, something inherent to

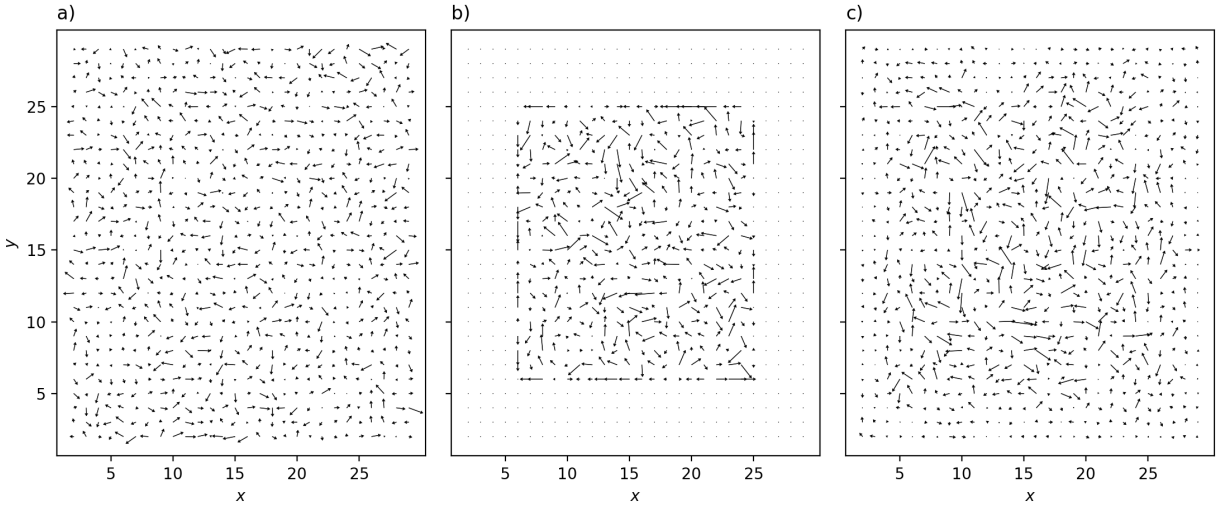

Figure 6.12: Supercurrents in units of $t\Phi_0$ for the three cases in figure 6.11.

the model is invalid, causing the instability of the self-consistent solution of $\boldsymbol{A}$. Paying special attention to the modeling of the vector potential in terms of the Peierls formalism, it can only be justified as long as the vector potential is slowly varying at the scale of the lattice spacing. Numerical values of the maximal changes in A_x and A_y among nearest-neighbour sites, indicate that this can be a problem. It certainly is when the Maxwell is solved without setting $\nabla \cdot \boldsymbol{A} = 0$. As evident from figure 6.11, the variations are in this case not small relative to the interatomic distance ($a = 1$). Solving the Poisson equation instead, the maximum change in $\boldsymbol{A}$ (in units of Φ_0) is typically between 0.5 and 1.0, but it can be significantly higher too. Based on these observations, we can not conclude whether the approximation expressed by the Peierls phase is the source for the instability of the self-consistent solution. At least, we have pointed out a possible source of error.

Chapter 7

Spontaneous vortex phase without self-consistently solving the Maxwell equation

In this chapter, the spontaneous vortex phase will explored. This will be done without solving the Maxwell equation, which has turned out to be problematic. Nevertheless, solution strategies where the spontaneity of the vortex phase arises from the magnetization alone will be presented. The is considered to be a good approximation for extreme type II superconductors with a large GL parameter. The magnetization of the system will be determined using two methods. Firstly, it will be fixed to the bulk system magnetization by the requirement of having a significantly higher magnetization than superconductivity in the system. Secondly, the vector potential will be computed iteratively from the global finite-size system magnetization, and there will be no criterion for the magnitude of the magnetization relative to the superconductivity. We start by the introduction of the so-called magnetic translation operators. Exploiting the symmetries of these operators, a possibility is to use quasiperiodic instead of open boundary conditions. In the last part of the chapter, the phase diagrams are discussed, and some final remarks are also given.

7.1 Magnetic translation symmetry

The concept of the magnetic translation symmetry outlined here is examined by Zhu, Aidelsburger and Bernevig [70, 72, 83]. As emphasized in the previous chapter, the Peierls phase breaks the translational symmetry of the Hamiltonian of a bulk superconductor. Accordingly, it will in this section only be necessary to study the hopping part of the Hamiltonian, that is

$$\hat{H} = \hat{T}_x + \hat{T}_y + \text{h.c.}, \tag{7.1}$$

where

$$\hat{T}_x = \sum_{m_x,m_y} \hat{c}^\dagger_{m_x+1,m_y} \hat{c}_{m_x,m_y} e^{i\phi^x_{m_x,m_y}} \tag{7.2}$$

$$\hat{T}_y = \sum_{m_x,m_y} \hat{c}^\dagger_{m_x,m_y+1} \hat{c}_{m_x,m_y} e^{i\phi^y_{m_x,m_y}}. \tag{7.3}$$

Because of $[\hat{T}_x, \hat{T}_y] \neq 0$, the translation operators $\hat{T}_x$ and $\hat{T}_y$ do not commute with the Hamiltonian in equation (7.1). We therefore construct the magnetic translation operators $\hat{M}_x$ and $\hat{M}_y$ as

$$\hat{M}_x = \sum_{m_x,m_y} \hat{c}^\dagger_{m_x+1,m_y} \hat{c}_{m_x,m_y} e^{i\theta^x_{m_x,m_y}} \tag{7.4}$$

$$\hat{M}_y = \sum_{m_x,m_y} \hat{c}^\dagger_{m_x,m_y+1} \hat{c}_{m_x,m_y} e^{i\theta^y_{m_x,m_y}}, \tag{7.5}$$

The phases in equations (7.4) and (7.5), $\theta^x_{m_x,m_y}$ and $\theta^y_{m_x,m_y}$, should be determined so that $[\hat{M}_{x(y)}, \hat{H}] = 0$ holds. In appendix A.4, it is motivated that this is fulfilled for

$$\theta^x_{m_x,m_y} = \phi^x_{m_x,m_y} - \pi \frac{\Phi_{m_x,m_y}}{\Phi_0} m_y \tag{7.6}$$

$$\theta^y_{m_x,m_y} = \phi^y_{m_x,m_y} + \pi \frac{\Phi_{m_x,m_y}}{\Phi_0} m_x. \tag{7.7}$$

In the particular case of a homogeneous magnetic field ($\Phi_{m_x,m_y} = \Phi$), it can be shown that $\hat{M}_x \hat{M}_y = e^{-i\pi\Phi/\Phi_0} \hat{M}_y \hat{M}_x$. As a result, $[\hat{M}_x, \hat{M}_y] = 0$ if $\Phi/\Phi_0 = 2l$, $l \in \mathbb{Z}$. Even so, this is physically equivalent to having no magnetic flux. On the other hand, we can consider the magnetic translation operators along the edges of a supercell of size $L_x \times L_y$, called the magnetic unit cell (MUC) . These translations are products of $\hat{M}_x$ and $\hat{M}_y$, satisfying

$$\hat{M}_x^{L_x} \hat{M}_y^{L_y} = e^{-i\pi L_x L_y \Phi/\Phi_0} \hat{M}_y^{L_y} \hat{M}_x^{L_x}, \tag{7.8}$$

where $\hat{M}_x^{L_x}$ and $\hat{M}_y^{L_y}$ are the magnetic translation operators of the MUC. These commute if $\Phi/\Phi_0 = 2p/L_x L_y$, $p \in \mathbb{Z}$. Thus, the MUC has a total flux of $\Phi_{\text{tot}} = 2p\Phi_0$. Using that $\Phi/\Phi_0 = B$, equations (6.26) and (6.27) inserted in equations (7.6) and (7.7) result in

$$\theta^x_{m_x,m_y} = 0 \tag{7.9}$$

$$\theta^y_{m_x,m_y} = \pi \frac{\Phi}{\Phi_0} m_x. \tag{7.10}$$

Since the magnetic translation operators of the MUC commute both with each other and with the Hamiltonian, it is possible to find simultaneous eigenstates of these operators. Such states are magnetic Bloch states with $\boldsymbol{k}$ as a good quantum number. In the generalized Bloch theorem, Bogoliubov states on the form $\begin{pmatrix} u_{\boldsymbol{k}}(\boldsymbol{r}) \\ v_{\boldsymbol{k}}(\boldsymbol{r}) \end{pmatrix}$, have the property [81]

$$\begin{pmatrix} u_{\boldsymbol{k}}(\boldsymbol{r}+\boldsymbol{R}_n) \\ v_{\boldsymbol{k}}(\boldsymbol{r}+\boldsymbol{R}_n) \end{pmatrix} = e^{i\boldsymbol{k}\cdot\boldsymbol{R}_n} \begin{pmatrix} e^{-i\chi(\boldsymbol{r},\boldsymbol{R}_n)/2} u_{\boldsymbol{k}}(\boldsymbol{r}) \\ e^{i\chi(\boldsymbol{r},\boldsymbol{R}_n)/2} v_{\boldsymbol{k}}(\boldsymbol{r}) \end{pmatrix}, \tag{7.11}$$

where $\boldsymbol{R}_n = n_x L_x \hat{\boldsymbol{x}} + n_y L_y \hat{\boldsymbol{y}}$, that is a translation vector consisting of n_x and n_y MUC translations in the x- and y-direction. Here the components of $\boldsymbol{k}$ are

$$k_{\beta=x,y} = \frac{2\pi}{L_\beta N_\beta} l_\beta, \qquad l_\beta = 0, 1, ..., N_\beta - 1, \tag{7.12}$$

where N_x and N_y are the number of MUCs in the x- and y-direction. According to equation (7.11), the coherence factors have a Bloch-like symmetry under a MUC translation. The difference is that an additional complex phase is acquired due to the presence of the magnetic field. This phase is given by [70]

$$\begin{aligned}\chi(\boldsymbol{r}, \boldsymbol{R}_n) &= \frac{2\pi}{\Phi_0}\boldsymbol{A}(\boldsymbol{R}_n)\cdot\boldsymbol{r} \\ &= -\frac{2\pi}{\Phi_0}Bn_yL_ym_x = -2\pi\frac{\Phi}{\Phi_0}n_yL_ym_x.\end{aligned} \tag{7.13}$$

The last line is valid for the gauge $\boldsymbol{A} = B(-y, 0)$, and the position vector can be written as $\boldsymbol{r} = m_x\hat{\boldsymbol{x}} + m_y\hat{\boldsymbol{y}}$. Implementing the quasiperiodic boundary conditions illustrated in figure 7.1, a system of size $L_xL_yN_xN_y$ can be divided into N_xN_y MUCs of size L_xL_y. The effect is that the eigenvalue problem is transformed into the diagonalization of N_xN_y matrices of dimension $2L_xL_y$ instead of having to diagonalize a matrix of dimension $2L_xL_yN_xN_y$.

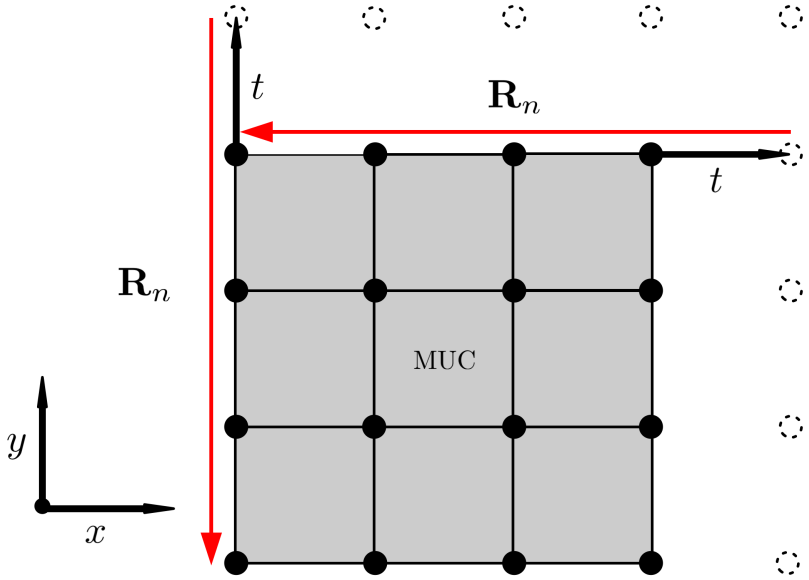

Figure 7.1: MUC of size $L_x = 4, L_y = 4$ (grey region). A nearest-neighbour hopping or superconducting correlation to a site outside of the MUC (dashed circles) is accompanied by the magnetic translation represented by $\boldsymbol{R}_n$, whereas a complex phase is added to the coherence factors as in equation (7.11). This figure is inspired by figure in the reference [81].

7.2 Vortex state for open and quasiperiodic boundary conditions

To check that the quasiperiodic boundary conditions are implemented correctly, the Hoftstadter butterfly is plotted in figure 7.2 [34]. This is the band structure of electrons exposed to an uniform magnetic field and moving in a periodic potential. Comparing the spectra obtained using

quasiperiodic and open boundary conditions, there are states in plot b) inside the forbidden regions in plot a). As discussed by Analytis *et al.* [84], the band structure for open boundary conditions will approach the one for quasiperiodic boundary conditions as the number of lattice sites is increased.

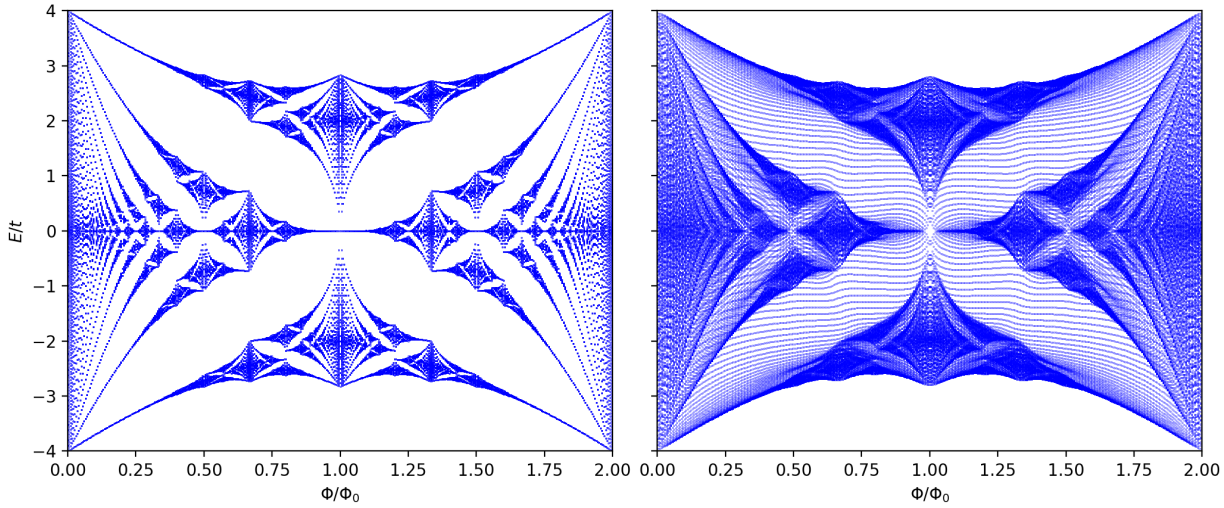

Figure 7.2: Hofstadter butterfly, that is the energy spectrum of electrons in a constant magnetic field, in the case of quasiperiodic (a) and open boundary conditions (b). The energy values are given as a function of the magnetic flux through each unit cell, and the system size is $L_x = 20, L_y = 20$ in both plots.

With regards to differences between the two sets of boundary conditions, it is interesting to analyze what happens with the equal-spin p-wave vortex phase in a constant magnetic field. Open boundary conditions are used in figure 7.3. Interestingly, $|\Delta^{\uparrow,\uparrow}_{p_x,i} + \Delta^{\downarrow,\downarrow}_{p_x,i}|$ is heavily suppressed along the system boundaries with normal vectors $\hat{\boldsymbol{n}} = \pm\hat{\boldsymbol{x}}$. This can be understood by the concept of zero-energy states (ZES). As the name suggests, these are mid-gap states leading to a finite DOS at the Fermi level. If such states appear, the superconducting order parameter can have a phase shift of π. For p_x-superconductors ZES occur in the proximity of a vacuum-superconductor interface. Using open boundary conditions, we are essentially modeling a superconductor in conjunction with vacuum, as the hopping amplitude $t_{i,j}$ and the superconducting interaction $V_{i,j}$ are zero when i or j is outside the superconductor. Therefore, the p_x order parameter in figure 7.3 is significantly smaller close to $x = 1$ and $x = L_x$ than in the superconducting bulk. The opposite happens at the boundaries $y = 1$ and $y = L_y$, where the order parameter is enlarged. For more details about ZES, we refer to appendix B showing additional results. Studying the p_y order parameters, there are suppressions at $y = 1$ and $y = L_y$ and enlargements at $x = 1$ and $x = L_x$.

As seen from figure 7.4, the situation is different in the case of quasiperiodic boundary conditions. Since lattice sites on opposite edges of the MUC are connected by magnetic translation operators, the suppression of Δ_{p_x} due to ZES vanishes. As opposed to figure 7.3, the behaviour of the order parameter indicates the presence of two vortices. Controlling this observation by calculation of the total phase change along the system boundary, confirms that there really are two vortices in figure 7.4, and no vortex state is obtained for open boundary conditions.

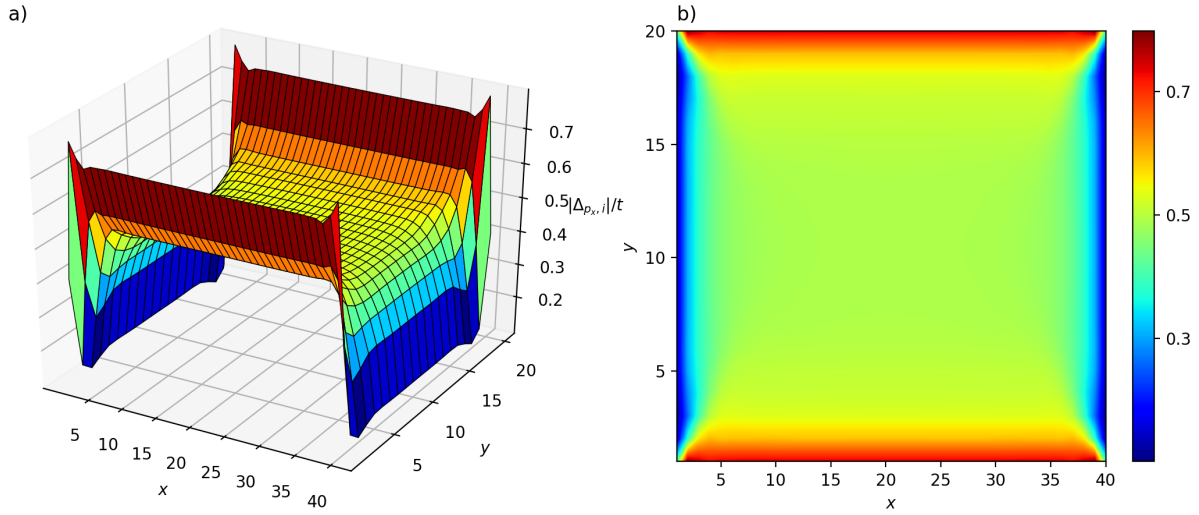

Figure 7.3: $|\Delta^{\uparrow,\uparrow}_{p_x,i} + \Delta^{\downarrow,\downarrow}_{p_x,i}|$ for the self-consistent solution initialized with non-zero order parameters of $p_x + ip_y$ and open boundary conditions. The equal-spin superconductor is exposed to a homogeneous magnetic field corresponding to a total magnetic flux of $2\Phi_0$. The physical parameters are $V/t = -4.0, \mu/t = -1.5$ and $T/t = 0.2$, and the dimensions of the system is $L_x = 40, L_y = 20$. For simplicity, the magnetic interactions are here set to zero.

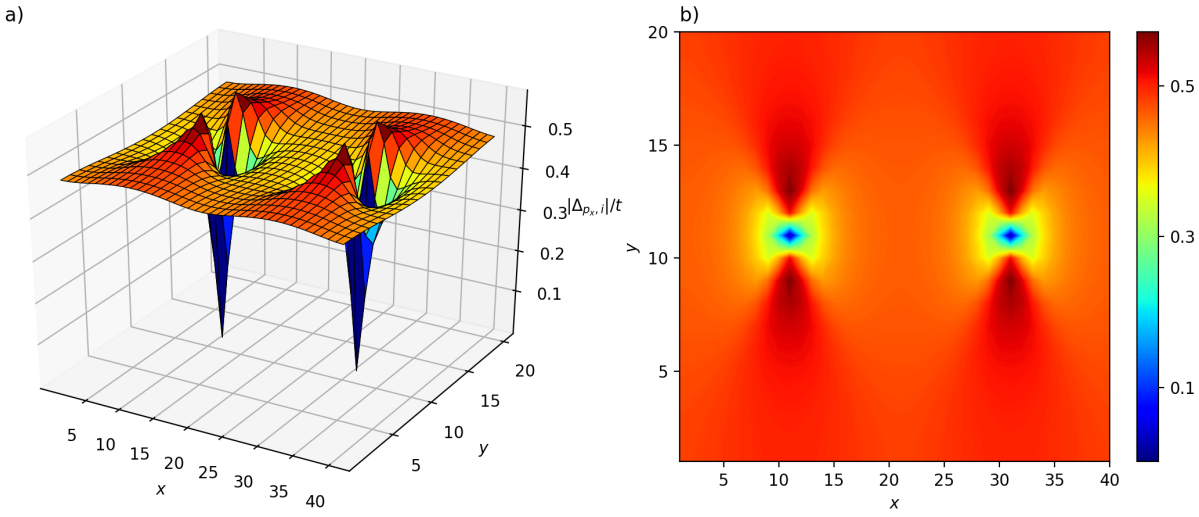

Figure 7.4: Similar plots as in figure 7.3 with quasiperiodic boundary conditions implemented.

The interpretation is that the p-wave vortices are more easily formed when the influence of boundary effects is small. Increasing the magnetic field, the p-wave vortex state is also created in the case of open boundary conditions.

We also observe that the vortices in figure 7.4 are anisotropic. Relative to the vortex core, the p_x order parameter decays more rapidly in the y-direction than in the x-direction. Going back to chapter 4 and figure 4.2, the gap function of p_x at $\mu/t = -1.5$ is elongated in the

x-direction, while it has a nodal line along the y-direction. This symmetry is reflected in the structure of its vortices, being more extensive in the direction of the x-axis.

7.3 Methods for investigation of the spontaneous vortex phase of extreme type II superconductors

As it stands, the effect of the supercurrent will be ignored by the assumption of having a large GL parameter κ. As mentioned in section 6.4, type II superconductors satisfy $\kappa > 1/\sqrt{2}$. In this respect, extreme type II superconductors do have a GL parameter $\kappa \gg 1$ in general. For high-temperature cuprates, we can have $\kappa \approx 100$ [85]. In the GL theory of superconductivity, one finds that the magnetic field set up by the supercurrent is proportional to $1/\kappa^2$ [86]. This means that the screening effect of the supercurrent will be small when κ is large. In the case of extreme type II superconductors, it is therefore expected that the exclusion of the supercurrent in the model, is a good approximation.

7.3.1 Spontaneity due to magnetization

In this chapter, the spontaneity of the vortex phase is caused by the presence of FM order in the system. The magnetic field B produced by alignment of electronic spins is simply related to the magnetization M by

$$B = M, \tag{7.14}$$

in the chosen system of units. Since the electrons are modeled as having spins pointing along the z-axis, we have used scalar quantities in equation (7.14). This means that the vector potential and the Peierls phase can be computed directly from the magnetization using equation (6.2). In the following, the magnetization M will be assumed to be the same for all sites in the lattice. As mentioned in the beginning of this chapter, we will consider two methods for the computation of M. In the first method, which will be referred to as Method 1, we will require that the magnetization is large in comparison with the maximal value of the p-wave superconducting order parameters. Quantitatively, the criterion is

$$M > 4\max_i|VF_i|, \tag{7.15}$$

where F_i denotes the different p-wave paring amplitudes at site i, and the meaning of $\max_i$ is the maximal value when all lattice sites i are accounted for. In this way, the magnetic energy scale will be large relative to the superconducting condensation energy. Fixing M to the bulk system magnetization for the normal conducting state, is then expected to be a good approximation. More specifically, for a given set of physical parameters, M will be set to the magnetization obtained from the self-consistent solution of the $\boldsymbol{k}$-space BdG equations in chapter 5.

In the second method, that is Method 2, M is computed in each iteration through the global finite-size system magnetization (see equation (6.20)). Hence, the vector potential and the Peierls phase will also be updated iteratively. Yet, as the vector potential is here directly related to the magnetization, which is determined self-consistently through the average number operators, there is no need for a specific self-consistency criterion for $\boldsymbol{A}$, like we had in the previous chapter. Using this method, the magnitude of the magnetization will not be restricted in relation to the superconductivity. We also note that the start value of M for Method 2 will be the bulk system magnetization, which is fixed in Method 1.

7.3.2 System size

In the case of open boundary conditions, the system size L_x, L_y will be fixed regardless of what the magnetic flux is. The same strategy is not appropriate using magnetic translation operators, which will be considered as part of Method 1. Then the system size should be chosen so that $\Phi_{\text{tot}} = 2n\Phi_0$, where n is a positive integer. Given an uniform magnetization M, the total magnetic flux is

$$\Phi_{\text{tot}} = ML_xL_y\Phi_0. \tag{7.16}$$

Numerically, there are other restrictions on the dimensions of the system. L_x and L_y should not be too small as this would lead to unreliable results. Moreover, the run-time of the self-consistent algorithm is obviously an issue. In real space with the Peierls phase included in the model, the convergence becomes much slower. Accordingly, there is also an upper limit for the size of the system. Setting $L_x = L_y = L$, a compromise between these contradictions is to search for L in the interval $[10, 18]$. Thus, the procedure is to calculate n from

$$n = \frac{ML^2}{2}, \tag{7.17}$$

for $L \in [10, 18]$, and then to choose the value of L where n is closest to being an integer. In the strictest sense, the commutation of the magnetic translation operators will in general be violated due to the bounds of L.

7.3.3 Superconducting phases in a finite-size system

In comparison with the bulk $\boldsymbol{k}$-space Hamiltonian, the self-consistent solution of equation (6.10) behaves differently in the sense that both the real and imaginary part of the p-wave order parameters can be significantly different from zero. Indeed, the real and imaginary part are often on the same order of magnitude. In the case of a finite-size system, this happens regardless of the paring amplitudes being initialized with only non-zero real or imaginary part. Previously, when there was no magnetic flux through the system, a superconducting state initialized with the momentum symmetry of $p_x + ip_y$, converged to a solution having only significant real part of F_{p_x} and imaginary part of F_{p_y}. As a consequence, we can not distinguish between superconducting states like $p_x \pm ip_y$ and $p_x \pm p_y$, as we could in chapter 5. We can only decide whether both the p_x and p_y correlation functions are present, or one of them. In addition, the distinction between up- and down-spin remains. For a convergent solution of the self-consistent algorithm, we explicitly check if the superconducting p_x and p_y order parameters are significantly large. For instance, this means that initial conditions with only the p_x paring amplitudes non-zero, can result in a solution where both p_x and p_y are significant, that is the phase $p_x + p_y$. Of all the solutions giving for example $(p_x + p_y)|\uparrow,\uparrow\rangle$, we choose the one having lowest free energy. Further, the free energy of the different phases are compared to find the most stable state for a set of input parameters.

7.3.4 Gauges of the magnetic vector potential

Referring to the discussion about the gauge freedom in section 6.6, we can obtain distinct metastable states using different gauges for fixed initial conditions of the paring amplitudes. In principle, the number of possible gauges for a constant magnetic field is infinite. As different

vortex configurations can have different free energies, a large number of gauges should basically be considered. Numerically, this solution strategy is extremely time-consuming. We therefore have to restrict ourselves to a minimum of possible gauges. First of all, testing indicates that adding a constant to the vector potential does not result in different vortex configurations. In addition, we expect that the difference between gauges like $\boldsymbol{A} = B(-y, 0)$ and $\boldsymbol{A} = B(0, x)$, will be small. Accounting for these considerations, the possible gauges will be limited to the Landau gauge $\boldsymbol{A} = B(-y, 0)$ and the symmetric gauge $\boldsymbol{A} = 1/2B(-y, x)$.

7.4 Results and discussion

The relative iteration tolerance for the electron densities and the superconducting order parameters used here is 1.0E-3. This means that the relative change of all the local self-consistent parameters should be lower than the tolerance in order to obtain a convergent solution. As previously, the tolerance in T/t for the bisection method is 1.0E-3.

This section is divided into two parts. Firstly, phase diagrams computed using Method 1 are presented and discussed. Secondly, we will examine the results obtained from Method 2. In both cases, we follow the procedure outlined in section 6.7, where vortices are detected by the phase change of the p-wave superconducting order parameter of interest. Put differently, we define the vortex state as having a non-zero winding number for the system. If the self-consistent algorithm converges to a solution with significant up- and down-spin p_x and p_y order parameters, the phase change of $\Delta_{p_x}^{\uparrow,\uparrow} + \Delta_{p_y}^{\uparrow,\uparrow} + \Delta_{p_x}^{\downarrow,\downarrow} + \Delta_{p_y}^{\downarrow,\downarrow}$ is computed. Analogously, if the solution for instance only has non-vanishing $\Delta_{p_x}^{\uparrow,\uparrow}$, we consider the winding number of this order parameter.

7.4.1 Method 1: Fixed bulk system magnetization

Figure 7.5 shows a phase diagram of an equal-spin p-wave superconductor when the FM state is modeled by the exchange field h. Accordingly, the naming of the phases is with respect to superconducting properties, as all phases have FM order. Regarding subsection 7.3.3, the meaning of $(p_x + p_y)|\uparrow,\uparrow\rangle$ is that the up-spin components of F_{p_x} and F_{p_y} are finite, and we avoid going into details about the significance of the real and imaginary parts of these paring amplitudes. In order to satisfy the criterion of having a much higher magnetization than superconductivity, quantitatively expressed by equation (7.15), the parameters of the model are chosen carefully. As we have seen, making the exchange field stronger, leads to a higher degree of splitting between up- and down-spin electrons, and consequently, a greater magnetization. However, choosing a too large value of h, results in a magnetic field destroying the superconducting state. Moreover, the magnitude of the FM order varies with the chemical potential. Moving away from half-filling, M is gradually reduced. Taking these aspects into account, a possible choice of interaction strengths are $h/t = 3.0$ and $V/t = -2.0$ on the interval $\mu/t = [-1.5, 0.0]$, which is a relatively small portion of the range from zero degree of filling to half-filling ($\mu/t = [-7.0, 0.0]$).

In the parts of the phase diagram having finite superconductivity, the system is found to be in the vortex state. Since the magnetic flux through the system originates solely from the magnetization, the vortex phase can be classified as spontaneous. With regards to figure 5.3 showing the exchange field phase diagram of a bulk superconductor, there are several similarities. As before, both the p_x and p_y superconducting order parameters are non-zero. The

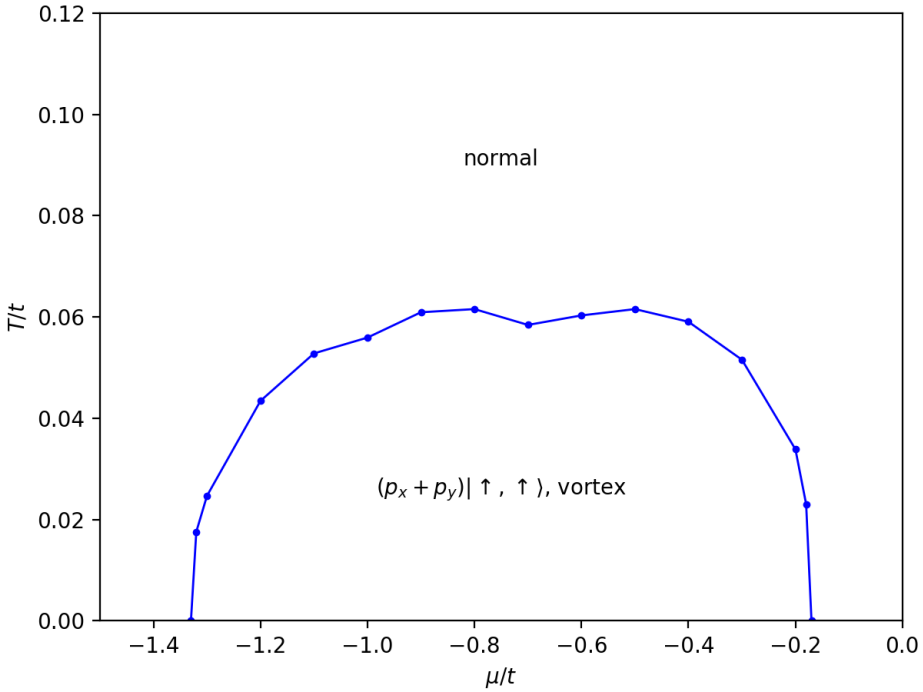

Figure 7.5: Phase diagram of an equal-spin p-wave superconductor in the case of open boundary conditions and fixed magnetization (Method 1). Parameters are $h/t = 3.0$ and $V/t = -2.0$. The system size is $L_x = 15, L_y = 15$.

difference is, as emphasized, that both the real and imaginary part of Δ_{p_x} and Δ_{p_y} contribute. As well, the combined spin configuration $|\uparrow,\uparrow\rangle + |\downarrow,\downarrow\rangle$ does not appear. The self-consistent algorithm converges to a solution having purely up-spin superconducting correlations below half-filling at $\mu/t = 0.0$. In fact, we could have extended the range of the chemical potential to include the symmetric region $\mu/t = [0.0, 1.5]$ about half-filling. Also here, the magnetization is adequately large with respect to the superconductivity. Examining this region, the same happens as for a bulk superconductor without magnetic flux. We have particle-hole symmetry if the spin direction is simultaneously switched. Formulated in another way, the vortex phase of $(p_x + p_y)|\downarrow,\downarrow\rangle$ is the most stable phase above half-filling. The fact that the single spin configurations are preferable is due to the high value of h. As a result, the up-spin band is located at much lower energies than the down-spin band below half-filling, and the opposite is the case for $\mu/t > 0.0$. The strong exchange field also gives a high number of flux quanta through the system. As long as the superconductivity is not completely destroyed, it is reasonable that the vortex state exists. The behaviour of the superconducting FM phase with respect to the normal state of FM for increasing temperatures is also similar to the non-flux case. For higher temperatures than at the transition, the FM phase without superconductivity has lowest free energy, despite the superconductivity still being significant. Again, a higher degree of FM order in the normal conducting state can be beneficial as the superconducting condensation energy becomes lower for increasing thermal fluctuations.

Implementing quasiperiodic boundary conditions as described in section 7.3.2, the μ-T phase diagram is slightly changed (see figure 7.6). Even so, the phase diagram has the same features as before. On the other hand, further analysis of the two phase diagrams computed for $h/t = 3.0$,

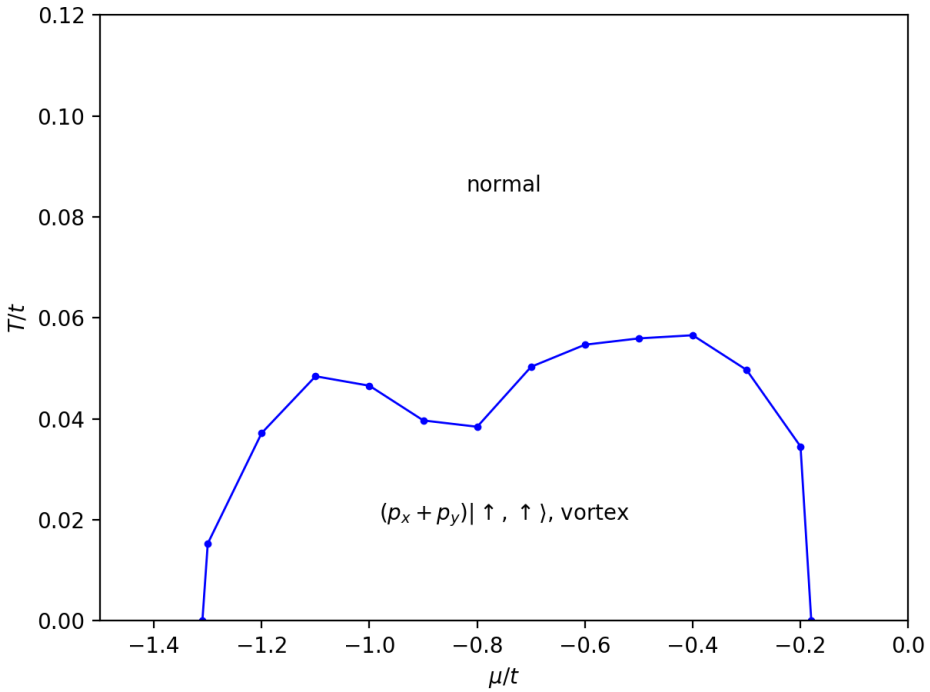

Figure 7.6: Similar plot as in figure 7.6 (Method 1) for variable system size and quasiperiodic boundary conditions.

signals a serious unreliability in the results. Studying the behaviour of the superconducting order parameters in the absence of a magnetic field for this value of h, the superconductivity is largest approximately at $n_e = 0.5$, that is around $\mu/t = -3.0$. Away from this electron density, the superconductivity becomes progressively weaker. It is negligible from about $\mu/t = -1.0$ and up to $\mu/t = 0.0$, and likewise above half-filling. Turning on the magnetic field, the phase diagrams suggest that the superconductivity can be finite in this region, which has no physical meaning. Actually, the development of the superconducting order parameters is meaningful at lower chemical potentials than shown in the phase diagrams. The problem is that here the criterion in equation (7.15) is violated by a too low magnetization relative to the superconductivity. The maximal superconductivity in the case of updated M, is obtained close to $\mu/t = -3.4$. Since the magnetic field becomes smaller for decreasing electron densities, it makes sense that the maximum is located at a slightly lower chemical potential than in the absence of a magnetic field. For increasing electron densities, the superconductivity disappears in the proximity of $\mu/t = -2.2$. This is also reasonable considering that a sufficiently strong magnetic field can destroy the superconducting condensate.

7.4.2 Method 2: Updated global finite-size system magnetization

To control that the unreliability is not caused by the implementation of Method 1, a similar phase diagram is computed using Method 2. Comparing figure 7.7 to figures 7.5 and 7.6, the problem is not solved by updating M through the computation of the global finite-size system magnetization. We observe that the spontaneous vortex region of figure 7.7 is shifted to the right on the interval $\mu/t = [-1.5, 0.0]$. This seems to be a result of having a smaller global

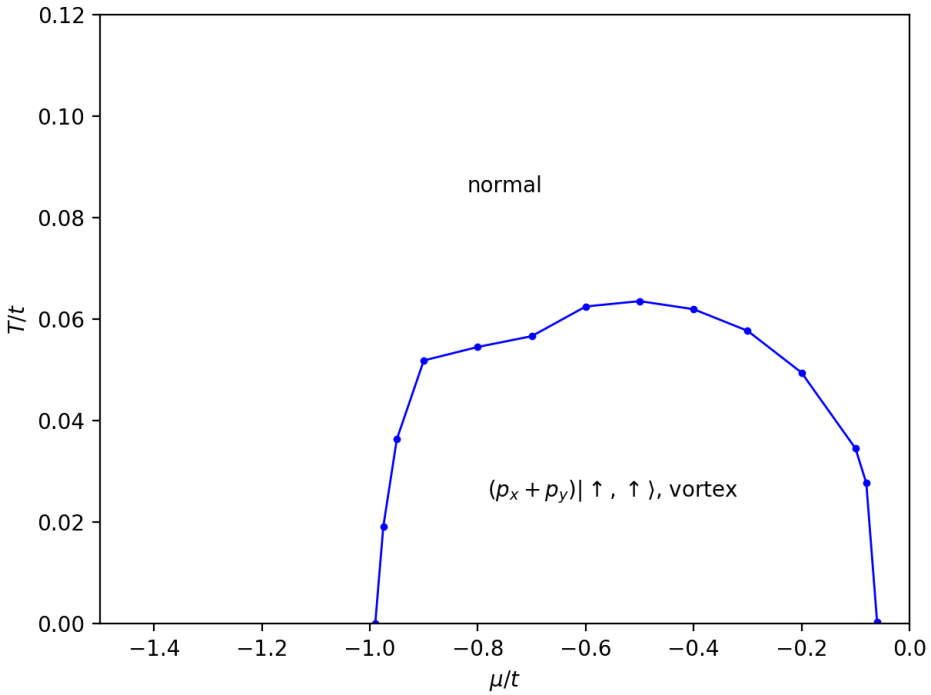

Figure 7.7: μ-T phase diagram for the same input parameters as in figures 7.5 and 7.6. The boundary conditions are open, and the magnetic field is determined using Method 2.

finite-system than bulk system magnetization at the same values of the chemical potential. Thus, a higher filling degree is needed using Method 2 instead of Method 1, for the magnetic field to be equally strong. Indeed, the onset of the vortex region occurs when the magnetization reaches a certain value, and this happens closer to half-filling in figure 7.7. This indicate that the Peierls substitution becomes invalid, which is caused by too large changes in the vector potential.

Using Method 2, the phase diagrams do not have to be restricted to a particular range of input parameters. Based on the discussion so far, the magnetic field due to the magnetization should be weakened. Hopefully, this will give us more reliable results. In figure 7.8, a phase diagram for a much lower exchange field strength is given. Here the spontaneous vortex phase of $p_x + p_y$ with the single and combined spin configurations appear. The low degree of splitting between the up- and down-spin band causes the $|\uparrow,\uparrow\rangle + |\downarrow,\downarrow\rangle$ spin configuration to be the most stable in a large part of the phase diagram. Far from half-filling, in a small region between $\mu/t = -3.0$ and $\mu/t = -2.5$, the gap in the down-spin band becomes negligible, so that $|\uparrow,\uparrow\rangle$ appears. For higher exchange field strengths, we find that the self-consistent solution converges to $|\uparrow,\uparrow\rangle$ below and $|\downarrow,\downarrow\rangle$ above half-filling in a larger region than in figure 7.8. Looking at the development of the superconducting order parameters for $h/t = 0.1$ in the absence of a magnetic field, the superconductivity is greatest around half-filling, and it steadily decreases away from $\mu/t = 0.0$. Therefore, it makes sense that the vortex phase is present as the most stable phase at higher temperatures closer to half-filling. In other words, a greater thermal energy is required here to make the higher FM order in the normal conducting state energetically favourable. In fact, there are apparently no physically unrealistic regions in this phase diagram.

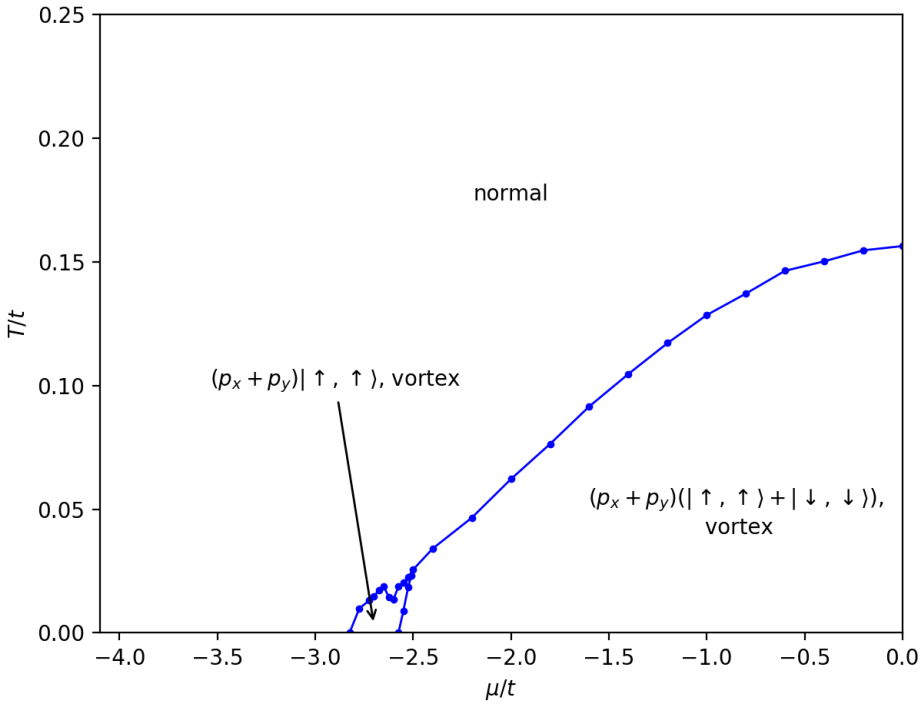

Figure 7.8: Spontaneous vortex phase diagram computed using Method 2. The input parameters are $V/t = -2.5$, $h/t = 0.1$, $L_x = 15$ and $L_y = 15$.

It would also have been interesting if we could find a phase diagram showing the relation between the vortex phase and the purely superconducting phase, that is the state having zero winding number and no vortices. By reducing the value of h even more, we have discovered another type of shortcoming of the numerical procedure outlined in this thesis. When the magnetic field is weak, the self-consistent solution can converge to the vortex or non-vortex state depending on the initial conditions of the paring amplitudes and the gauge used. We here note that in the case of $h/t = 0.1$, it does happen that a particular set of initial conditions give the non-vortex state at some points in the phase diagram of figure 7.8. Nevertheless, other initial conditions result in the vortex state for the same physical parameters. The important observation is that the purely superconducting state generally appear at isolated points, and the free energy of this state is not found to be lower than for the vortex state. Therefore, we do not find any consistent region where the purely superconducting state is the most stable. For even weaker exchange fields, at least one of the different initial conditions give the non-vortex state persistently. The free energy curves are then connected also for the purely superconducting state. By itself, this is by no means a problem. Following the usual free energy minimization procedure, we should be able to determine the state of highest stability. However, the problem is that the free energy curves do not behave in a consistent way. In large regions, there are no significant difference in the free energies of the purely superconducting state and the vortex state. Intuitively, the free energy of the non-vortex state should be lower because of the vanishing superconductivity in the vortex cores. Analyzing how the magnitude of the p-wave superconducting order parameters varies in the purely superconducting state, we find that the superconductivity is considerably smaller in some parts of the system. This explains why we can have that the free energy curves overlap.

As we see it, there can be two reasons for the suppression of the purely superconducting state. First of all, it can be a consequence of finite-size system boundary effects in p-wave superconductors, like the ZES. Due to the slow convergence of the self-consistent algorithm in the presence of a magnetic field, we have been enforced to use a quite small system size. Thus, boundary effects certainly have some influence. It is now worth to point out why the magnetic periodic boundary conditions are here not of interest in order to minimize the boundary effects. The reason is that we are searching for the transition between the vortex state and the purely superconducting state, which is expected to occur in the range from having no magnetic flux up to only a few superconducting flux quanta, possibly only a single flux quantum. When we are using the magnetic translation operators, the flux through the system should be discretized in even numbers of superconducting quanta, meaning that we would have a discontinuous jump from 0 to 2 and 2 to 4 quanta. Secondly, we can also imagine that the procedure where vortices are detected by the phase change of the order parameter gives a false negative. In other words, it can be that we get a vanishing winding number for the system due to the canceling of positive and negative winding numbers of different vortices. In this situation, vortices are present, but the system size is too small to avoid different vortices to interfere. On the other hand, this should be of little concern when the flux is low, but it can explain the isolated points with zero winding number at higher magnetic fields.

7.5 Concluding remarks

In the light of the discussion of the phase diagrams, it seems again to be an issue related to the modeling of the magnetic field through the Peierls substitution. As we have seen, the results becomes unreliable when the magnetic field is too strong. This means that the change in the vector potential between neighbouring sites can be large, which probably invalidates the use of the Peierls formalism. As an additional remark, there is a periodicity in the Peierls phase. If we add a multiple of 2π to the Peierls phase, the Hamiltonian remains the same. Consequently, changing the magnetic field in steps of $2\Phi_0$, the Peierls phase will effectively be the same. For instance, when the Peierls substitution is utilized, a magnetic field strength equal to $2\Phi_0$ gives the same results as what we get in the absence of a magnetic field. Still, because of the magnetization not being higher than Φ_0, this is not the cause of the unexpected behaviour.

A phase diagram that is in agreement with physical predictions, has been computed for $h/t = 0.1$, in which the spontaneous vortex state is present in both the single up-spin and the combined spin configuration of $p_x + p_y$. We have also pointed out the limitations of our solution strategy in the comparison of the purely superconducting and the vortex state of p-wave superconductors. Here we are in the lack of having a consistent way to decide if the vortex or non-vortex state is the most stable, when the free energy curves corresponding to zero and non-zero winding numbers overlap. When it comes to FM order modeled by the Hubbard U-term, it has been even more difficult to find a parameter set giving a reliable phase diagram. For too high values of U, the self-consistent solution becomes unreliable. However, for a lower interaction strength the free energy curves of the purely superconducting and the vortex state start to overlap. Therefore, the results and discussion have been limited to the case of $h \neq 0, U = 0$.

Chapter 8

General conclusions and outlook

In this master's thesis, we have studied the properties of FM equal-spin p-wave superconductors to a great extent, using the 2D extended single-band Hubbard model. In the bulk case without a magnetic field, we have compared the free energies of p_x, $p_x + ip_y$ and $p_x + p_y$ with equal-spin configurations $|\uparrow,\uparrow\rangle$, $|\downarrow,\downarrow\rangle$ and $|\uparrow,\uparrow\rangle + |\downarrow,\downarrow\rangle$. Using the Hubbard U-term, also the normal conducting and superconducting paramagnetic phases have been considered in addition to the ferromagnetic phases. In comparison with the case of a finite-size system, the method for separation of different p-wave orbital symmetries has been better suited for a system with translational invariance. In fact, we have not been able to distinguish between phases like p_x+p_y and $p_x + ip_y$ or $p_x + p_y$ and $p_x - p_y$ for the finite-size system. In the absence of a magnetic field for the bulk system, the phase diagrams show that $p_x + ip_y$ generally is the most stable p-wave symmetry. As opposed to p_x and $p_x + p_y$, this orbital symmetry has a fully gapped DOS due to no nodal lines in the $\boldsymbol{k}$-space gap function. Consequently, the superconducting contribution to the free energy is found to be lower for this symmetry in general. Additionally, none of the phase diagrams are particle-hole symmetric. This was predicted for the exchange field term, but it was a bit surprising in the case of the Hubbard U-term since phase diagrams for purely magnetic phases obey this symmetry. Yet, when superconductivity and magnetism are combined, the particle-hole symmetry is broken as the free energy caused by the U-term is higher for increasing electron densities at a fixed magnetization. The computation of phase diagrams have also made it clear that phase transitions from FM superconducting phases to the FM normal conducting state occur at points where the superconducting p-wave order parameters are finite. This can be explained from the higher FM order in the normal conducting state.

An important part of this master's project has been the testing of whether it is possible to determine a self-consistent vector potential when the supercurrent is accounted for through the Maxwell equation. Using the methods presented in this thesis, including the introduction of a vacuum region and successively reduced nearest-neighbour hopping amplitudes, it has not been possible to obtain a convergent solution. In addition, the Maxwell equation has both been solved in its general form and by the implementation of the Coulomb gauge $\nabla \cdot \boldsymbol{A}$. Some improvements in the behaviour of the vector potential have been observed using alternative system setups. After all, the self-consistent solution is unstable as the vector potential and the supercurrent acquire new configurations in each iteration. The reason why the method fails, is possibly because of the Peierls substitution only being valid for sufficiently small changes of $\boldsymbol{A}$. The breakdown of the Peierls formalism is certainly the case when we solve the Maxwell equation without the Coulomb gauge, as the divergence of $\boldsymbol{A}$ then becomes substantial. In

this part of the thesis, we have also discussed how the self-consistent solution can give distinct metastable states for different gauges when superconductivity is included in the model. Indeed, using different gauges and fixed initial conditions of the paring amplitudes, distinct vortex configurations are possible. The gauge invariance of the theory is found to be respected if we initialize the superconducting order parameters in a proper way. This insight is of special importance in the computation of phase diagrams as we are interested in the most stable state.

Disregarding the effect of the supercurrent by consideration of extreme type II superconductors, we have explored the spontaneous vortex phase arising from the magnetization alone. Here two different solutions strategies have been used. First of all, the magnetization has been fixed to the bulk system value for the normal conducting state. For this, we have required that the magnetization is at least 4 times higher than the maximal p-wave superconducting order parameter. The computed phase diagrams indicate that this method is incompatible with the use of the Peierls formalism. The reason is that the high magnetization leads to a strong magnetic field. This is a problem as the changes in the vector potential are too large for the Peierls substitution to be valid. The second method has been to update the vector potential through the computation of the global finite-system magnetization. In this way, we have avoided too high magnetic fields. A physically reliable phase diagram has been calculated for $h/t = 0.1, V/t = -2.5$, showing the presence of spontaneous vortex phases. Analogous to the bulk case, we have finite p_x and p_y parameters. Moreover, the combined spin configuration $|\uparrow,\uparrow\rangle + |\downarrow,\downarrow\rangle$ becomes progressively more dominating as the exchange field is lowered, since the energy splitting between the up- and down-spin band decreases. In the search for the transition between the purely superconducting and the vortex state, the free energy curves of these states have been found to overlap. According to the system winding numbers, the phases are distinct. We have pointed out two reasons for this. Firstly, it can be caused by the cancellation of positive and negative winding numbers of different vortices, leading to zero phase change despite there being vortices present. Secondly, the insignificant differences in the free energies can be due to boundary effects, resulting in the observed suppression of the purely superconducting state.

Regarding future studies on FM p-wave superconductors, this thesis suggests that the framework of the Peierls phase must be applied with caution. In the limit of a high magnetic field and a rapidly changing vector potential, the Peierls substitution leads to physically unreliable results. In such cases, another way of implementing the magnetic field should be considered. It is also worth to stress that solving the BdG equations self-consistently for a finite-size system, is a very computational demanding task. The size of the Hamiltonian matrix scales by the square of the number of lattice sites, and in the presence of a magnetic field, a much higher number of iterations is required to reach convergence. In the computation of phase diagrams, a vast number of different gauges should in principle also be considered. Especially, performing the self-consistency procedure on larger systems, will certainly be valuable in the study of p-wave superconductors as they can be influenced by boundary effects due to presence of ZES. A higher system size can possibly also reduce the suppression observed for the purely superconducting state, and it is required to avoid the interference of different vortices.

In this thesis, we have been focused on FM superconductors in the form of equal-spin triplets due to the fact that this type of superconductivity has been found to be more compatible with FM order [36, 38, 39]. Since the free energy is lowered by the presence of FM order, new research projects on FM superconductors should also concentrate on this type of spin-triplets. Expanding the model to include the time degree of freedom of the Cooper pair correlation func-

tion, would allow for superconducting order parameters with odd parity under a permutation of time coordinates. It would have been instructive to compare the free energies of s- and d-wave spin-triplet superconductors with the p-wave superconductors treated in this thesis, both in the presence and the absence of a magnetic field.

Appendix A

Additional derivations

In this appendix, additional calculations, which have not been part of the main text, are given. For completeness, the analytical eigenvalues of the bulk system Hamiltonian in chapter 5 are computed. In context of the tight-binding supercurrent given in chapter 6, we also derive the time derivative of the number operator and its average. Finally, the phase of the magnetic translation operators in chapter 7 is considered.

A.1 Analytical eigenvalues of the Fourier space Hamiltonian matrix

The eigenvalues of the matrix $\boldsymbol{H}_{\boldsymbol{k},\sigma}$, which is given in equation (5.6), can be found using the usual procedure of solving $\det(\boldsymbol{H}_{\boldsymbol{k},\sigma} - E_{\boldsymbol{k},\sigma}\mathbb{1}) = 0$. This leads to

$$\begin{aligned} \det\begin{pmatrix} \epsilon_{\boldsymbol{k}} - \sigma h + U\langle n_{\bar{\sigma}}\rangle - E_{\boldsymbol{k},\sigma} & VF_{\boldsymbol{k},\sigma} \\ VF^*_{\boldsymbol{k},\sigma} & -\epsilon_{\boldsymbol{k}} + \sigma h - U\langle n_{\bar{\sigma}}\rangle - E_{\boldsymbol{k},\sigma} \end{pmatrix} = 0 \\ -\big(\epsilon_{\boldsymbol{k}} - \sigma h + U\langle n_{\bar{\sigma}}\rangle - E_{\boldsymbol{k},\sigma}\big)\big(\epsilon_{\boldsymbol{k}} - \sigma h + U\langle n_{\bar{\sigma}}\rangle + E_{\boldsymbol{k},\sigma}\big) - V^2|F_{\boldsymbol{k},\sigma}|^2 = 0 \\ -\big(\epsilon_{\boldsymbol{k}} - \sigma h + U\langle n_{\bar{\sigma}}\rangle\big)^2 + E^2_{\boldsymbol{k},\sigma} - V^2|F_{\boldsymbol{k},\sigma}|^2 = 0. \end{aligned} \tag{A.1}$$

Hence, the analytical eigenvalues of the 2×2 $\boldsymbol{k}$-space matrix are

$$E_{\boldsymbol{k},\sigma} = \pm\sqrt{\big(\epsilon_{\boldsymbol{k}} - \sigma h + U\langle n_{\bar{\sigma}}\rangle\big)^2 + V^2|F_{\boldsymbol{k},\sigma}|^2}. \tag{A.2}$$

A.2 Time derivative of the number operator

Here the main steps in the calculation of the time derivative of the number operator at site i, are outlined. In quantum mechanics, we have that the time derivative is given as

$$\frac{\partial \hat{n}_i}{\partial t} = i[\hat{H}, \hat{n}_i], \tag{A.3}$$

where

$$\begin{aligned} \hat{H} = -t\sum_{\langle i,j\rangle,\sigma} e^{i\phi_{i,j}}\hat{c}^\dagger_{i,\sigma}\hat{c}_{j,\sigma} - \mu\sum_{i,\sigma}\hat{n}_{i,\sigma} + \frac{1}{2}V\sum_{\langle i,j\rangle,\sigma}\hat{n}_{i,\sigma}\hat{n}_{j,\sigma} \\ - h\sum_i(\hat{n}_{i,\uparrow} - \hat{n}_{i,\downarrow}) + U\sum_i \hat{n}_{i,\uparrow}\hat{n}_{i,\downarrow}. \end{aligned} \tag{A.4}$$

This Hamiltonian conserves the particle number and can therefore be used in the calculation of the time derivative of the $\hat{n}_i$. For the μ- and h-term, we have

$$\begin{aligned}
\sum_{l,\sigma,\sigma'} [\hat{n}_{l,\sigma}, \hat{n}_{i,\sigma'}] &= \sum_{l,\sigma,\sigma'} [\hat{c}^\dagger_{l,\sigma}\hat{c}_{l,\sigma}, \hat{c}^\dagger_{i,\sigma'}\hat{c}_{i,\sigma'}] \\
&= \sum_{l,\sigma,\sigma'} \big(\hat{c}^\dagger_{l,\sigma}\hat{c}_{l,\sigma}\hat{c}^\dagger_{i,\sigma'}\hat{c}_{i,\sigma'} - \hat{c}^\dagger_{i,\sigma'}\hat{c}_{i,\sigma'}\hat{c}^\dagger_{l,\sigma}\hat{c}_{l,\sigma}\big) \\
&= \sum_{l,\sigma,\sigma'} \big[\hat{c}^\dagger_{l,\sigma}(\delta_{l,i}\delta_{\sigma,\sigma'} - \hat{c}^\dagger_{i,\sigma'}\hat{c}_{l,\sigma})\hat{c}_{i,\sigma'} - \hat{c}^\dagger_{i,\sigma'}(\delta_{l,i}\delta_{\sigma,\sigma'} - \hat{c}^\dagger_{l,\sigma}\hat{c}_{i,\sigma'})\hat{c}_{l,\sigma}\big] \\
&= \sum_{l,\sigma,\sigma'} \big(\hat{c}^\dagger_{i,\sigma'}\hat{c}^\dagger_{l,\sigma}\hat{c}_{i,\sigma'}\hat{c}_{l,\sigma} - \hat{c}^\dagger_{l,\sigma}\hat{c}^\dagger_{i,\sigma'}\hat{c}_{l,\sigma}\hat{c}_{i,\sigma'}\big) \\
&= 0.
\end{aligned} \tag{A.5}$$

In the last line, the fact that the fermionic creation operators anticommute, and the same for the annihilation operators, is used. Similarly, it can be shown that the commutator with the U- and V-term vanishes. In fact, there is only a contribution from the hopping term given as

$$\begin{aligned}
[\hat{H}_t, \hat{n}_i] &= -t \sum_{k,l,\sigma,\sigma'} e^{i\phi_{k,l}} [\hat{c}^\dagger_{k,\sigma}\hat{c}_{l,\sigma}, \hat{c}^\dagger_{i,\sigma'}\hat{c}_{i,\sigma'}] \\
&= -t \sum_{k,l,\sigma,\sigma'} e^{i\phi_{k,l}} \big(\hat{c}^\dagger_{k,\sigma}\hat{c}_{l,\sigma}\hat{c}^\dagger_{i,\sigma'}\hat{c}_{i,\sigma'} - \hat{c}^\dagger_{i,\sigma'}\hat{c}_{i,\sigma'}\hat{c}^\dagger_{k,\sigma}\hat{c}_{l,\sigma}\big) \\
&= -t \sum_{k,l,\sigma,\sigma'} e^{i\phi_{k,l}} \big[\hat{c}^\dagger_{k,\sigma}(\delta_{l,i}\delta_{\sigma,\sigma'} - \hat{c}^\dagger_{i,\sigma'}\hat{c}_{l,\sigma})\hat{c}_{i,\sigma'} - \hat{c}^\dagger_{i,\sigma'}(\delta_{k,i}\delta_{\sigma,\sigma'} - \hat{c}^\dagger_{k,\sigma}\hat{c}_{i,\sigma'})\hat{c}_{l,\sigma}\big].
\end{aligned} \tag{A.6}$$

Analogous to the commutator in equation (A.5), the second and fourth term above cancel each other, so that

$$\begin{aligned}
[\hat{H}_t, \hat{n}_i] &= -t \sum_{k,l,\sigma,\sigma'} e^{i\phi_{k,l}} \big(\hat{c}^\dagger_{k,\sigma}\delta_{l,i}\delta_{\sigma,\sigma'}\hat{c}_{i,\sigma'} - \hat{c}^\dagger_{i,\sigma'}\delta_{k,i}\delta_{\sigma,\sigma'}\hat{c}_{l,\sigma}\big) \\
&= -t \sum_{\sigma} \big[\sum_{k} e^{i\phi_{k,i}}\hat{c}^\dagger_{k,\sigma}\hat{c}_{i,\sigma} - \sum_{l} e^{i\phi_{i,l}}\hat{c}^\dagger_{i,\sigma}\hat{c}_{l,\sigma}\big].
\end{aligned} \tag{A.7}$$

Renaming the indices k and l as $k, l = j$, the time derivative is

$$\frac{\partial \hat{n}_i}{\partial t} = it \sum_{j,\sigma} \big(e^{i\phi_{i,j}}\hat{c}^\dagger_{i,\sigma}\hat{c}_{j,\sigma} - \text{h.c.}\big). \tag{A.8}$$

A.3 Average of the time derivative of the number operator

To derive the average of equation (A.8), the Bogoliubov transformations in equations (6.14) and (6.15) are inserted, leading to

$$\frac{\partial \hat{n}_i}{\partial t} = it \sum_{j} \sum_{n,n'} \big(e^{i\phi_{i,j}} u^*_{n,i,\sigma} u_{n',j,\sigma} \alpha^\dagger_{n,\sigma}\alpha_{n',\sigma} - \text{h.c.}\big). \tag{A.9}$$

Taking the average and using that $\langle \alpha^\dagger_{n,\sigma} \alpha_{n',\sigma} \rangle = f(E_{n,\sigma}) \delta_{n,n'}$, result in

$$\begin{aligned} \left\langle \frac{\partial n_i}{\partial t} \right\rangle &= it \sum_j \sum_{n,n'} \left(e^{i\phi_{i,j}} u^*_{n,i,\sigma} u_{n',j,\sigma} \langle \alpha^\dagger_{n,\sigma} \alpha_{n',\sigma} \rangle - \text{h.c.} \right) \\ &= it \sum_{j,n} \left(e^{i\phi_{i,j}} u^*_{n,i,\sigma} u_{n,j,\sigma} - \text{h.c.} \right) f(E_{n,\sigma}). \end{aligned} \tag{A.10}$$

A.4 Determination of the phases of the magnetic translation operators

In this section, the phases ($\theta^x_{m_x,m_y}$, $\theta^y_{m_x,m_y}$) of the magnetic translation operators ($\hat{M}_x$, $\hat{M}_y$) will be motivated using the same methods as Aidelsburger and Bernevig [72, 83]. In total, we require that $[\hat{M}_{x(y)}, \hat{H}] = 0$. In other words, the four commutators $[\hat{M}_{x(y)}, \hat{T}_{x(y)}]$ are set to zero. First of all, we have that $[\hat{M}_x, \hat{T}_x]$ is zero if

$$e^{i(\theta^x_{m_x+1,m_y} + \phi^x_{m_x,m_y})} \left[1 - e^{i(\theta^x_{m_x,m_y} - \theta^x_{m_x+1,m_y} + \phi^x_{m_x+1,m_y} - \phi^x_{m_x,m_y})} \right] = 0, \tag{A.11}$$

that is

$$\theta^x_{m_x+1,m_y} - \theta^x_{m_x,m_y} = \phi^x_{m_x+1,m_y} - \phi^x_{m_x,m_y}. \tag{A.12}$$

Moreover, the commutator of $\hat{M}_x$ and $\hat{T}_y$ vanishes if

$$e^{i(\theta^y_{m_x,m_y+1} + \phi^x_{m_x,m_y})} \left[1 - e^{i(\theta^x_{m_x,m_y} - \theta^x_{m_x,m_y+1} + \phi^y_{m_x+1,m_y} - \phi^y_{m_x,m_y})} \right] = 0, \tag{A.13}$$

so that

$$\begin{aligned} \theta^x_{m_x,m_y+1} - \theta^x_{m_x,m_y} &= \phi^y_{m_x+1,m_y} - \phi^y_{m_x,m_y} \\ &= \phi^x_{m_x,m_y+1} - \phi^x_{m_x,m_y} - \pi \Phi_{m_x,m_y}, \end{aligned} \tag{A.14}$$

where equation (6.22) is used. Similarly, we get

$$\begin{aligned} \theta^y_{m_x+1,m_y} - \theta^y_{m_x,m_y} &= \phi^x_{m_x,m_y+1} - \phi^x_{m_x,m_y} \\ &= \phi^y_{m_x+1,m_y} - \phi^y_{m_x,m_y} + \pi \Phi_{m_x,m_y}, \end{aligned} \tag{A.15}$$

from $[\hat{M}_y, \hat{T}_y] = 0$, and

$$\theta^y_{m_x,m_y+1} - \theta^y_{m_x,m_y} = \phi^y_{m_x,m_y+1} - \phi^y_{m_x,m_y}, \tag{A.16}$$

from $[\hat{M}_y, \hat{T}_x] = 0$. These equations can be solved with respect to $\theta^x_{m_x,m_y}$ and $\theta^y_{m_x,m_y}$, yielding

$$\theta^x_{m_x,m_y} = \phi^x_{m_x,m_y} - \pi \Phi_{m_x,m_y} m_y \tag{A.17}$$

$$\theta^y_{m_x,m_y} = \phi^y_{m_x,m_y} + \pi \Phi_{m_x,m_y} m_x. \tag{A.18}$$

Appendix B

Zero-energy states (ZES)

To illustrate the concept of zero-energy states (ZES), we will consider relevant results obtained by Terrade [52], which were reproduced and discussed in the specialization project. In fact,

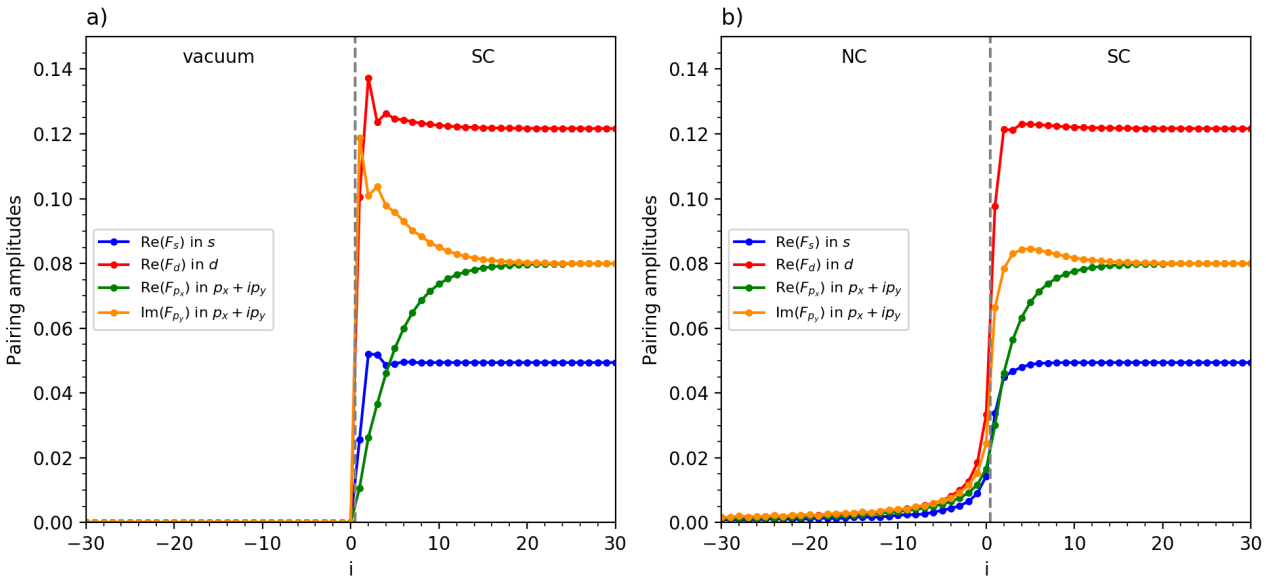

Figure B.1: Opposite-spin superconducting paring amplitudes of extended (unconventional) s-wave (F_s), $d_{x^2-y^2}$ (F_d), and the p_x- (F_{p_x}) and p_y-component (F_{p_y}) of $p_x + ip_y$. In addition to a superconducting region (SC) , the heterostructure consists of vacuum in plot a) and a normal conductor (NC) in plot b). The interface is located between sites $i = 0$ and $i = 1$ in the x-direction. The hopping amplitude t is zero in the vacuum, and it is 1 otherwise. The temperature is equal to $T = 0.0$ and the superconducting interaction strength is $V = -2.5$. The chemical potentials are $\mu = -3.5$ for s, $\mu = -0.5$ for d and $\mu = -1.5$ for $p_x + ip_y$.

plot a) in figure B.1, which is for a vacuum-superconductor heterostructure, shows the same dependence of the p_x and p_y superconducting order parameters as observed in section 7.2. In the proximity of the boundary to vacuum, F_{p_x} is suppressed, while F_{p_y} is enlarged. Since p_x has a $\sin k_x$ momentum dependence, the π-shift due to ZES at the boundary, leads to suppression. As discussed by Terrade, the enlargement of the p_y paring amplitude can arise because of bounded

states and a higher density of Cooper pairs close to the boundary [52]. With an interface normal to the y-direction instead of the x-direction, the opposite happens.

As a reference, the behaviour of order parameters of the extended s-wave and $d_{x^2-y^2}$ are included. These paring amplitudes acquire the bulk magnitude of a shorter range than F_{p_x} and F_{p_y}. Considering figure B.2, ZES are clearly present for $p_x + ip_y$ and absent for extended s-wave. We also not that ZES can also be introduced into the DOS of a $d_{x^2-y^2}$-superconductor when the interface is oriented in the [110]-direction [87]. However, this is not fulfilled here, so that we do not observe the same suppression of the d-wave paring amplitude. It is also worth to point out that another proximity effect known as Andreev reflections [88], occur in the vacuum is replaced by a metal. In plot b) of figure B.1, there are leakages of Cooper pairs into the non-superconducting region.

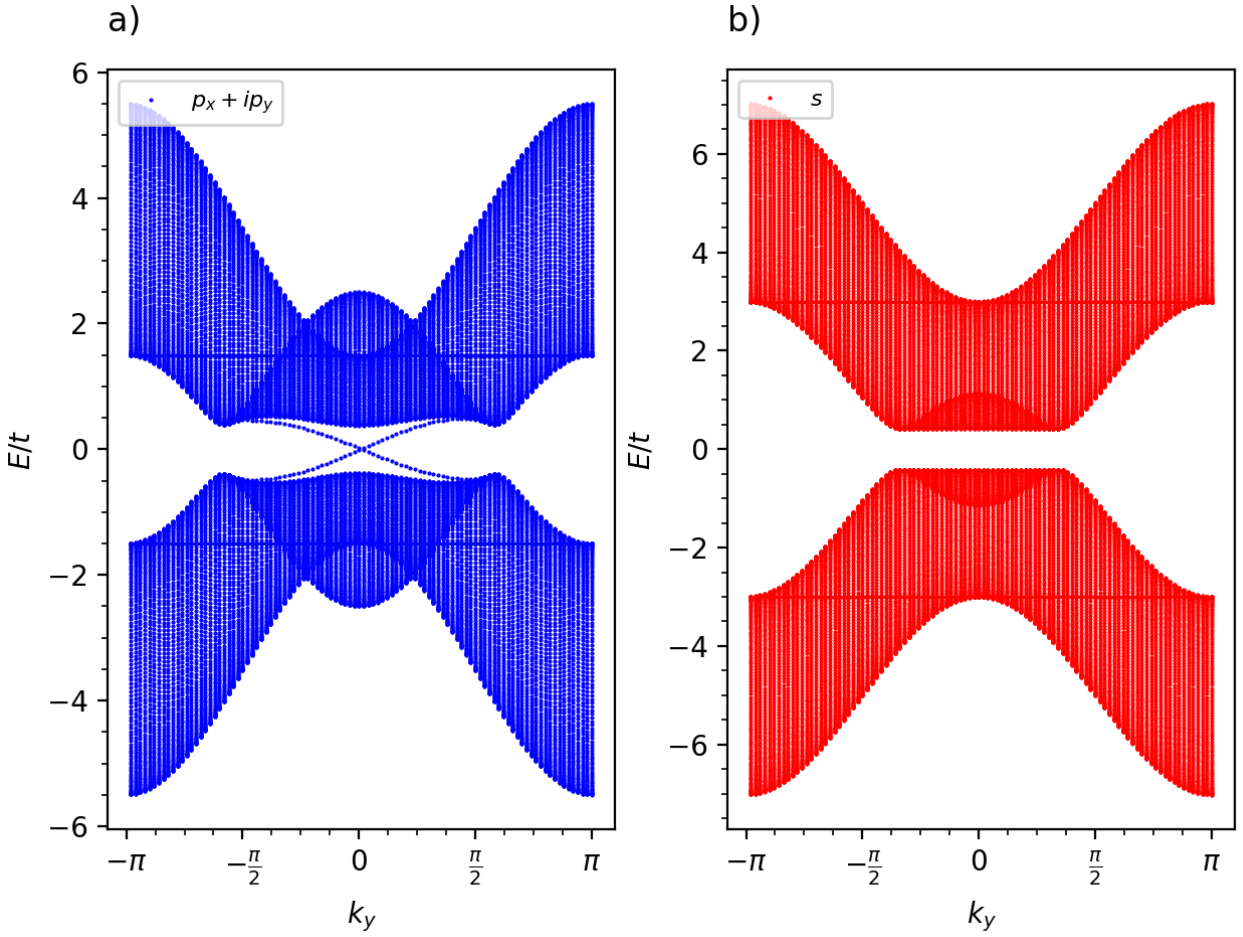

Figure B.2: Local energy spectra in the grand canonical ensemble of $p_x + ip_y$ (a) and s (b) for a vacuum-SC heterostructure. The plots are obtained for the first line of sites inside ($i = 1$) the superconducting region, and the physical parameters are as in figure B.1. The y-component of the momentum (on the x-axis) is a good quantum number as the heterostructure has translational symmetry in this direction.

Bibliography

[1] É. du Trémolet de Lacheisserie. "Magnetism, from the Dawn of Civilization to Today". In: *Magnetism*. Springer, 2002, pp. 3–18. ISBN: 978-0-387-23062-7.

[2] O. Darrigol. *Electrodynamics from Ampère to Einstein*. Oxford University Press, 2000. Chap. 1, pp. 3–36. ISBN: 9780198505938.

[3] B. N. Dwivedi. "James Clerk Maxwell and his equations". In: *Resonance* 8.5 (2003), pp. 4–16. DOI: 10.1007/BF02867125.

[4] F. Weinert. "Stern—Gerlach Experiment". In: *Compendium of Quantum Physics*. Ed. by D. Greenberger, K. Hentschel, and F. Weinert. Springer, 2009, pp. 746–750. ISBN: 978-3-540-70626-7.

[5] M. Massimi. "Exclusion Principle (or Pauli Exclusion Principle)". In: *Compendium of Quantum Physics*. Ed. by D. Greenberger, K Hentschel, and F. Weinert. Springer, 2009, pp. 220–222. ISBN: 978-3-540-70626-7.

[6] C. Timm. *Theory of Magnetism*. Chap. 4, 10, pp. 23, 89–91. 2015. URL: https://www.physik.tu-dresden.de/~timm/personal/teaching/thmag_w09/lecturenotes.pdf (visited on June 7, 2020).

[7] D. van Delft and P. Kes. "The discovery of superconductivity". In: *Physics Today* 63.9 (2010), pp. 38–43. DOI: 10.1063/1.3490499.

[8] A. M. Forrest. "Meissner and Ochsenfeld revisited". In: *European Journal of Physics* 4.2 (1983), pp. 117–120. DOI: 10.1088/0143-0807/4/2/011.

[9] J. Bardeen, L. N. Cooper, and J. R. Schrieffer. "Theory of Superconductivity". In: *Physical Review Journal* 108.5 (1957), pp. 1175–1204. DOI: 10.1103/PhysRev.108.1175.

[10] G. Webb, F. Marsiglio, and J. Hirsch. "Superconductivity in the elements, alloys and simple compounds". In: *Physica C: Superconductivity and its Applications* 514 (2015), pp. 17–27. DOI: 10.1016/j.physc.2015.02.037.

[11] H. Fröhlich. "Theory of the Superconducting State. I. The Ground State at the Absolute Zero of Temperature". In: *Physical Review Journal* 79.5 (1950), pp. 845–856. DOI: 10.1103/PhysRev.79.845.

[12] Y. Yang. "Rigorous proof of isotope effect by Bardeen–Cooper–Schrieffer theory". In: *Journal of Mathematical Physics* 44.5 (2003), pp. 2009–2025. DOI: 10.1063/1.1565831.

[13] M. Olsen. "Superconductivity of Lead Isotopes". In: *Nature* 168.4267 (1951), pp. 245–246. DOI: 10.1038/168245a0.

[14] E. Maxwell. "Superconductivity of the Isotopes of Tin". In: *Physical Review Journal* 86.2 (1952), pp. 235–242. DOI: 10.1103/PhysRev.86.235.

[15] J. G. Bednorz and K. A. Müller. "Possible High T_c Superconductivity in the Ba-La-Cu-O System". In: *Zeitschrift für Physik B Condensed Matter* 64.2 (1986), pp. 189–193. DOI: 10.1007/BF01303701.

[16] J. G. Bednorz and K. A. Müller. *Perovskite-Type Oxides - The New Approach to High-T_c Superconductivity*. Nobel lecture, pp. 424–455. 1987. URL: https://www.nobelprize.org/uploads/2018/06/bednorz-muller-lecture.pdf (visited on June 7, 2020).

[17] M. K. Wu et al. "Superconductivity at 93 K in a New Mixed-Phase Y-Ba-Cu-O Compound System at Ambient Pressure". In: *Physical Review Letters* 58.9 (1987), pp. 908–910. DOI: 10.1103/PhysRevLett.58.908.

[18] A. P. Drozdov et al. "Superconductivity at 250 K in lanthanum hydride under high pressures". In: *Nature* 569.7757 (2019), pp. 528–531. DOI: 10.1038/s41586-019-1201-8.

[19] G. R. Stewart. "Unconventional superconductivity". In: *Advances in Physics* 66.2 (2017), pp. 79–80. DOI: 10.1080/00018732.2017.1331615.

[20] S. S. Saxena et al. "Superconductivity on the border of itinerant-electron ferromagnetism in UGe_2". In: *Nature* 406.6796 (2000), pp. 587–592. DOI: 10.1038/35020500.

[21] D. Aoki et al. "Coexistence of superconductivity and ferromagnetism in URhGe". In: *Nature* 413.6856 (2001), pp. 613–616. DOI: 10.1038/35098048.

[22] N. T. Huy et al. "Superconductivity on the Border of Weak Itinerant Ferromagnetism in UCoGe". In: *Physical Review Letters* 99.6 (2007), p. 067006. DOI: 10.1103/PhysRevLett.99.067006.

[23] T. R. Kirkpatrick et al. "Superconductivity and Quantum Phase Transitions in Weak Itinerant Ferromagnets". In: *Recent Progress In Many-body Theories - Proceedings Of The 11th International Conference*. Ed. by R. F. Bishop et al. World Scientific Publishing Company, 2002, pp. 132–141. ISBN: 9789814489195.

[24] D. Aoki et al. "Spin-Triplet Superconductivity in UTe_2 and Ferromagnetic Superconductors". In: *Journal of the Physical Society of Japan* 30 (2020), p. 011065. DOI: 10.7566/JPSCP.30.011065.

[25] F. Hardy and A. D. Huxley. "p-Wave Superconductivity in the Ferromagnetic Superconductor URhGe". In: *Physical Review Letters* 94.24 (2005), p. 247006. DOI: 10.1103/PhysRevLett.94.247006.

[26] D. Fay and J. Appel. "Coexistence of p-state superconductivity and itinerant ferromagnetism". In: *Phys. Rev. B* 22.7 (1980), pp. 3173–3182. DOI: 10.1103/PhysRevB.22.3173.

[27] S. Ran et al. "Nearly ferromagnetic spin-triplet superconductivity". In: *Science* 365.6454 (2019), pp. 684–687. DOI: 10.1126/science.aav8645.

[28] A. de Visser. "UTe_2: A New Spin-Triplet Pairing Superconductor". In: *JPSJ News and Comments* 16 (2019), p. 08. DOI: 10.7566/JPSJNC.16.08.

[29] J. Linder and J. W. A. Robinson. "Superconducting spintronics". In: *Nature Physics* 11.4 (2015), pp. 307–315. DOI: 10.1038/nphys3242.

[30] J. Hubbard. "Electron correlations in narrow energy bands". In: *Proceedings of the Royal Society of London Series A* 276.1365 (1963), pp. 238–257. DOI: 10.1098/rspa.1963.0204.

[31] P. R. Bertussi et al. "Kondo–attractive-Hubbard model for the ordering of local magnetic moments in superconductors". In: *Physical Review B* 79.2 (2009), p. 220513. DOI: 10.1103/PhysRevB.79.220513.

[32] "The Hubbard model at half a century". In: *Nature Physics* 9.9 (2013), p. 523. DOI: 10.1038/nphys2759.

[33] R. Peierls. "Zur Theorie des Diamagnetismus von Leitungselektronen". In: *Zeitschrift für Physik* 80.11 (1933), pp. 763–791. DOI: 10.1007/BF01342591.

[34] D. R. Hofstadter. "Energy levels and wave functions of Bloch electrons in rational and irrational magnetic fields". In: *Physical Review B* 14.6 (1976), pp. 2239–2249. DOI: 10.1103/PhysRevB.14.2239.

[35] C. W. Gardiner and P. Zoller. *Quantum World Of Ultra-cold Atoms And Light, The - Book Iii: Ultra-cold Atoms*. World Scientific Publishing Company, 2017. Chap. 27, pp. 506–511. ISBN: 9781786344199.

[36] M. Eschrig et al. "Symmetries of Pairing Correlations in Superconductor-Ferromagnet Nanostructures". In: *Journal of Low Temperature Physics* 147.3 (2007), pp. 457–476. DOI: 10.1007/s10909-007-9329-6.

[37] F. S. Bergeret, A. F. Volkov, and K. B. Efetov. "Long-Range Proximity Effects in Superconductor-Ferromagnet Structures". In: *Phys. Rev. Lett.* 86.18 (2001), pp. 4096–4099. DOI: 10.1103/PhysRevLett.86.4096.

[38] T. S. Khaire et al. "Observation of Spin-Triplet Superconductivity in Co-Based Josephson Junctions". In: *Physical Review Letters* 104.13 (2010), p. 137002. DOI: 10.1103/PhysRevLett.104.137002.

[39] R. S. Keizer et al. "A spin triplet supercurrent through the half-metallic ferromagnet CrO_2". In: *Nature* 439.7078 (2006), pp. 825–827. DOI: 10.1038/nature04499.

[40] M. Tachiki et al. "Self-induced vortices in magnetic superconductors". In: *Solid State Communications* 34.1 (1980), pp. 19–23. DOI: 10.1016/0038-1098(80)90620-1.

[41] C. G. Kuper, M. Revzen, and A. Ron. "Ferromagnetic Superconductors: A Vortex Phase in Ternary Rare-Earth Compounds". In: *Physical Review Letters* 44.23 (1980), pp. 1545–1548. DOI: 10.1103/PhysRevLett.44.1545.

[42] W.-H. Jiao et al. "Evidence of spontaneous vortex ground state in an iron-based ferromagnetic superconductor". In: *npj Quantum Materials* 2.1 (2017), p. 50. DOI: 10.1038/s41535-017-0057-0.

[43] A. L. Fetter and J. D. Walecka. *Quantum Theory of Many-Particle Systems*. Dover Publications, 2013. Chap. 1, pp. 7–19. ISBN: 978-0-486-42827-7.

[44] J. O. Fjærestad. *"Second quantization" (the occupation-number representation)*. pp. 1–16. 2013. URL: https://folk.ntnu.no/johnof/second-quantization-2013 (visited on June 8, 2020).

[45] J. C. Cuevas and E. Scheer. *Molecular Electronics: An Introduction to Theory and Experiment*. World Scientific Publishing Company, 2010. Chap. 9, pp. 136–140. ISBN: 9789814282598.

[46] W. M. C. Foulkes. "Tight-Binding Models and Coulomb Interactions for s, p, and d Electrons". In: *Quantum Materials: Experiments and Theory*. Ed. by E. Pavarini et al. Forschungszentrum Jülich GmbH Institute for Advanced Simulation, 2016, pp. 3.29–3.35. ISBN: 978-3-95806-159-0.

[47] J. O. Fjærestad. *Introduction to Green functions and many-body perturbation theory*. pp. 1–22. 2013. URL: http://folk.ntnu.no/johnof/green-2013.pdf (visited on June 9, 2020).

[48] J. O. Fjærestad. *Tight-binding model for electrons in a crystal*. pp. 1–4. 2014. URL: https://folk.ntnu.no/johnof/tight-binding-2014.pdf (visited on June 9, 2020).

[49] R. E. Hummel. *Electrons in a Crystal*. Springer, 2011. Chap. 6, pp. 63–65. ISBN: 978-1-4419-8164-6.

[50] H. Jin and T. Miyazaki. *The Physics of Ferromagnetism*. Springer, 2012. Chap. 3, pp. 117–120. ISBN: 978-3-642-25583-0.

[51] W. Nolting and A. Ramakanth. *Quantum Theory of Magnetism*. Springer, 2009. Chap. 5, pp. 180–188. ISBN: 978-3-540-85416-6.

[52] D. Terrade. "Proximity Effects and Josephson Currents in Ferromagnet - Spin-Triplet Superconductors Junctions". PhD thesis. University of Stuttgart, 2015. URL: https://pdfs.semanticscholar.org/485e/d43c1bdc98994a9d2f88e04d308f5af2eabe.pdf (visited on June 9, 2020).

[53] M. Cuoco et al. "Proximity effect between an unconventional superconductor and a ferromagnet with spin bandwidth asymmetry". In: *Physical Review B* 78.5 (2008), p. 054503. DOI: 10.1103/PhysRevB.78.054503.

[54] K. B. Efetov et al. "Proximity Effects in Ferromagnet/Superconductor Heterostructures". In: *Magnetic Heterostructures: Advances and Perspectives in Spinstructures and Spintransport*. Ed. by H. Zabel and S. D. Bader. Springer, 2008, pp. 251–255. ISBN: 978-3-540-73462-8.

[55] F. Lechermann. "Model Hamiltonians and Basic Techniques". In: *The LDA+DMFT approach to strongly correlated materials*. Ed. by E. Pavarini et al. Forschungszentrum Jülich GmbH Institute for Advanced Simulations, 2011, pp. 3.15–3.17. ISBN: 978-3-89336-734-4.

[56] J. E. Hirsch. "Two-dimensional Hubbard model: Numerical simulation study". In: *Physical Review B* 31.7 (1985), pp. 4403–4419. DOI: 10.1103/PhysRevB.31.4403.

[57] Y. Claveau, B. Arnaud, and S. Matteo. "Mean-field solution of the Hubbard model: The magnetic phase diagram". In: *European Journal of Physics* 35.3 (2014), p. 035023. DOI: 10.1088/0143-0807/35/3/035023.

[58] H. P. Eckle. *Models of Quantum Matter: A First Course on Integrability and the Bethe Ansatz*. Oxford University Press, 2019. Chap. 8, pp. 363–364. ISBN: 9780199678839.

[59] R. T. Scalletar. "Tight-Binding Models and Coulomb Interactions for s, p, and d Electrons". In: *Quantum Materials: Experiments and Theory*. Ed. by E. Pavarini et al. Forschungszentrum Jülich GmbH Institute for Advanced Simulation, 2016, pp. 4.4–4.7. ISBN: 978-3-95806-159-0.

[60] K. Fossheim and A. Sudbø. *Superconductivity Physics and Applications*. John Wiley & Sons, 2004. Chap. 1,3,4. ISBN: 0-470-84452-3.

[61] L. N. Cooper. "Bound Electron Pairs in a Degenerate Fermi Gas". In: *Physical Review Journal* 104.4 (1956), pp. 1189–1190. DOI: 10.1103/PhysRev.104.1189.

[62] Q. Gu et al. "Directly visualizing the sign change of d-wave superconducting gap in $Bi_2Sr_2CaCu_2O_{8+\delta}$ by phase-referenced quasiparticle interference". In: *Nature Communications* 10.1 (2019), p. 1603. DOI: 10.1038/s41467-019-09340-5.

[63] Y. Maeno et al. "Evaluation of Spin-Triplet Superconductivity in Sr_2RuO_4". In: *Journal of the Physical Society of Japan* 81.1 (2012), p. 011009. DOI: 10.1143/jpsj.81.011009.

[64] K. D. Nelson et al. "Odd-Parity Superconductivity in Sr_2RuO_4". In: *Science* 306.5699 (2004), pp. 1151–1154. DOI: 10.1126/science.1103881.

[65] S. Nayak and S. Kumar. "Exotic superconducting states in the extended attractive Hubbard model". In: *Journal of Physics: Condensed Matter* 30.13 (2018), p. 135601. DOI: 10.1088/1361-648x/aaaefe.

[66] M. R. Norman. "The Challenge of Unconventional Superconductivity". In: *Science* 332.6026 (2011), pp. 196–200. DOI: 10.1126/science.1200181.

[67] Jacob Linder and Alexander V Balatsky. "Odd-frequency superconductivity". In: *Reviews of Modern Physics* 91 (2019), p. 045005. DOI: 10.1103/RevModPhys.91.045005.

[68] Christopher Triola and Alexander V. Balatsky. "Odd-frequency superconductivity in driven systems". In: *Physical Review B* 94.9 (2016), p. 094518. DOI: 10.1103/PhysRevB.94.094518.

[69] K. Kuboki. "Effect of Band Structure on the Symmetry of Superconducting States". In: *Journal of the Physical Society of Japan* 70.9 (2001), pp. 2698–2702. DOI: 10.1143/JPSJ.70.2698.

[70] J. Zhu. *Bogoliubov-de Gennes Method and Its Applications*. Springer, 2016. Chap. 2, pp. 111–114. ISBN: 978-3-319-31314-6.

[71] J. M. Luttinger. "The Effect of a Magnetic Field on Electrons in a Periodic Potential". In: *Physical Review Journal* 84.4 (1951), pp. 814–817. DOI: 10.1103/PhysRev.84.814.

[72] M. Aidelsburger. *Artificial Gauge Fields with Ultracold Atoms in Optical Lattices*. Springer, 2016. Chap. 2, pp. 9–17. ISBN: 978-3-319-25829-4.

[73] C. Kittel. *Introduction to Solid State Physics*. John Wiley & Sons, 2005. Chap. 10. ISBN: 0-471-41526-X.

[74] R. G. Sharma. *Superconductivity Basics and Applications to Magnets*. Springer, 2015. Chap. 5, pp. 110–115. ISBN: 978-3-319-13713-1.

[75] A. A. Abrikosov. "On the Magnetic Properties of Superconductors of the Second Group". In: *Soviet Physics JETP* 5.6 (1957), p. 1174. URL: http://www.jetp.ac.ru/cgi-bin/dn/e_005_06_1174.pdf (visited on June 9, 2020).

[76] A. Mourachkine. "Determination of the Coherence Length and the Cooper-Pair Size in Unconventional Superconductors by Tunneling Spectroscopy". In: *Journal of Superconductivity* 17.6 (2004), pp. 711–724. DOI: 10.1007/s10948-004-0831-7.

[77] T. Petrila and D. Trif. *Basics of Fluid Mechanics and Introduction to Computational Fluid Dynamics*. Springer, 2005. Chap. 5, pp. 247–256. ISBN: 978-0-387-23838-8.

[78] V. Risinggård and J. Linder. "Direct and inverse superspin Hall effect in two-dimensional systems: Electrical detection of spin supercurrents". In: *Physical Review B* 99.17 (2019), p. 174505. DOI: 10.1103/PhysRevB.99.174505.

[79] J.J. Sakurai and J. Napolitano. *Modern Quantum Mechanics*. Pearson, 2010. Chap. 2, pp. 134–140. ISBN: 978-0-8053-8291-4.

[80] B. M. Uranga. "Vortices in unconventional correlated superconductors". MA thesis. University of Copenhagen, 2014. URL: https://www.nbi.ku.dk/english/theses/masters-theses/benat-mencia-uranga/thesis_benat.pdf (visited on June 9, 2020).

[81] M. Schmid et al. "d-Wave superconductivity as a catalyst for antiferromagnetism in underdoped cuprates". In: *New Journal of Physics* 12.5 (2010), p. 053043. DOI: 10.1088/1367-2630/12/5/053043.

[82] A. J. Taylor. *Analysis of Quantised Vortex Tangle*. Springer, 2017. Chap. 2, pp. 45–49. ISBN: 978-3-319-48556-0.

[83] B. A. Bernevig. *Topological Insulators and Topological Superconductors*. Princeton University Press, 2013. Chap. 5, pp. 41–44. ISBN: 978-0-691-15175-5.

[84] J. G. Analytis, S. J. Blundell, and A. Ardavan. "Landau levels, molecular orbitals, and the Hofstadter butterfly in finite systems". In: *American Journal of Physics* 72.5 (2004), pp. 613–618. DOI: 10.1119/1.1615568.

[85] R. Wesche. *Physical Properties of High-Temperature Superconductors*. John Wiley & Sons, 2015. Chap. 4, p. 73. ISBN: 9781119978817.

[86] B. Rosenstein and D. Li. "Ginzburg-Landau theory of type II superconductors in magnetic field". In: *Review of Modern Physics* 82.1 (2010), pp. 109–168. DOI: 10.1103/RevModPhys.82.109.

[87] O. Negri et al. "Zero energy states at a normal-metal/cuprate-superconductor interface probed by shot noise". In: *Physical Review B* 97.21 (2018), p. 214504. DOI: 10.1103/PhysRevB.97.214504.

[88] M. J. M. de Jong and C. W. J. Beenakker. "Andreev Reflection in Ferromagnet-Superconductor Junctions". In: *Physical Review Letters* 74.9 (1995), pp. 1657–1660. DOI: 10.1103/PhysRevLett.74.1657.

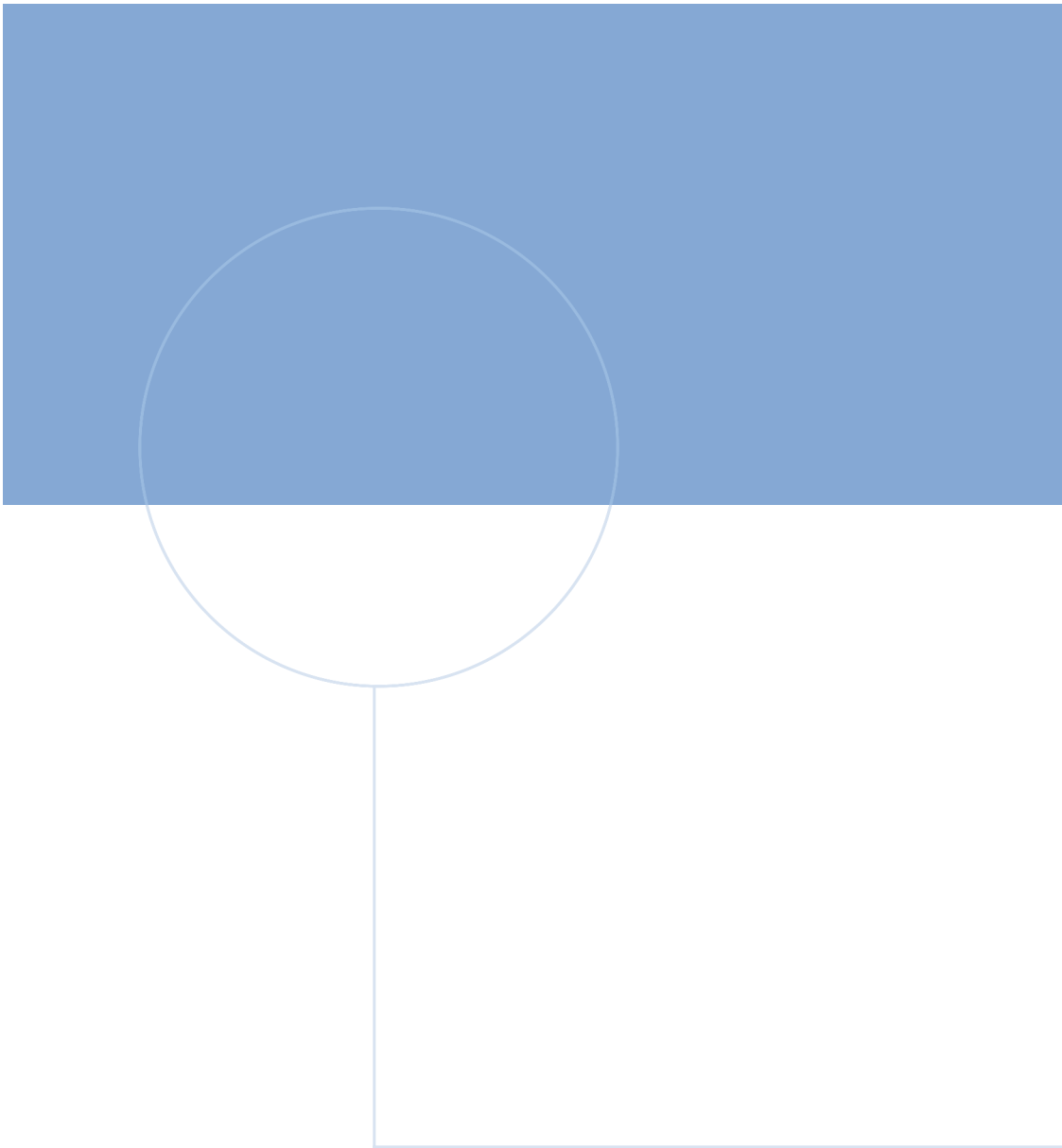

NTNU

Norwegian University of
Science and Technology